



SCHOOL of
GRADUATE STUDIES
EAST TENNESSEE STATE UNIVERSITY

East Tennessee State University
Digital Commons @ East Tennessee
State University

Electronic Theses and Dissertations


Student Works

5-2020

Stacking the Odds for Better GPR: An Antenna Comparison

Montana Kruske
East Tennessee State University

Follow this and additional works at: <https://dc.etsu.edu/etd>

 Part of the [Geophysics and Seismology Commons](#)

Recommended Citation

Kruske, Montana, "Stacking the Odds for Better GPR: An Antenna Comparison" (2020). *Electronic Theses and Dissertations*. Paper 3770. <https://dc.etsu.edu/etd/3770>

This Thesis - unrestricted is brought to you for free and open access by the Student Works at Digital Commons @ East Tennessee State University. It has been accepted for inclusion in Electronic Theses and Dissertations by an authorized administrator of Digital Commons @ East Tennessee State University. For more information, please contact digilib@etsu.edu.

Stacking the Odds for Better GPR: An Antenna Comparison

A thesis

presented to

the faculty of the Department of Geosciences

East Tennessee State University

In partial fulfillment

of the requirements for the degree

Master of Science in Geosciences, Geospatial Analysis

by

Montana L. Kruske

May 2020

Dr. Eileen G. Ernenwein, Chair

Dr. Ingrid Luffman

Dr. Michael Whitelaw

Keywords: Ground Penetrating Radar, GPR, Geophysics, 400 MHz, 350 MHz HS

ABSTRACT

Stacking the Odds for Better GPR: An Antenna Comparison

by

Montana L. Kruske

Ground penetrating radar (GPR) is limited by depth penetration and signal-to-noise ratio (SNR), impacting the ability to resolve subsurface features. Stacking, a process of averaging multiple scans in the same location, improves SNR. Digital antennas are capable of stacking at much higher rates than analog antennas. Four sites were examined using a GSSI SIR-4000 GPR unit with a 400 MHz analog antenna and a 350 MHz digital “hyperstacking” (350 HS) antenna. Sites represent various soil conditions, with known features. Data were compared qualitatively and quantitatively for differences in antenna outputs. Visual inspection of radargrams indicate a reduction in noise in the 350 HS data compared to the 400 MHz data. Quantitative assessments identified significant differences in standard deviation of radar reflection amplitude occurring at depth with both antennas and a reduction in noise and marginal increases in depth of penetration in low-loss conditions with the 350 MHz HS antenna.

DEDICATION

This thesis is dedicated to my parents and my sister who believed in my continued pursuit of knowledge. Also, in memoriam to my paternal grandmother Betty Kruske, who taught me that a woman is capable of anything that she sets her mind to. “Everyone has inside of her a piece of good news. The good news is that you don’t know how great you can be, how much you can love, what you can accomplish, and what your potential is.” -Anne Frank

ACKNOWLEDGEMENTS

I wish to express my sincere appreciation to my advisor Dr. Eileen G. Ernenwein for supporting me, challenging me, and believing in a project which was different than your standard research. I appreciate the time you spent with me collecting and analyzing data, and developing presentations. Eileen, you have changed the way I think about GPR data and taught me more about remote sensing than I thought possible.

I would like to acknowledge the School of Graduate Studies at East Tennessee State University for awarding me funding to support this research. I would also like to acknowledge GSSI for providing me access to the hyperstacking antenna which allowed me to conduct my research.

I would like to thank Kevin McMinn, Porcha McCurdy, and Monica Ayala for assisting with data collection at the various sites. Without you all, data collection would not have been possible. Specifically, Porcha and Monica, I appreciate all the times you guys listened to me explain my data in order to try to understand each of my sites. I would also like to express my genuine appreciation to my committee members: Eileen Ernenwein, Ingrid Luffman, and Mick Whitelaw, for the feedback regarding this thesis.

Finally, I must express my profound gratitude to my parents and my sister for providing me with consistent support and continuous encouragement throughout the years of school and the process of writing this thesis. I would not have been able to accomplish this without you. Thank you.

TABLE OF CONTENTS

ABSTRACT.....	2
DEDICATION.....	3
ACKNOWLEDGEMENTS.....	4
LIST OF TABLES.....	7
LIST OF FIGURES.....	8
CHAPTER 1. INTRODUCTION.....	13
What is Geophysics?.....	13
What is GPR?.....	13
GPR Theory.....	14
Noise.....	15
What is the Nature of GPR Data?.....	15
Relationship between Data Resolution and Depth of Penetration.....	16
Limitations of GPR.....	16
Hilbert Transform.....	17
What is Stacking?.....	17
State of the Technology.....	18
Statement of Research Problem.....	18
Research Questions.....	19
Background of Sites.....	19
Paleochannel Outcrop.....	20
Taylor Cemetery.....	22
Carter Mansion.....	23
Runion.....	23
CHAPTER 2. METHODS.....	25
Field Methods.....	25
Paleochannel Outcrop.....	26
Taylor Cemetery.....	27
Carter Mansion.....	29
Runion.....	30
Data Processing.....	31
GNSS Mapping.....	31

Microtopographic Mapping	32
GPR Processing	32
Gridding Radargrams for Raster Analysis	36
Qualitative Analysis	37
Statistical Comparison	39
CHAPTER 3. RESULTS	40
Paleochannel.....	40
Qualitative Analysis.....	40
Quantitative Analysis.....	49
Taylor Cemetery.....	50
Qualitative Analysis.....	50
Marked Burials.....	50
Unmarked Burials.....	57
Quantitative Analysis.....	64
Marked Burials.....	64
Unmarked Burials.....	65
Carter Mansion.....	67
Qualitative Analysis.....	67
Quantitative Analysis.....	77
Runion	79
Qualitative Analysis.....	79
Quantitative Analysis.....	92
CHAPTER 4. DISCUSSION.....	96
CHAPTER 5. CONCLUSION.....	104
REFERENCES	105
APPENDIX: Coordinates of Site Locations.....	112
VITA.....	113

LIST OF TABLES

Table 1.1. GSSI GPR Antenna Specifications.....19

Table 3.1. P-values from the Kruskal-Wallis Test at a depth interval of 0.2 meters
indicating significant differences between the three antenna frequencies49

Table 3.2. Pairwise comparison of the antennas from the Kruskal-Wallis test results.....50

Table 3.3. P-values from the Mann-Whitney U Test at depth interval of 0.2 meters
indicating significant differences between the two antenna frequencies64

Table 3.4. P-values from the Mann-Whitney U Test at depth interval of 0.2 meters
indicating significant differences between the two antenna frequencies65

Table 3.5. P-values from the Mann-Whitney U Test at depth interval of 0.2 meters
indicating significant differences between the two antenna frequencies66

Table 3.6. P-values from the Mann-Whitney U Test at depth interval of 0.2 meters
indicating significant differences between the two antenna frequencies66

Table 3.7. P-values from the Mann-Whitney U Test at depth interval of 0.2 meters
indicating significant differences between the two antenna frequencies at all
depths77

Table 3.8. P-values from the Mann-Whitney U Test at depth interval of 0.2 meters
indicating significant differences between the two antenna frequencies at all
depths78

Table 3.9. P-values from the Mann-Whitney U Test at depth interval of 0.2 meters
indicating significant differences between the two antenna frequencies93

Table 3.10. P-values from the Mann-Whitney U Test at depth interval of 0.2 meters
indicating significant differences between the two antenna frequencies94

Table 3.11. P-values from the Mann-Whitney U Test at depth interval of 0.2 meters
indicating significant differences between the two antenna frequencies95

LIST OF FIGURES

Figure 1.1. Location of the four study sites (red stars) where GPR surveys were conducted	20
Figure 1.2. Interpreted channel outcrop at Paleochannel site location	21
Figure 1.3. Interpreted stratigraphy at Paleochannel location	22
Figure 2.1. Workflow of field data collection.....	26
Figure 2.2. Location of Paleochannel Outcrop transects with respect to the eroded hillside and showing site conditions	26
Figure 2.3. Approximate location of survey grid A as indicated by the red box at Taylor Cemetery	28
Figure 2.4. Survey grid B located over two elongated topographic depressions.....	28
Figure 2.5. Location of transects with respect to Carter Mansion and showing site conditions	29
Figure 2.6. Location of transects and site conditions at Runion.....	30
Figure 2.7. Data processing and analysis workflow	31
Figure 2.8. Data from Carter Mansion (A) 350 MHz hyperstacking antenna (B) 400 MHz antenna showing the visual difference in gain value with the same gain curve applied.....	34
Figure 2.9. Frequency spectra of an unfiltered radargram (A) 350 MHz HS antenna (B) 400 MHz antenna.....	35
Figure 2.10. Data from Taylor Cemetery (A) topographic profile (B) topographically corrected 350 MHz HS radargram	36
Figure 2.11. RGB color model.....	38
Figure 3.1. Radargrams at the Paleochannel (A) 270 MHz antenna (B) 350 MHz HS antenna (C) 400 MHz antenna	42
Figure 3.2. Radargrams for the Paleochannel (A) 270 MHz antenna (B) 350 MHz HS antenna (C) 400 MHz antenna.	43

Figure 3.3. Topographically corrected radargrams for the Paleochannel (A) 270 MHz antenna (B) 350 MHz HS antenna (C) 400 MHz antenna	44
Figure 3.4. Hilbert transform radargrams for the Paleochannel (A) 270 MHz antenna (B) 350 MHz HS antenna (C) 400 MHz antenna.....	45
Figure 3.5. Hilbert transform radargrams for the Paleochannel (A) 270 MHz antenna (B) 350 MHz HS antenna (C) 400 MHz antenna.....	46
Figure 3.6. Graph of standard deviation with depth for the Paleochannel	47
Figure 3.7. Color composite of all three antennas for the Paleochannel	48
Figure 3.8. Radargrams line 003 marked burials at Taylor Cemetery (A) 350 MHz HS antenna (B) 400 MHz antenna	52
Figure 3.9. Radargrams line 006 marked burials at Taylor Cemetery (A) 350 MHz HS antenna (B) 400 MHz antenna	52
Figure 3.10. Hilbert transform radargrams of marked burials at Taylor Cemetery (A) 350 MHz HS antenna line 003 (B) 400 MHz antenna line 003 (C) 350 MHz HS antenna line 006 (D) 400 MHz antenna line 006.....	53
Figure 3.11. Hilbert transform radargrams of marked burials at Taylor Cemetery (A) 350 MHz HS antenna line 003 (B) 400 MHz antenna line 003 (C) 350 MHz HS antenna line 006 (D) 400 MHz antenna line 006.....	53
Figure 3.12. Graph of standard deviation with depth for Line 003 over a marked burial	54
Figure 3.13. Graph of standard deviation with depth for Line 006 over a marked burial	55
Figure 3.14. Color composite marked burials line 003, 400 MHz antenna is the blue and green band and 350 MHz HS antenna is the red band.....	56
Figure 3.15. Color composite marked burials line 006, 400 MHz antenna is the blue and green band and 350 MHz HS antenna is the red band.....	56
Figure 3.16. Radargrams line 003 possible unmarked burials at Taylor Cemetery (A) 350 MHz HS antenna (B) 400 MHz antenna.....	58
Figure 3.17. Radargrams line 004 possible unmarked burials at Taylor Cemetery (A) 350 MHz HS antenna (B) 400 MHz antenna.....	59

Figure 3.18. Hilbert transform radargrams of unmarked burials at Taylor Cemetery (A) 350 MHz HS antenna line 003 (B) 400 MHz antenna line 003 (C) 350 MHz HS antenna line 004 (D) 400 MHz antenna line 004.....	59
Figure 3.19. Hilbert transform radargrams of unmarked burials at Taylor Cemetery (A) 350 MHz HS antenna line 003 (B) 400 MHz antenna line 003 (C) 350 MHz HS antenna line 004 (D) 400 MHz line antenna 004.....	60
Figure 3.20. Graph of standard deviation with depth for line 003 over an unmarked burial	61
Figure 3.21. Graph of standard deviation with depth for line 004 over an unmarked burial	62
Figure 3.22. Color composite of unmarked burials line 003, 400 MHz antenna is the blue and green band and 350 MHz HS antenna is the red band	63
Figure 3.23. Color composite of unmarked burials line 004, 400 MHz antenna is the blue and green band and 350 MHz HS antenna is the red band	63
Figure 3.24. Radargrams for Carter Mansion line 015 (A) 350 MHz HS antenna (B) 400 MHz antenna.....	69
Figure 3.25. Zoomed in view of radargrams for Carter Mansion line 015 (A) 350 MHz HS antenna (B) 400 MHz antenna, showing the marginal increase in depth of penetration.....	69
Figure 3.26. Hilbert transform radargrams for Carter Mansion line 015 (A) 350 MHz HS antenna (B) 400 MHz antenna, showing the hyperstacking noise.....	70
Figure 3.27. Hilbert transform radargrams for Carter Mansion line 015 (A) 350 MHz HS antenna (B) 400 MHz antenna showing the hyperstacking noise reduction. Red arrows indicate areas of noise.....	70
Figure 3.28. Radargrams for Carter Mansion line 024 (A) 350 MHz HS antenna (B) 400 MHz antenna.....	71
Figure 3.29. Zoomed in view of radargrams for Carter Mansion line 024 (A) 350 MHz HS antenna (B) 400 MHz antenna, showing the marginal increase in depth of penetration.....	71
Figure 3.30. Hilbert transform radargrams for Carter Mansion line 024 (A) 350 MHz HS antenna (B) 400 MHz antenna showing the hyperstacking noise reduction.....	72

Figure 3.31. Hilbert transform radargrams for Carter Mansion line 024 (A) 350 MHz HS antenna (B) 400 MHz antenna showing the hyperstacking noise reduction. Red arrows indicate areas of noise.....	72
Figure 3.32. Graph of standard deviation with depth for Carter Mansion Line 015	73
Figure 3.33. Graph of standard deviation with depth for Carter Mansion Line 024	74
Figure 3.34. Color composite of Carter Mansion line 015, 400 MHz antenna is the blue and green band and 350 MHz HS antenna is the red band	75
Figure 3.35. Color composite of Carter Mansion line 024, 400 MHz antenna is the blue and green band and 350 MHz HS antenna is the red band.	76
Figure 3.36. Radargram of linear feature on Runion line 002 (A) 350 MHz HS antenna (B) 400 MHz antenna.....	81
Figure 3.37. Hilbert transform radargram of linear feature on Runion line 002 (A) 350 MHz HS antenna (B) 400 MHz antenna.....	82
Figure 3.38. Hilbert transform radargram of linear feature on Runion line 002 (A) 350 MHz HS antenna (B) 400 MHz antenna.....	82
Figure 3.39. Radargram of linear feature on Runion line 014 (A) 350 MHz HS antenna (B) 400 MHz antenna.....	83
Figure 3.40. Hilbert transform radargram of linear feature on Runion line 014 (A) 350 MHz HS antenna (B) 400 MHz antenna.....	83
Figure 3.41. Hilbert transform radargram of linear feature on Runion line 014 (A) 350 MHz HS antenna (B) 400 MHz antenna.....	84
Figure 3.42. Radargram of linear feature on Runion line 018 (A) 350 MHz HS antenna (B) 400 MHz antenna.....	84
Figure 3.43. Hilbert transform radargram of linear feature on Runion line 018 (A) 350 MHz HS antenna (B) 400 MHz antenna.....	85
Figure 3.44. Hilbert transform radargram of linear feature on Runion line 018 (A) 350 MHz HS antenna (B) 400 MHz antenna.....	85
Figure 3.45. Graph of standard deviation with depth for Runion Line 002.....	86
Figure 3.46. Graph of standard deviation with depth for Runion Line 014.....	87

Figure 3.47. Graph of standard deviation with depth for Runion Line 018.....88

Figure 3.48. Color composite of Runion line 002, 400 MHz antenna is the blue and green band and 350 MHz HS antenna is the red band.....89

Figure 3.49. Color composite of Runion line 002, 400 MHz antenna is the blue and green band and 350 MHz HS antenna is the red band.....90

Figure 3.50. Color composite of Runion line 018, 400 MHz antenna is the blue and green band and 350 MHz HS antenna is the red band.....91

Figure 4.1. Independent-sample Kruskal-Wallis test of the Paleochannel site standard deviations between antenna groups98

CHAPTER 1. INTRODUCTION

What is Geophysics?

Geophysics is a subdiscipline of geoscience which studies earth's natural processes. Specifically, geophysics is the non-invasive subsurface examination of geological structures, groundwater, contamination, and human artifacts based on remotely sensed physical property variations occurring in the subsurface (EEGS 2019). Some geophysical techniques are considered invasive where equipment has to be inserted into the ground. Other techniques are non-invasive where the equipment passes over the ground. Geophysical techniques can be applied to different fields such as geology, archaeology, and engineering. Gathered data are analyzed and interpreted to understand the geological or archeological response of features occurring in the subsurface.

What is GPR?

Ground penetrating radar (GPR) is a geophysical technique used to non-invasively image the near-subsurface transmitting and receiving electromagnetic waves (Everett 2013; Reynolds 2013). A GPR system consists of three parts: a transmitter, a receiver, and a control unit. GPR antennas transmit and receive signals in all directions with a range of frequencies measured in megahertz (MHz), but are named for the center frequency. GPR antennas can be unshielded or shielded. Typically, unshielded antennas have separate transmitters and receivers. Due to the signal being transmitted in all directions unshielded antennas have difficulties with buildings, cars, people, or power lines, which result in reflections from them being recorded as part of the data. Shielded antennas have both the transmitter and receiver in one unit. However, antenna shielding reduces the amount of upward transmitted signal, thus producing a clearer signal. GPR has a wide range of applications such as analyzing cemeteries (e.g. Schultz, Collins and Falsetti

2006; Doolittle and Bellantoni 2010; Bigman 2013; Hansen, Pringle and Goodwin 2014; Diamanti and Annan 2019), geology (e.g. Słowik 2011; Hausmann et al. 2013; Andersen et al. 2018; Salinas Naval, Santos-Assunção and Pérez-Gracia 2018), hydrology (e.g. Doolittle et al. 2006; Klotzsche et al. 2018), and archaeology (e.g. Weaver 2006; Bigman et al. 2011; Verdonck et al. 2015; Welc et al. 2015). Depending on the geophysical application there is a range of frequency antennas which may be selected for the survey. Typically, GPR antennas range in frequency from 10 MHz to 1 GHz. Generally, lower frequency antennas penetrate deeper, but due to the size of the wave transmitted, they are only able to resolve larger features (Jol 1995; Smith and Jol 1995).

GPR Theory

GPR records reflections based on changes in the electromagnetic properties of sediments. Electromagnetic properties vary as a result of changes in water content, which is related to sediment grain-size and porosity (Roth et al. 1990; van Dam 2001). These variations in electromagnetic properties can cause stronger (more visible) or weaker (less visible) reflections. The electrical conductivity of sediments describes the movement of charge when an electrical field is present (Jol 2009). Resistance to the flow of charge leads to energy loss and/or dissipation (Jol 2009). Relative dielectric permittivity (RDP) is the ability of a material to store a charge when an electrical field is applied (Jol 2009; Everett 2013; Reynolds 2013). RDP is the primary diagnostic property used for GPR (Alsharahi, Driouach and Faize 2015). Materials such as air, sand, gravel, or crystalline rock tend to have lower RDPs compared to clay or water. Materials with higher RDPs or soil moisture tend to cause a GPR signal to attenuate. Attenuation in GPR is the loss of signal strength with depth. Therefore, GPR is most successful in low-

electrical loss materials (Jol 2009) and there are limits to the depth of penetration achievable due to antenna frequency, signal attenuation, and noise.

Noise

In GPR data, noise is considered to be any unwanted signal that contaminates the signal of interest thus making it difficult to discriminate reflections (Kim et al. 2007). Direct coupling errors or antenna ringing appears as horizontal or periodic noise events that result from internal GPR components (Kim et al. 2007; Mostapha et al. 2019). External sources of noise occur in GPR data because the signal is transmitted in all directions (Mostapha et al. 2019). Random noise occurs as fluctuations in frequencies from external sources, varying both spatially and temporally (Oskooi et al. 2018). GPR signal becomes weaker with increasing depth of penetration. Weakened signal contaminated with noise makes it challenging to discern reflections at depth. The noise floor is considered to be an area where the GPR signal of interest is weaker than the noise. Signal-to-noise ratio (SNR) is the comparison of signal strength to background noise, where background noise is any unwanted signal.

What is the Nature of GPR Data?

GPR data are raster data stored in radargrams. Radargrams are the recorded depth profiles of the reflection amplitudes, which can be positive or negative, and results in alternating light or dark colors on a radargram. Post-acquisition GPR signal processing reduces the random interference (noise) allowing clearer visualization of radar reflections (Wang et al. 2017). Radargrams depict two-way travel time recorded in nanoseconds (ns), which is converted to depth using a velocity estimation. Radar velocity varies based on differences in soil composition, dielectric constant, and soil moisture, and can be estimated using a technique called hyperbolic velocity analysis (Jol 2009). Software is used to match the ideal shape of a velocity-specific

hyperbola to recorded hyperbolas in the data, in order to estimate an average depth based on the time it took the signal to transmit and reflect back to the receiving antenna.

Relationship between Data Resolution and Depth of Penetration

GPR antenna frequency impacts depth of penetration and data resolution (Davis and Annan, 1989; Jol, 1995; Smith and Jol, 1995; Jol, 2009). There is an inverse relationship between antenna frequency and depth of penetration, where antenna frequency increases depth of penetration decreases. Studies indicate that higher frequency antennas, for example 400 MHz or 500 MHz, are only able to penetrate approximately two meters into the ground with high resolution (Jol, 1995; Smith and Jol, 1995). A lower frequency antenna, for example 100 MHz, will penetrate deeper into the ground but provide lower resolution data (Jol, 1995; Smith and Jol, 1995). GPR data resolution refers to the smallest size feature that is able to be detected, and resolution is constrained by the inverse relationship between frequency and wavelength. However, there is a direct relationship between antenna frequency and data resolution, where antenna frequency increases data resolution increases; this due to the shorter radar wavelength emitted from the antenna. The frequency of the antenna impacts the depth of penetration and the relative size of objects that can be resolved.

Limitations of GPR

GPR is limited by depth penetration and signal-to-noise ratio (SNR), which both impact the ability to resolve subsurface features. GPR antennas are known to have limited depth penetration due to attenuation. The noise floor is the depth at which there is no discernable signal (Stec and Susek 2018). Different objects in the environment can transmit frequencies that are recorded in data as background noise; this noise is considered to be external noise. An example of high frequency background noise is that associated with cell phones or electrical lines.

Internal noise is noise which is generated by the internal components of the GPR. Data processing such as filtering has the ability to reduce noise. Noise that occurs at the same frequency as the signal of interest, however, cannot be filtered out without also removing the signal of interest.

Hilbert Transform

Hilbert transform is a post-acquisition data process used to show the envelope of the radar pulse. Hilbert transform is mathematically based on the use of a Fourier transform to shift negative values within the radar pulse envelope (Goodman and Piro 2013). Generally, Hilbert transform can be thought of as taking the absolute value of the radar pulse (Wang et al. 2017). Hilbert transform is a useful way to visualize radar data, because areas of strong or weak reflections are prominent without the alternating positive and negative signal. Stronger pulses appear darker than weaker pulses.

What is Stacking?

Stacking was first used in seismic data, as a process that averages traces collected in the same location to reduce random noise, thus improving the SNR. Stacking can be applied to GPR data both during data collection and during post-acquisition data processing (Goodman and Piro 2013). The theory of stacking is that rather than just collecting one GPR trace and saving it, multiple GPR traces are collected and averaged together. Thus, random noise is eliminated and only repetitive signals remain. Stacking can often be confused with smoothing, but they are not the same process. Smoothing is a data processing step which returns only the naturally smooth signals based on a moving average (Goodman and Piro 2013).

State of the Technology

GPR is a relatively new technology, which did not become readily available until the mid-1970s. GPR manufacturers continue to improve the speed of GPR equipment, allowing stacking at a faster rate (Goodman and Piro 2013). GPR manufacturers are developing antennas capable of a high rate of stacking which reduces recorded noise. The new technology, referred to as hyperstacking, patented by Feigin (Geophysical Survey Systems Inc. 2014) uses high-speed interpolated sampling to reduce noise. Feigin (2017) describes high-speed interpolated sampling as a method to recover all or most of the radar reflection information with less noise. Therefore, high-speed interpolated sampling is equivalent to the geophysical term “stacking.” Feigin and Cist (2016) show that the GSSI 350 MHz hyperstacking antenna is capable of doubling the depth of penetration, compared to the 400 MHz antenna, in low-loss soils. However, Feigin and Cist (2016) show that in high-loss soils there is not much performance difference between the two antennas.

Statement of Research Problem

It is known in the geophysical community that there is a trade-off between depth of penetration and data resolution. New technology has the ability to improve depth of penetration and reduce the recorded noise (Feigin and Cist 2016). This analysis seeks to fill a knowledge gap surrounding the hyperstacking antenna, due to the lack of research and literature about the antenna. Feigin and Cist (2016) have shown that the hyperstacking antenna dramatically improves depth of penetration and reduces noise. However, these studies have not been verified and results have not been duplicated. Feigin is the primary author and patent holder of existing information about the hyperstacking antenna. While Feigin’s claim is exciting for the future potential of GPR, it is necessary to independently test the validity of his claim. Thus, it is

important to compare antennas of similar frequencies (Table 1.1) in a variety of geological and environmental settings, to understand the qualitative and quantitative differences between them.

Table 1.1. GSSI GPR Antenna Specifications

<i>GPR Antenna Specifications</i>			
	Hyperstacking	400 MHz	270 MHz
Frequency	350 MHz	400 MHz	270 MHz
Depth Range	0-12m	0-4m	0-6m
Resolution	High	Moderate	Low

Research Questions

CHAPTER 1. Does the 350 MHz hyperstacking antenna reduce random noise when compared to the 400 MHz analog antenna?

CHAPTER 2. Is the 350 MHz hyperstacking antenna able to increase depth of penetration compared to the 400 MHz analog antenna (the closest available frequency)? If so, is this true in all four test sites, which test different soil conditions?

Background of Sites

Four sites were examined to compare depth of penetration and noise reduction between the 350 MHz HS and the 400 MHz antennas. The sites are located in northeastern, TN (Figure 1.1). The Paleochannel and Taylor Cemetery sites represent high-loss soils, which were used to test the antennas in less than ideal conditions. Carter Mansion and Runion represent low-loss soil, which were used to test the antennas in optimal conditions.

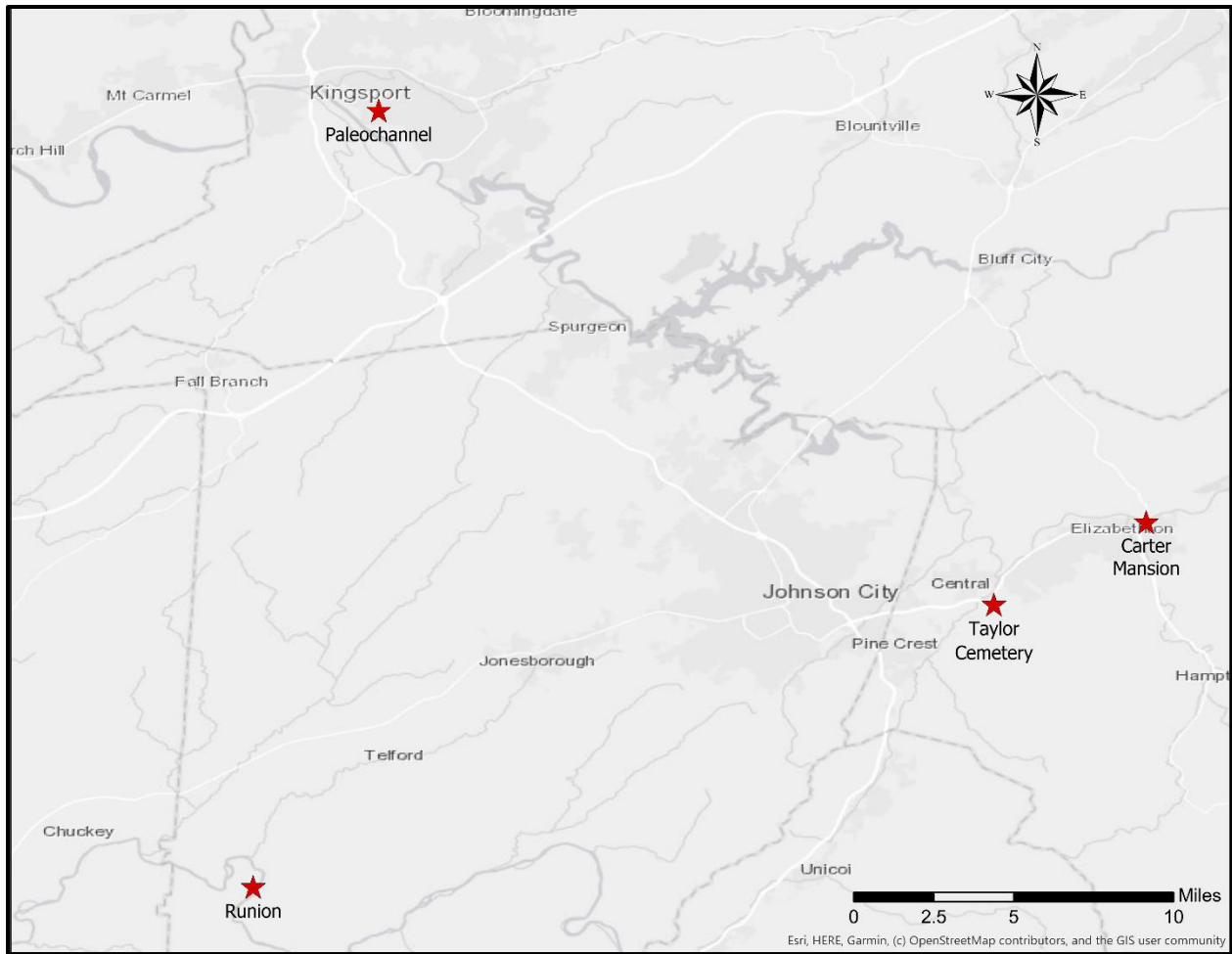


Figure 1.1. Location of the four study sites (red stars) where GPR surveys were conducted

Paleochannel Outcrop

This site is located in Kingsport, central Sullivan County, TN (Figure 1.1). This location exposes a paleochannel outcrop on an eroded hillside (Figure 1.2). The feature is assumed to be a paleochannel due to proximity to the meandering South Holston River (Tennessee Valley Authority 1949). As a river meanders, channels are abandoned, and over time, are left to fill in with sediments in fining-upward sequences. A channel can be defined by the presence of an incised surface, cross-bedding, point bar sequences, thalweg, and alternating sediment layers (Wyatt and Temples 1996). This site was chosen in order to map stratigraphy using GPR,

because the exposed geological structure makes it possible to ground truth the outcrop (Figure 1.3). It would be expected that a channel would have dipping reflectors and/or a wavy appearance in the radargram (Wyatt and Temples 1996). Soils at the site are in the Holston-Urban land complex (HuC) and range from loam to clay loam occurring on the high stream terraces in the Southern Appalachian Ridge and Valley area (Davis 1994). The ground at this location was uneven due to soil subsidence and plant roots.



Figure 1.2. Interpreted channel outcrop at Paleochannel site location

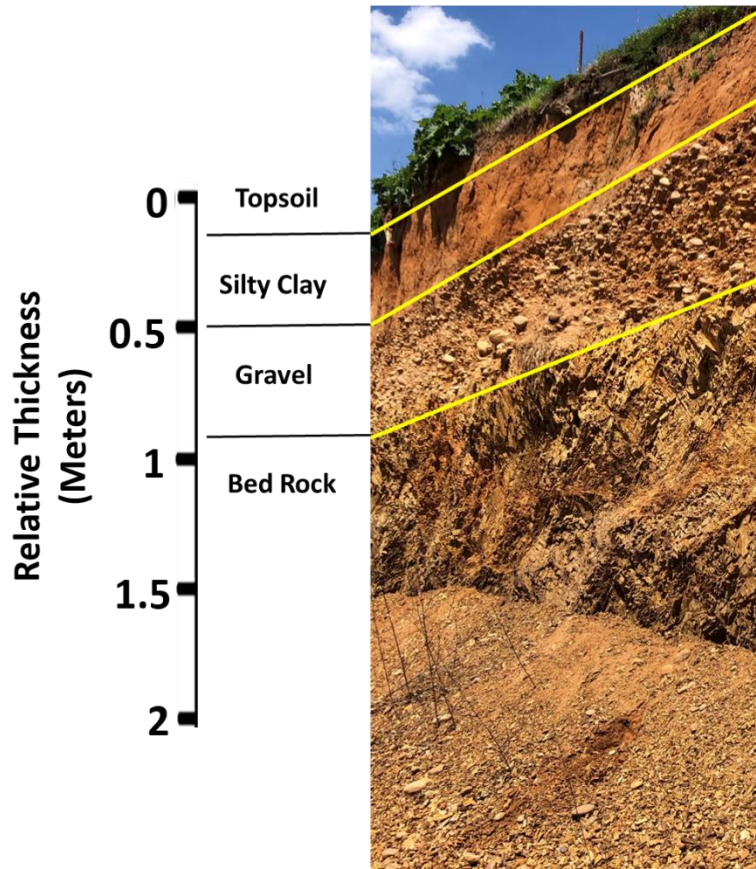


Figure 1.3. Interpreted stratigraphy at Paleochannel location

Taylor Cemetery

This site is located in western Carter County, TN (Figure 1.1). The cemetery is maintained by Sycamore Shoals State Historic Park and the Taylor family. It is a historic hilltop cemetery dating back to the late 18th to early 19th century. The Taylor family was influential in northeast TN during the time of the Watauga Settlement in the late 18th century. The cemetery contains both marked and unmarked burials. Generally, there is a hyperbolic reflection associated with burials (Schultz, Collins and Falsetti 2006). GPR reflections vary depending on the method of burial (Hansen, Pringle and Goodwin 2014). Two small surveys were conducted at

the site, one over marked burials and the other over topographic depressions (unmarked burials). Previous GPR surveys at the site provided limited knowledge due to the soils and soil moisture conditions, which attenuated GPR signal. The soils at this site are Braxton silt loam (BrD2) ranging from silty loam to clay, which is derived from the limestone bedrock that forms the ridges and side slopes (Hartgrove 2000).

Carter Mansion

This site is located in northern Carter County, Elizabethton, TN (Figure 1.1), and is managed by the Sycamore Shoals State Historic Park. The Carter Mansion was built in the late 18th century by John and Landon Carter, members of the influential Carter family, during the Watauga Settlement in the late 18th century. The mansion is the oldest standing frame house within the State of Tennessee (Ernenwein and Cannon 2017). Native Americans used the land as a seasonal camp for centuries before the Carters' claimed the land. Typically, Native American burials occur in the flexed, fetal position, where the GPR signal reflects off the head (Doolittle and Bellantoni 2010). Most historic burials, in contrast, are extended. Both flexed and extended graves appear as hyperbolic reflections in GPR data, but extended burials are longer. Previous geophysical and archaeological research indicates that there are both Native American and historical burials on the property, as well as other archaeological features (Ernenwein and Cannon 2017). The soils at the site are Colvard fine sandy loam (Cn) on the floodplain of the Watauga River (Hartgrove 2000).

Runion

This site is located in southwestern Washington County, near Limestone, TN (Figure 1.1). Runion is a protohistoric Native American village located on the floodplain of the Nolichucky River. Previous archaeological research and radiocarbon dates suggest that the

village was occupied during the mid- 16th to mid-17th century (Ernenwein and Franklin 2017). The Native American village at Runion was a large village featuring a townhouse (Ernenwein and Franklin 2017). Previous geophysical research located a linear feature in close proximity to the village and the Nolichucky River. The linear feature may be a fortification ditch or palisade used to defend the village from attack. It is similar to Etowah, a Mississippian (1,000 AD to 1,500 AD) fortified village located in northwestern Georgia (Cobb and King 2005). Etowah consists of a defensive ditch and palisade encompassing the village, which was analyzed via geophysics and archeological excavation (Bigman et al. 2011). The palisade at Etowah was recognized in the magnetic gradiometer data, due to being burned (Bigman et al. 2011). At Runion the linear feature appears in both magnetic gradiometer and GPR data, and is consistent with a palisade feature such as Etowah (Ernenwein and Franklin 2017). The feature may also be consistent with typical meandering floodplain stratigraphy such as an abandoned channel due to proximity to the Nolichucky River. In GPR data, channel stratigraphy created by lateral accretion may appear as dipping reflectors (Wyatt and Temples 1996). Reflections which are discontinuous can indicate a gravel bed (Nimnate et al. 2017). The soils at this site are floodplain deposits from the Nolichucky River. Specifically, the soils are Buncombe loamy fine sand (By) which can range from fine sandy loam to fine sandy gravel (Elder 1958).

CHAPTER 2. METHODS

Radar data were collected from four sites using both antennas. Sites were selected to reflect two low-loss soil environments and two high-loss soil environments. Post-acquisition data processing was required to analyze the visual and quantitative differences. Visual interpretation and image analysis of sample transects from the four sites were used to evaluate the qualitative differences between the antennas. Statistical analysis of the data was used to evaluate the quantitative differences between the antennas.

Field Methods

Data collection was carried out in August of 2019 in northeast Tennessee, at the four sites, over the course of a week. Precipitation data from the ETSU Ross Hall weather station indicates that, prior to the survey, there had been little to no precipitation accumulation over the previous 2 weeks. Generally, the same workflow was followed at each of the four sites (Figure 2.1). Prior to conducting the surveys each site was walked to determine the best survey profile orientation. Survey setup included placing measuring tapes as references to keep the survey lines straight. Global Navigation Satellite Systems (GNSS) points were collected at each of the four sites using a real time kinematic (RTK) system to provide reference of the location to the corners of the survey grids. At the paleochannel outcrop and Taylor Cemetery, GNSS points were collected along transects to collect elevation data. Surveys were conducted using a GSSI GPR with SIR-4000 control unit. Two different antennas, a 350 MHz hyperstacking (HS) digital antenna and 400 MHz analog antenna, were used. Only at the paleochannel site was a third antenna used: a 270 MHz analog antenna. At Carter Mansion and Runion, survey grids were collected in a zig-zag pattern, which is a back and forth pattern that allows for continuous data collection. GPR profiles were spaced 0.5 m apart.

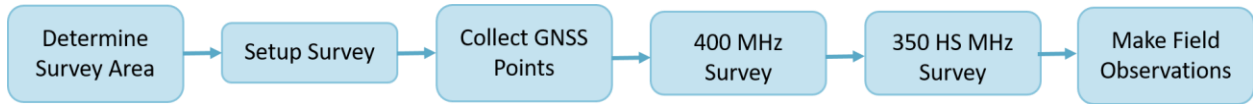


Figure 2.1. Workflow of field data collection

Paleochannel Outcrop

Two GPR transects approximately 14 meters long were collected over the paleochannel outcrop in Kingsport, Tennessee with all three frequency antennas (Figure 2.2). All three antenna transects were collected in both North to South and South to North directions, for a total of six transects. GNSS points were collected with a point spacing of one meter. However, a higher density of points was collected where there was visible sediment slumping. The data were collected with 1024 samples per scan, 32 bits per sample, 100 scans per meter, and a time window of 100 ns.



Figure 2.2. Location of Paleochannel Outcrop transects with respect to the eroded hillside and showing site conditions

Taylor Cemetery

Two small grids were surveyed at the Taylor Cemetery, located near Johnson City, Tennessee. The survey was conducted following some light misty rain that occurred earlier in the morning. Survey grid A was 3 x 4 meters and encompassed two headstones, two presumed footstones, and associated burial plots (Figure 2.3). Survey grid B was 3 x 4 meters and encompassed two elongated topographic depressions with no associated gravestones (Figure 2.4). The grids were surveyed in a zig-zag pattern with a 0.5 meter spacing between transects using both a 400 MHz antenna and a 350 MHz HS antenna. Data collection began in the southwest corner of each grid. The data were collected with 1024 samples per scan, 32 bits per sample, 100 scans per meter, and a time window of 100 ns. GNSS points were collected at the corners of both grids and additional points were taken every 10-20 cm in survey grid B to map topographic change.

Drone photography was collected for a portion of Taylor Cemetery in October 2019 using the DJI Phantom 3 Advanced quadcopter. Photos were collected in manual flight mode below the tree canopy. These photos were processed to create a digital elevation model (DEM), which was used to topographically correct the GPR. The camera used was the standard 12.4 megapixel Sony EXMO, which comes with the DJI Phantom 3 Advanced package. Generally, the flight path was in the North to South direction with at least 80% photographic overlap. Both vertical and oblique photos were collected. The total flight duration was approximately 50 minutes which used all three batteries.

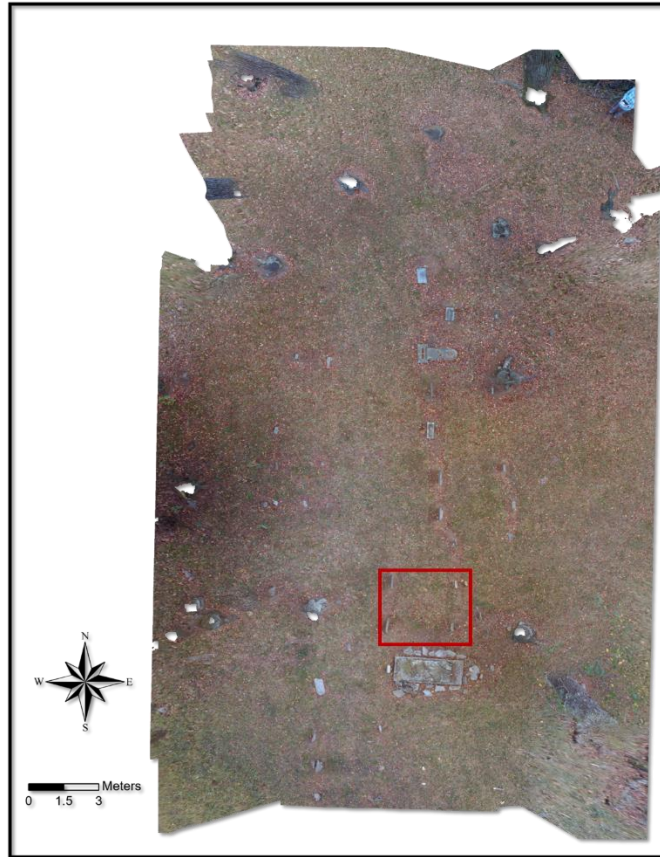


Figure 2.3. Approximate location of survey grid A as indicated by the red box at Taylor Cemetery



Figure 2.4. Survey grid B located over two elongated topographic depressions

Carter Mansion

A 20 x 20 meter grid was surveyed at the Carter Mansion which is located in Elizabethton, Tennessee (Figure 2.5). Previous geophysical research indicated that historic and Native American burials are present on the property. The survey was conducted in a zig-zag pattern, with a line spacing of 0.5 meters, starting in the Southwest corner of the grid. GNSS points were collected at the corners of the grid using an RTK. The survey was conducted in a light misty rain. The data were collected with 1024 samples per scan, 32 bits per sample, 100 scans per meter, and a time window of 100 ns.



Figure 2.5. Location of transects with respect to Carter Mansion and showing site conditions

Runion

A 20 x 30 meter grid was surveyed at Runion which is a protohistoric Native American village located on the floodplain of the Nolichucky River in western Washington County, TN (Figure 2.6). Previous geophysical research identified a linear feature surrounding the protohistoric village. The grid was oriented perpendicular to the linear feature. The survey was conducted in a zig-zag pattern with line spacing of 0.5 meters starting in the southwest corner of the grid. GNSS points were collected at the corners of the grid using an RTK system. The data were collected with 1024 samples per scan, 32 bits per sample, 100 scans per meter, and a time window of 120 ns.



Figure 2.6. Location of transects and site conditions at Runion

Data Processing

Data processing was conducted using seven different software packages in order to qualitatively and quantitatively analyze the differences between antennas (Figure 2.7). First, topography data were converted from World Geodetic System of 1984 (WGS84) into Universal Transverse Mercator (UTM) zone 17N using ArcGIS Pro. Topography data for survey grid A at Taylor Cemetery were extracted from a DEM created using Agisoft Metashape Professional (2006). Next, GPR data were processed using GPR-Slice 7, and then extracted as ASCII files for qualitative and quantitative analysis. Next, Surfer 13 was used to grid data from the extracted ASCII file format. Then the grid files were converted to TIF files for raster analysis using ArcGIS Pro. Then the raster image files were analyzed in TerrSet. Next, data were extracted from TerrSet and graphed using Microsoft Excel. Finally, the data were statistically analyzed using IBM SPSS Statistics 25 (2017).

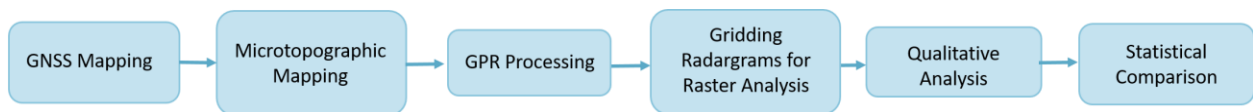


Figure 2.7. Data processing and analysis workflow

GNSS Mapping

Locations of survey grids and/or transects were recorded at each of the four sites. The GNSS points were downloaded from the RTK data collector as decimal degrees with reference to the World Geodetic System of 1984 (WGS84) as comma delimited values (CSV) files.

Specifically, at the Paleochannel Outcrop and Taylor Cemetery survey grid B, topographic data were displayed as point features using ArcGIS Pro Version 2.4.0 (ESRI 2019). The points were then projected to Universal Transverse Mercator (UTM) zone 17N, which is the coordinate

system required for topographic correction in GPR-Slice. Then using the ‘calculate geometry attributes tool’ the tables were updated to reflect the UTM coordinates. The new tables were exported from ArcGIS as .csv files for topographic correction in GPR-Slice.

Microtopographic Mapping

Structure-from-Motion (SfM) is a photogrammetry technique which can produce an orthomosaic and DEM from a 3-D point cloud derived from overlapping photos (Westoby et al. 2012). Aerial imagery collected from Taylor Cemetery were processed to create a DEM using the standard workflow within Agisoft Metashape Professional Version 1.6.1 (Agisoft 2006). Photos were added to Metashape and the GNSS locations were automatically loaded into the program. The photos were aligned in the software, by finding overlapping points in the photos (these are features or objects which appear in multiple photos) using a medium accuracy due to the time required to process all images. A medium accuracy is used to generally place the photos in the 3-dimensional location where the camera captured them. Then further alignment of the photos was completed to provide higher accuracy and correct for possible distortion. After optimization, a dense point cloud was built, which calculates the depth from photos. Due to processing constraints a medium quality dense point cloud was built using moderate depth filtering. Finally, a DEM was created from the dense point cloud.

GPR Processing

Radargrams were brought into GPR-Slice Version 7 (Goodman 2019) for data processing and visualization. A series of preprocessing steps were required to prepare the data for further processing and analysis within GPR-Slice. First, a new project was created for each dataset indicating the equipment used for data collection. The raw data files were copied into a directory stored within the project, which prevents user error in overwriting the originals. Information files

(info files) were created to allow the software to correctly read the datasets. Then the data were converted into the native format for GPR-Slice. During this process a constant gain value of 1 and a minus wobble of 36 ns was applied to the data. Applying a constant gain allows for the visualization of the first full waveform, which is required to locate time-zero. Using the minus wobble feature reduces some low frequency noise which can be associated with radio communications. The even data files were reversed to account for collection in the zig-zag survey style. Then artificial navigational markers were added as points of reference during visualization. A time-zero correction was then applied to the data, which aligns the average time-zero value for each line. Time zero is considered to be at the beginning of the first full waveform, which represents the ground surface (Everett 2013; Reynolds 2013). The first full wave form is identified as the first time the wave rises to a threshold value of 0.1 (10 %) deviation from the midline.

Preprocessed GPR data need further processing, which often includes applying gain, frequency bandpass, and background removal. Gain is applied to GPR data to compensate for signal attenuation with depth (Goodman and Piro 2013). A different gain curve was developed for each of the four locations due to variation in soil composition and signal attenuation. Gain curves developed for 350 MHz HS data were applied to analog datasets collected in the same locations. Gain values between the 350 MHz HS and 400 MHz antennas are different (Figure 2.8). A gain factor was determined and applied to the 400 MHz antenna to match gains. Before filtering there were visible differences in the frequency spectra between the two antennas with just a gain curve and time-zero correction applied to the data (Figure 2.9). There is dramatically more low frequency noise recorded by the 400 MHz antenna than the 350 MHz HS antenna, thus it can be assumed that there is less noise in the 350 MHz HS data compared to the 400 MHz

data. A frequency bandpass filter was applied to the datasets using a low cut-off value of 175 MHz and a high cut-off value of 800 MHz. These values were selected using the Butterworth method of filtering data which is based on removing frequency values that fall below half power and above double power of the selected antenna (Spathis 1983). Filter cut-off values were selected to encompass the full range of frequencies of interest captured by the 350 and 400 MHz antennas. A value of 175 MHz is half of 350 MHz and 800 MHz is double that of 400 MHz. A background removal filter was used for each of the datasets, which removes signals that occur in horizontal bands in radargrams. A hyperbola velocity estimation was used to convert two-way travel time to depth for each of the five sites. Datasets were then exported from GPR-Slice as ASCII files for further analysis.

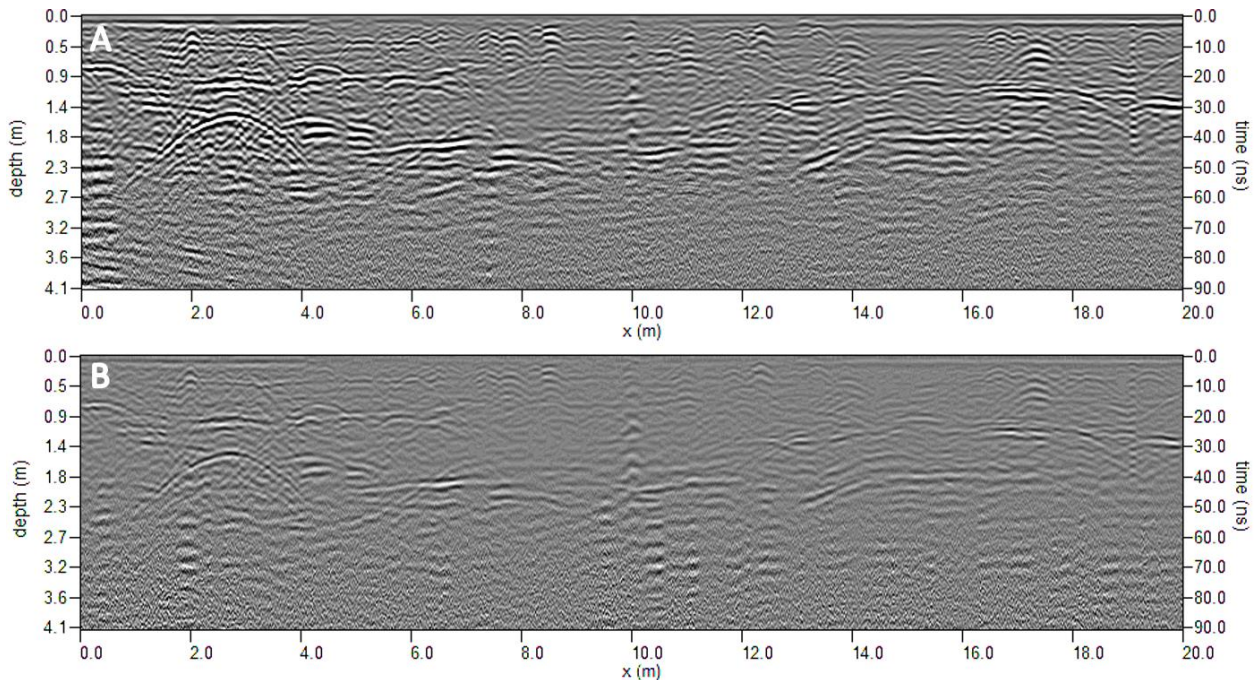


Figure 2.8. Data from Carter Mansion (A) 350 MHz hyperstacking antenna (B) 400 MHz antenna showing the visual difference in gain value with the same gain curve applied

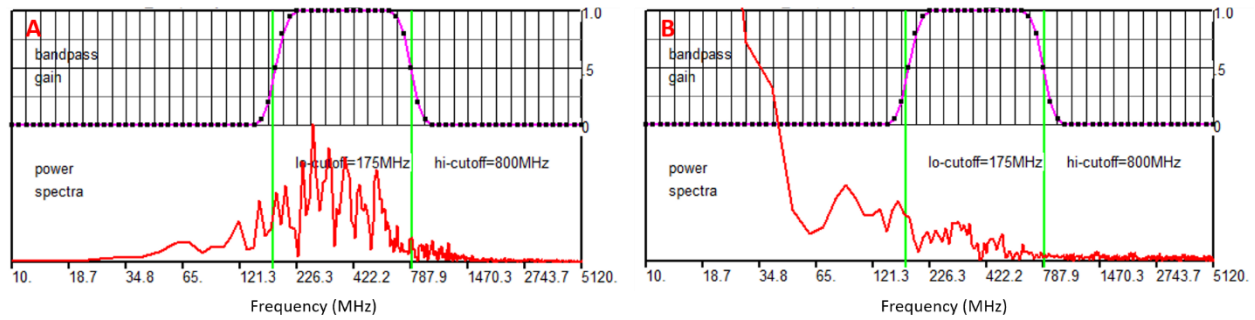


Figure 2.9. Frequency spectra of an unfiltered radargram (A) 350 MHz HS antenna (B) 400 MHz antenna

Data from Taylor Cemetery and the Paleochannel outcrop required a topographic correction due to the amount of elevation variation occurring at both sites. Topography files were generated from the GNSS points collected at each site, with average point spacing of between 0.1 to 0.3 meters. The software requires that the information files be edited to reflect the GNSS locations along the survey line. Then topography files can be imported into the software. An interpolated grid was created to make a continuous surface from GNSS points using the inverse distance weighted (IDW) method. IDW estimates values at unknown locations using a weighted average of neighboring values where more weight is applied to locations that are closer to the estimated value. A grid cell size of 0.005 m was selected and a search radius of 1 m in the x- and y-directions. Elevation profiles were extracted from the topographic grid, which then were applied to topographically correct the radargrams (Figure 2.10).

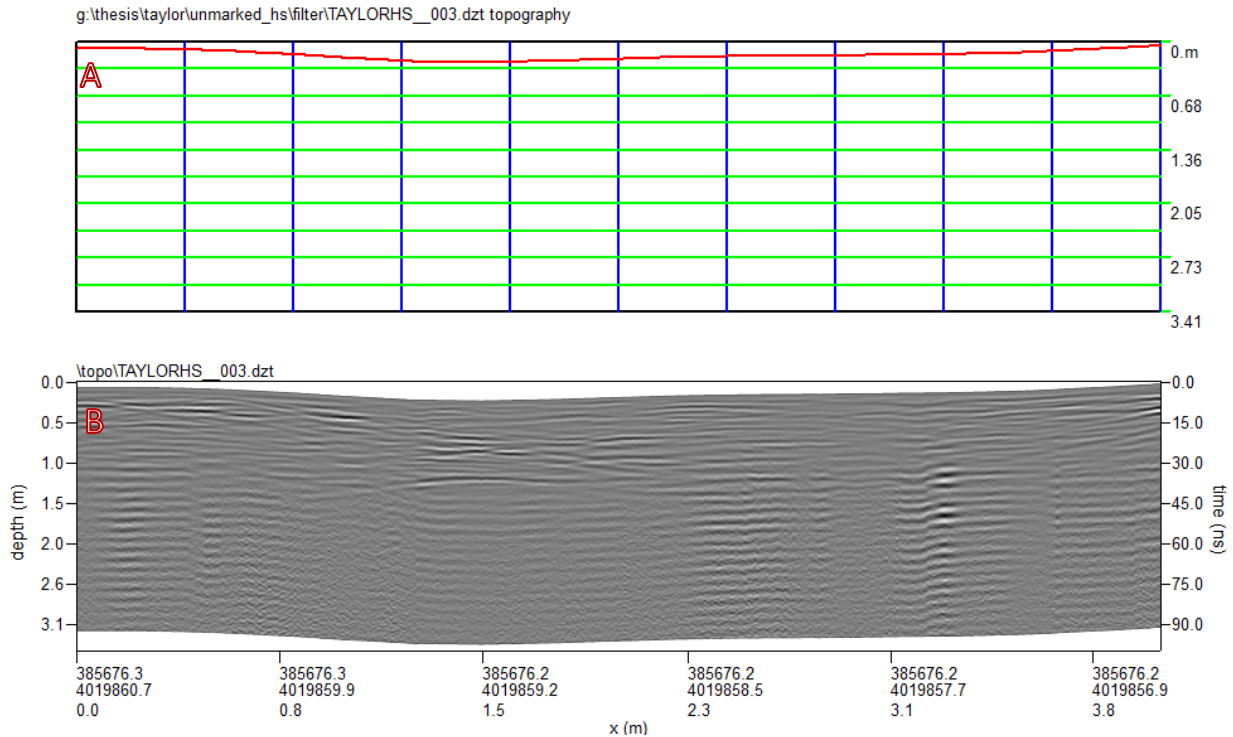


Figure 2.10. Data from Taylor Cemetery (A) topographic profile (B) topographically corrected 350 MHz HS radargram

Gridding Radargrams for Raster Analysis

The ASCII files were opened and edited in notepad to remove the extra information from the header. Then in Surfer Version 13 (Golden Software 2015) the ASCII files were gridded into x-, y-, and z- values using x-, z-, and a- values, respectively. This gridding process was necessary so that the radargrams could be brought in to TerrSet software. The new x- values represent horizontal distance along the radargram. The new y- values represent depth below ground surface. The new z- values represent the amplitude response of the reflected signal. The gridding method was set to nearest neighbor with a search distance of 0.01 m for both x- and y- directions. This was done to minimize change in the values as exported from GPR-Slice. The number of nodes in the x-direction was selected for each site based on the length of the line multiplied by 100, which is the sampling density used for the original data. The number of nodes in the y-

direction for each site was based on the number of samples of the processed radargram. Grid files were generated and saved for further analysis.

Qualitative Analysis

The grid files were converted to TIF files Arc GIS Pro using the copy raster function. TerrSet Version 18.31 (Clark Labs 2017) is a raster image analysis software that allows radargrams to be analyzed. Files were converted from TIF to Idrisi, a TerrSet specific file type. An image can be displayed as a composite of three primary color bands, which include: red, green, and blue (RGB). The RGB color model is an additive model, resulting in the color white when all three bands contribute 100% (Figure 2.11). If all three bands are in agreement the color will appear as a gray shade produced in the composite image. Where the bands disagree individual colors are produced. A combination of just the red and blue bands results in magenta. A combination of blue and green bands results in cyan. A combination of red and green bands results in yellow. In order to produce a composite image all three color bands must be used. The 400 MHz antenna is represented by two bands, (blue and green), resulting in cyan. The 350 MHz antenna is represented by one band, the red band. Radargrams from both antennas were used to create a color composite in TerrSet using the Composite tool. The three antennas used at the Paleochannel site each represented a single color band. The 270 MHz antenna is the green band, 400 MHz antenna is the blue band, and 350 MHz HS antenna is the red band in the color composite.

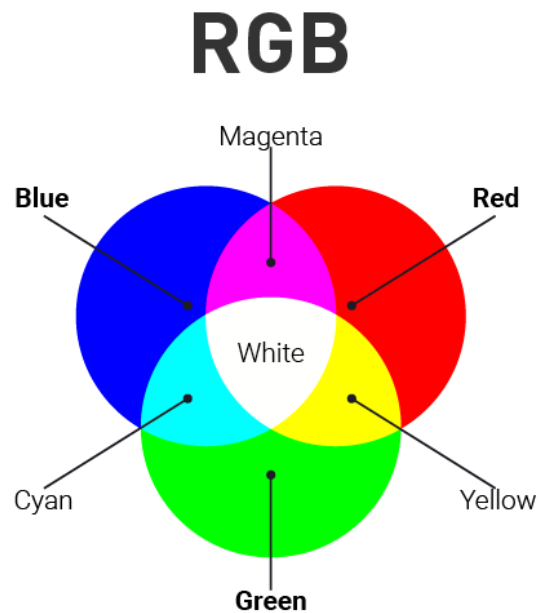


Figure 2.11. RGB color model

Radargrams were prepared for statistical analysis using TerrSet. Radargrams were standardized using the Standard tool in TerrSet, which calculates a standard score for the image (Equation 1). A constant value was added to the standardized radargrams to make all values positive. Then a moving window standard deviation filter was applied to the radargrams; the moving window was customized for each site based on the size of feature being analyzed. Then radargrams were generalized using the Contract tool in TerrSet to be one column with as many rows as the radargram originally contained, using the average pixel value for each row. The raster radargrams were converted to vector point data type, which allowed the data to be exported as a CSV file for the purpose of statistical analysis.

$$\text{Equation 1: Standard Score} = \frac{\text{Cell Value} - \text{Mean}}{\text{Standard Deviation}}$$

Statistical Comparison

CSV data files were prepared using Microsoft Excel. Graphs of the standard deviation of reflection amplitude were plotted to compare standard deviation changes with depth for each antenna. A 30 unit moving window average of standard deviation was calculated to smooth out the standard deviation curve. Depth measurements were grouped in 0.2 meter increments and antenna frequencies were assigned a grouping value. Separate spreadsheets were generated for each of the sites for use in IBM SPSS Statistics 25 (IBM 2017). The data were not normally distributed; therefore, a Mann-Whitney U test was selected for analysis of sites where only two antennas were used. The Mann-Whitney U test was used to compare variations in the standard deviation (dependent variable) between the antennas (grouping variable) within a 0.2 meter increment depth interval. The Kruskal-Wallis test was used to compare variations in standard deviation (independent variable) between all three antennas (dependent variable). A pairwise comparison of groups from the Kruskal-Wallis test was analyzed to determine which antennas were statistically different. P-values were examined to determine if there were statistically significant differences between antennas' standard deviation over the depth interval. Tables were made in Excel to show the significant p-values for each antenna at each site.

CHAPTER 3. RESULTS

Paleochannel

Qualitative Analysis

Estimated radar velocity was 0.12 meters per nanosecond and RDP was 6.25 for the Paleochannel. Visual examination of the three radargrams shows the noise floor to be at approximately 1 to 1.2 meters deep (Figure 3.1). Soils at this site seemed to limit the penetration depth due to GPR signal attenuation, which indicates a high-loss soil environment that makes imaging the channel difficult. Visually, it was observed that there was no advantage to using a lower frequency antenna (270 MHz) compared to higher frequency antennas (Figure 3.1). Approximately 24 to 27 meters along the radargram, at a depth of 0.6 meters, strong discontinuous reflections were observed. The topographically corrected radargrams provide more information about the imaged structure. A relatively continuous horizontal reflection was observed at approximately 0.9 meters depth (Figure 3.1), which was associated with a change in sediment grain size. Linear spikes of noise occur in all three radargrams, as indicated by the red arrows (Figure 3.2). Even with the topographic correction there doesn't appear to be any distinct channel features recorded in the radargrams (Figure 3.3). The noise floor was further confirmed by the Hilbert transform data (Figure 3.4). Linear spikes are observed easily in the Hilbert transform radargram data. The number of linear spikes (red arrows) (Figure 3.5), associated with the 270 MHz and 400 MHz antennas, is greater than that observed for the 350 MHz HS antenna (Figure 3.5B).

The graph of standard deviation of recorded radar amplitude (Figure 3.6), shows that in the upper 1 meter the 350 MHz HS antenna has a higher standard deviation value than the 270 MHz and 400 MHz antennas. Visually, the graph shows a transitional zone, from

approximately 1.5 to 2 meters depth, in radar amplitude before all the lines intersect at the point of complete signal loss, indicating that only noise was being recorded and no meaningful reflections. Following the point of intersection, the lines begin to separate where remaining noise in the 270 MHz and 400 MHz antennas is amplified in comparison to the 350 MHz HS antenna. The three antennas used at the Paleochannel site each represented a single color band. The 270 MHz antenna was the green band, 400 MHz antenna was the blue band, and 350 MHz HS antenna was the red band in the color composite. The color composite shows agreement between all three antennas as indicated by shades of gray colors at approximately 24 to 27 meters along the radargram (Figure 3.7). Agreement between the 270 MHz and 400 MHz antennas was observed in the color composite by the presence of the color cyan in the lower half of the radargram, as noise. Agreement between the 270 MHz and 350 MHz HS antennas was indicated by yellow in the color composite image at approximately 14 meters on the radargram. Agreement between the 400 MHz and the 350 MHz HS antennas was marked by the color magenta in the lower half of the radargram and is associated with noise.

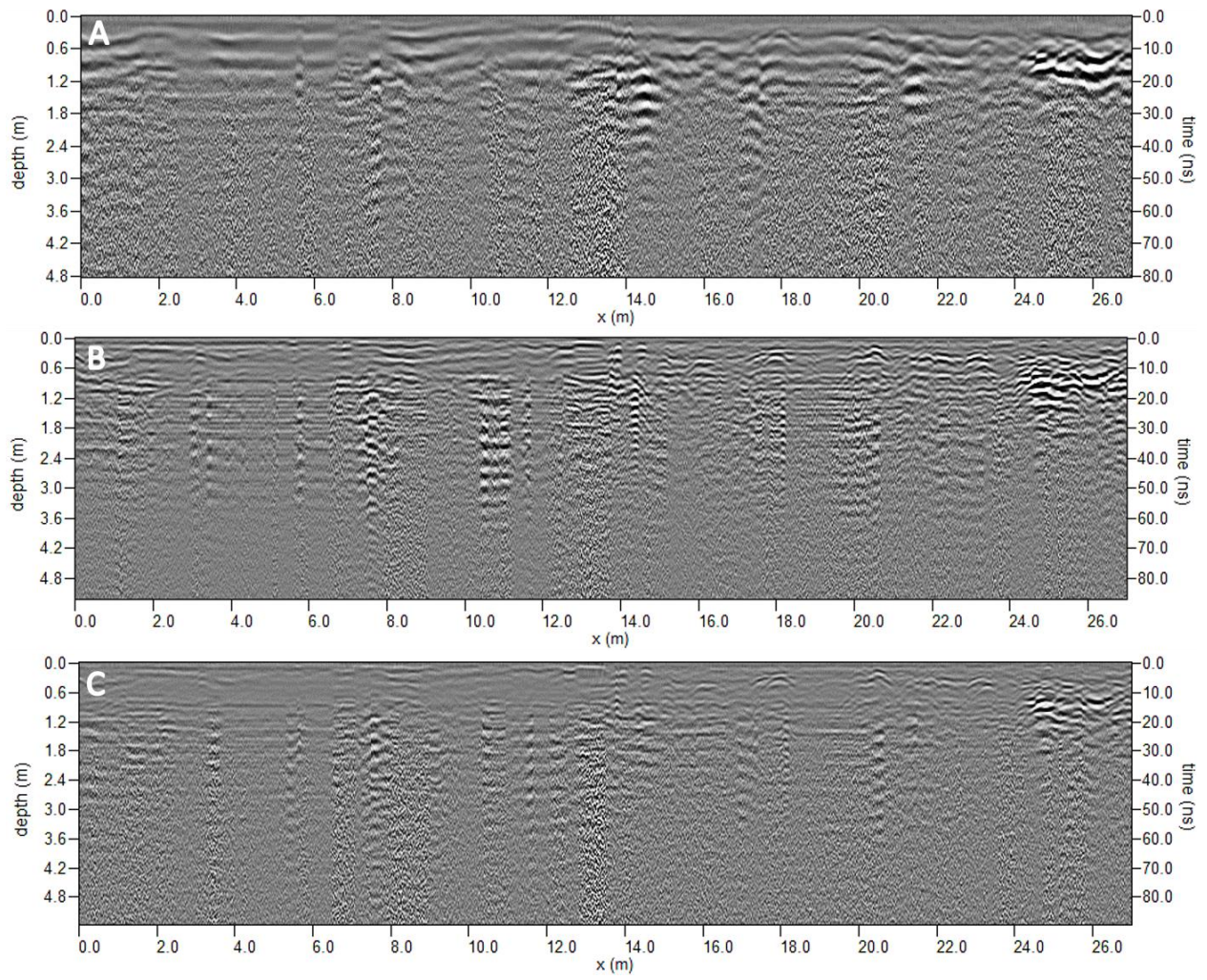


Figure 3.1. Radargrams at the Paleochannel (A) 270 MHz antenna (B) 350 MHz HS antenna (C) 400 MHz antenna

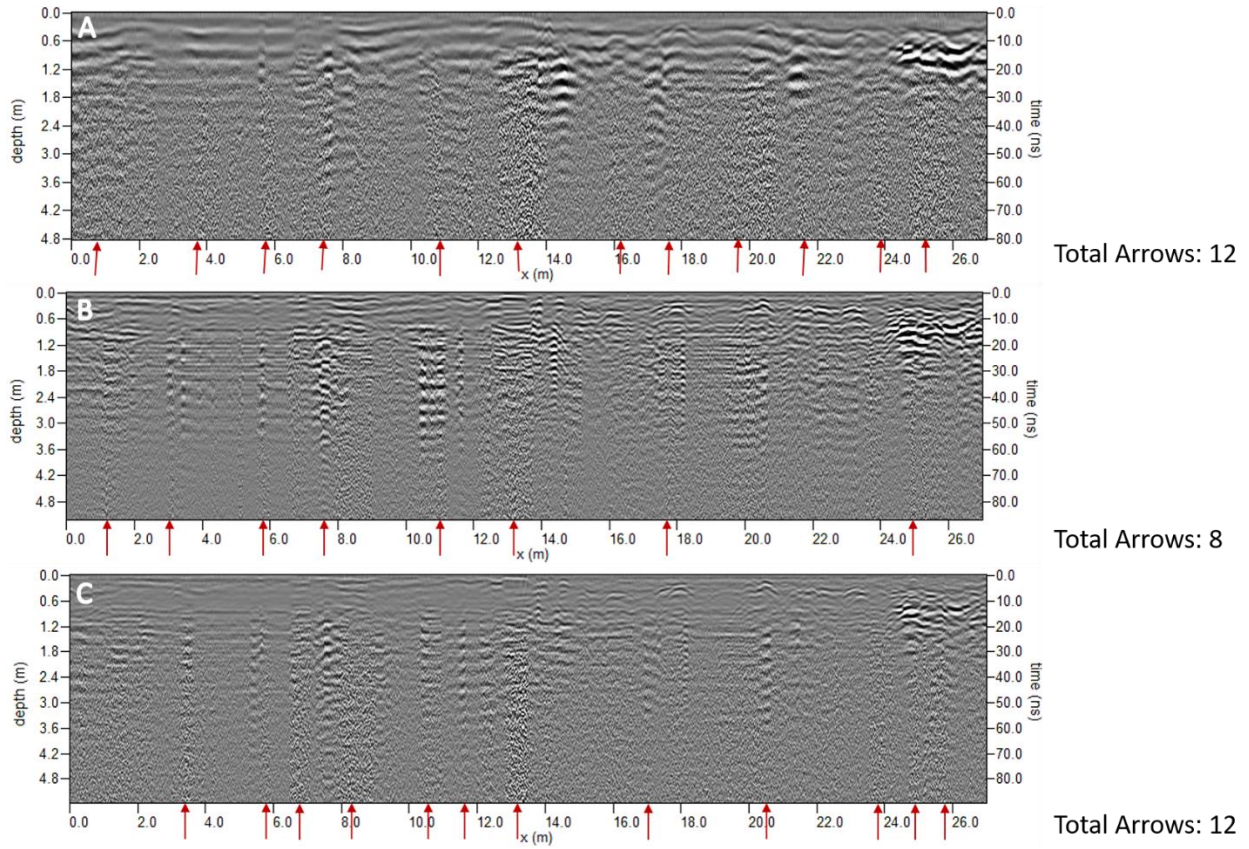


Figure 3.2. Radargrams for the Paleochannel (A) 270 MHz antenna (B) 350 MHz HS antenna (C) 400 MHz antenna. Areas of noise are indicated by the red arrows.

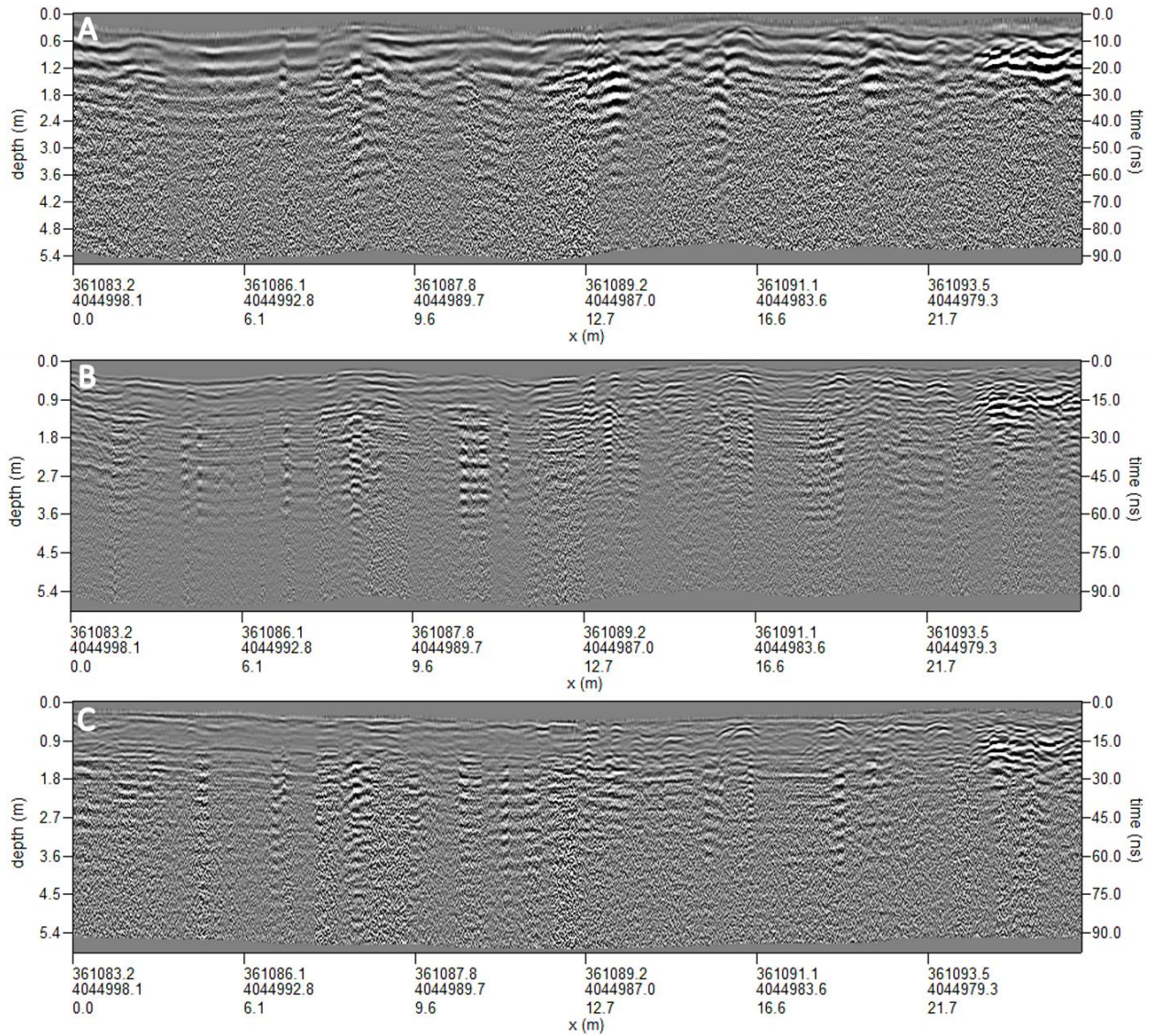


Figure 3.3. Topographically corrected radargrams for the Paleochannel (A) 270 MHz antenna (B) 350 MHz HS antenna (C) 400 MHz antenna

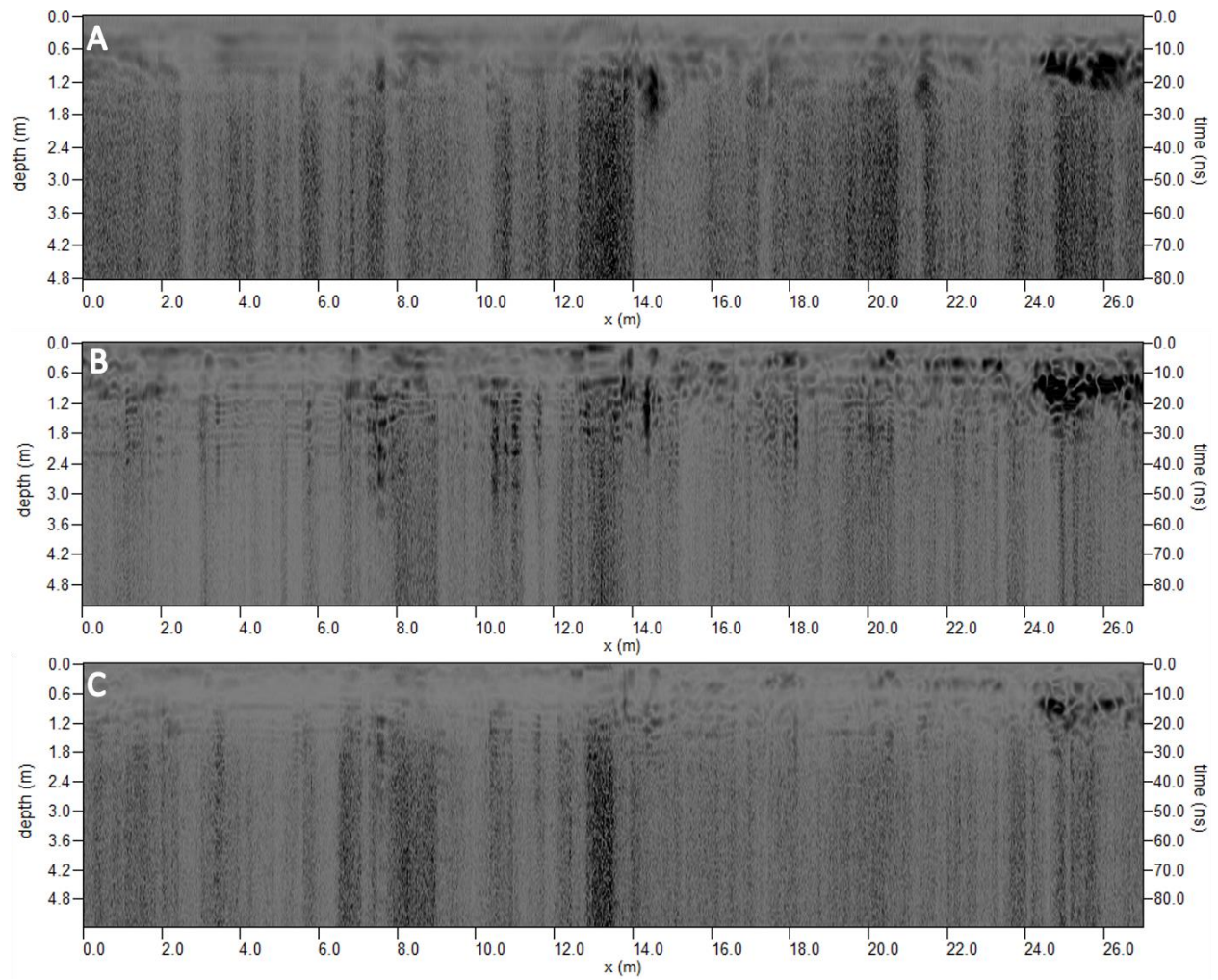


Figure 3.4. Hilbert transform radargrams for the Paleochannel (A) 270 MHz antenna (B) 350 MHz HS antenna (C) 400 MHz antenna

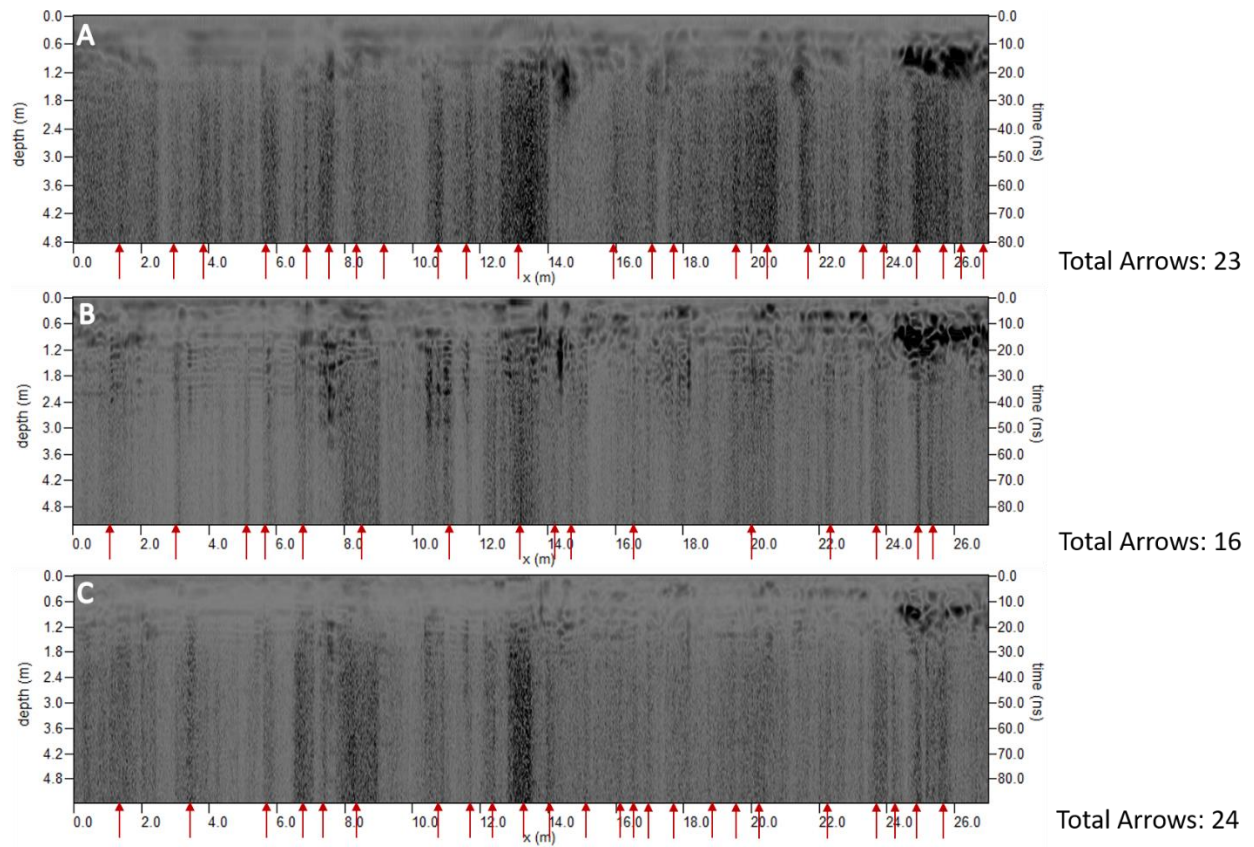


Figure 3.5. Hilbert transform radargrams for the Paleochannel (A) 270 MHz antenna (B) 350 MHz HS antenna (C) 400 MHz antenna. Areas of noise are indicated by the red arrows.

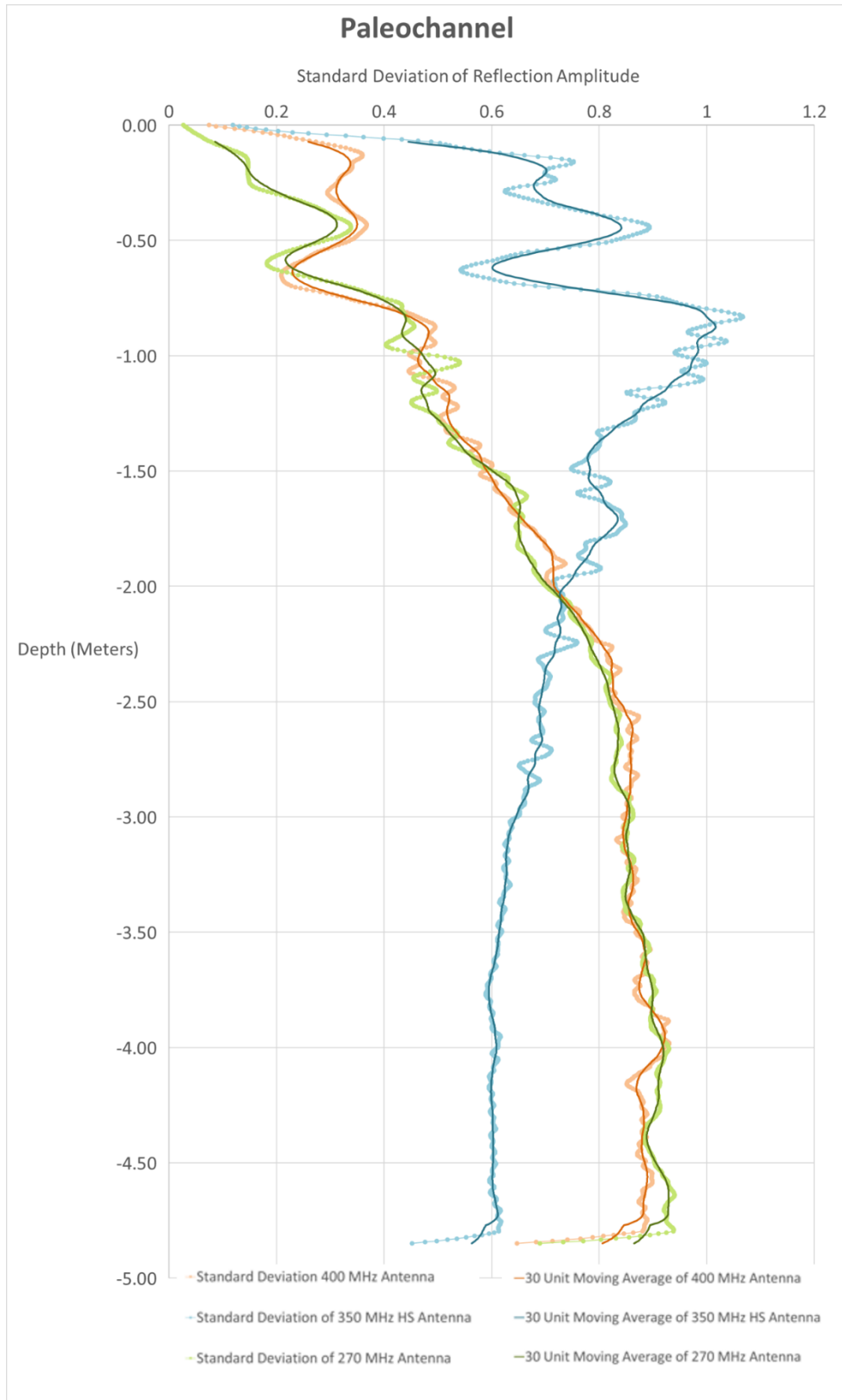


Figure 3.6. Graph of standard deviation with depth for the Paleochannel

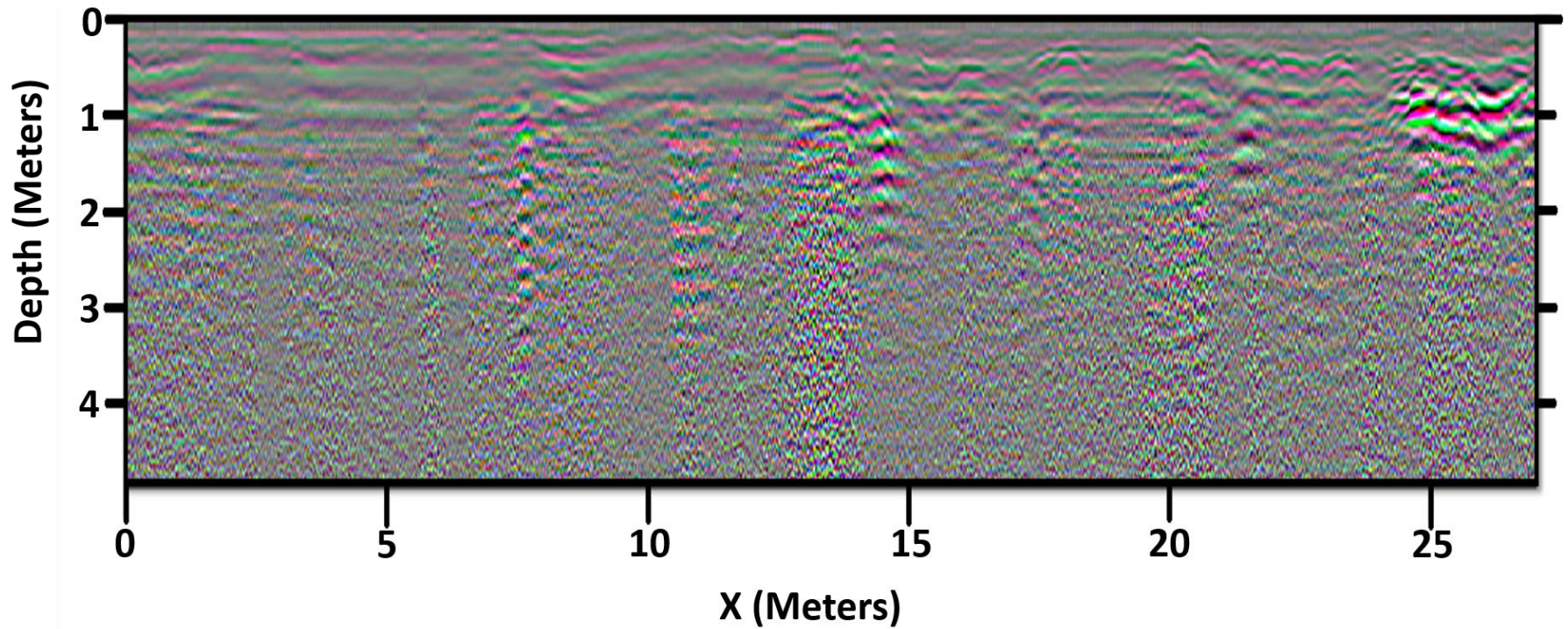


Figure 3.7. Color composite of all three antennas for the Paleochannel. 400 MHz antenna is the blue band, 270 MHz antenna is the green band, and 350 MHz HS antenna is the red band. Shades of grey indicate agreement between all three antennas. Yellow indicates agreement between the 270 MHz and the 350 MHz HS antennas. Cyan indicates agreement between the 270 MHz and the 400 MHz antennas. Magenta indicates agreement between the 400 MHz and the 350 MHz HS antenna.

Quantitative Analysis

Statistical analysis results indicate that there are significant differences ($p = 0.000$) at a confidence level of 95% occurring between the three antenna groups for all depths (Table 3.1). A pairwise comparison indicates a significant difference ($p = 0.000$) between the 350 MHz HS antenna and the 400 MHz and 270 MHz antennas (Table 3.2).

Table 3.1. P-values from the Kruskal-Wallis Test at a depth interval of 0.2 meters indicating significant differences between the three antenna frequencies

Paleochannel	
Kruskal-Wallis Test Results	
Depth (Meters)	P-Value
0.0 to 0.2	0.000
0.2 to 0.4	0.000
0.4 to 0.6	0.000
0.6 to 0.8	0.000
0.8 to 1.0	0.000
1.0 to 1.2	0.000
1.2 to 1.4	0.000
1.4 to 1.6	0.000
1.6 to 1.8	0.000
1.8 to 2.0	0.000
2.0 to 2.2	0.000
2.2 to 2.4	0.000
2.4 to 2.6	0.000
2.6 to 2.8	0.000
2.8 to 3.0	0.000
3.0 to 3.2	0.000
3.2 to 3.4	0.000
3.4 to 3.6	0.000
3.6 to 3.8	0.000
3.8 to 4.0	0.000
4.0 to 4.2	0.000
4.2 to 4.4	0.000
4.4 to 4.6	0.000
4.6 to 4.8	0.000
<i>Significant at 0.05 Confidence Level</i>	

Table 3.2. Pairwise comparison of the antennas from the Kruskal-Wallis test results. Group 1 is the 400 MHz antenna, group 2 is the 350 MHz HS antenna, and group 3 is the 270 MHz antenna.

Kruskal-Wallis Test Results		
Pairwise Comparison of Groups		
Groups	Significance	Adjusted Significance
3 to 1	0.840	1.000
3 to 2	0.000	0.000
1 to 2	0.000	0.000
<i>Significant at 0.05 Confidence Level</i>		

Taylor Cemetery

Qualitative Analysis

Marked Burials. Estimated radar velocity was 0.066 meters per nanosecond and RDP was 20.66 for Taylor Cemetery. Radargrams from two sample lines were collected over marked burials which were examined visually. Two hyperbolic reflections were observed at a depth of approximately 1 meter (Figure 3.8), which were the first appearances of burial reflections. The hyperbolic reflections continued to be observed on line 006 (Figure 3.9) at approximately the same depth of 1 meter, which is consistent with a historical burial. In both radargrams the noise floor was interpreted to occur at a depth of approximately 1.3 meters, due to the increase in random reflections (Figures 3.8 and 3.9). In both radargrams there was continuous horizontal banding seen in the 350 MHz HS antenna data (Figures 3.8 and 3.9). The Hilbert transform radargrams of the marked burials showed linear spikes of noise (Figure 3.10). Generally, it appears that there was a similar amount of linear noise spiking in both antennas (Figures 3.10 and 3.11). The Hilbert transform radargram data reveals weak point features, which represent and correspond to the marked burials.

The graphs of standard deviation of recorded radar reflection amplitude showed an increase in standard deviation at approximately 1 meter, which corresponded to an increased amplitude of the burial feature (Figures 3.12 and 3.13). Visually, the graph showed a transitional zone, from approximately 1 to 1.5 meters in depth, where there was an increase in noise. The lines intersected at approximately 1.5 to 2 meters indicating the point of complete signal loss, beyond which no meaningful reflections were recorded. This corresponds with radargram observations. Following the point of intersection, the lines separate where remaining noise in the 400 MHz antenna was amplified, in comparison to the 350 MHz HS antenna. Agreement between the 400 MHz and 350 MHz HS antennas at the location of the burials was indicated by the shade of gray in the color composite (Figures 3.14 and 3.15). Generally, it appeared that the 400 MHz data contained more noise in relation to data as indicated by the appearance of cyan in the lower half of the radargrams. However, noise that appeared only in the 350 MHz HS data is shown in red such as the striping between the burials between 2 to 2.5 meters along the x-axis (Figure 3.14).

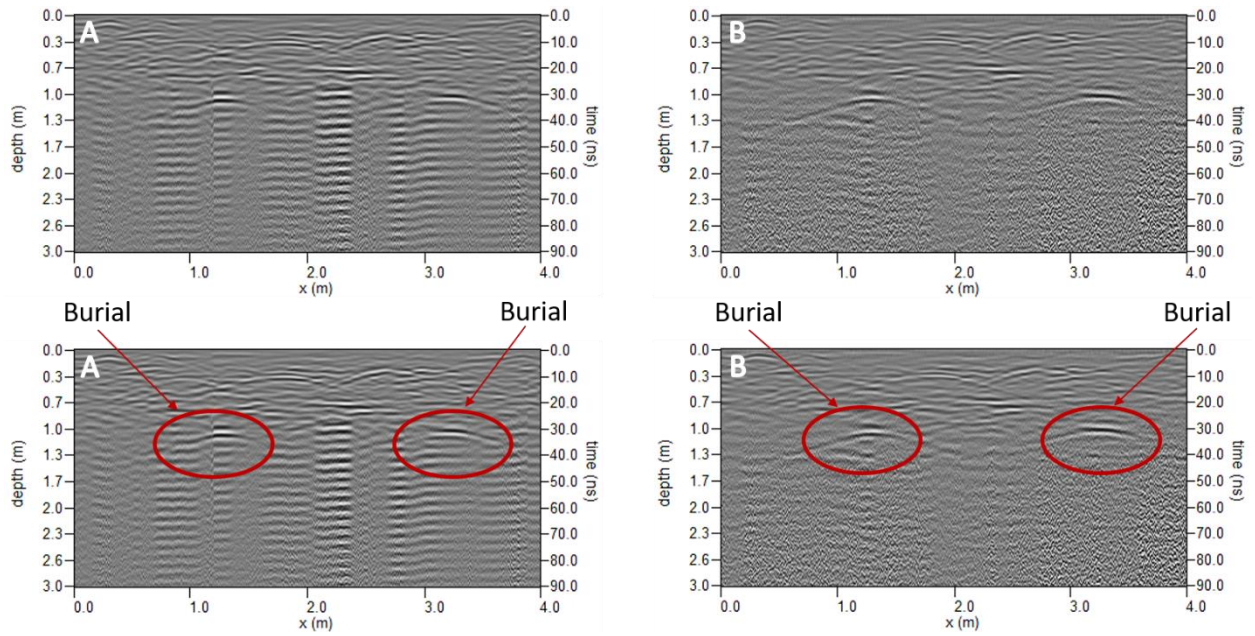


Figure 3.8. Radargrams line 003 marked burials at Taylor Cemetery (A) 350 MHz HS antenna (B) 400 MHz antenna

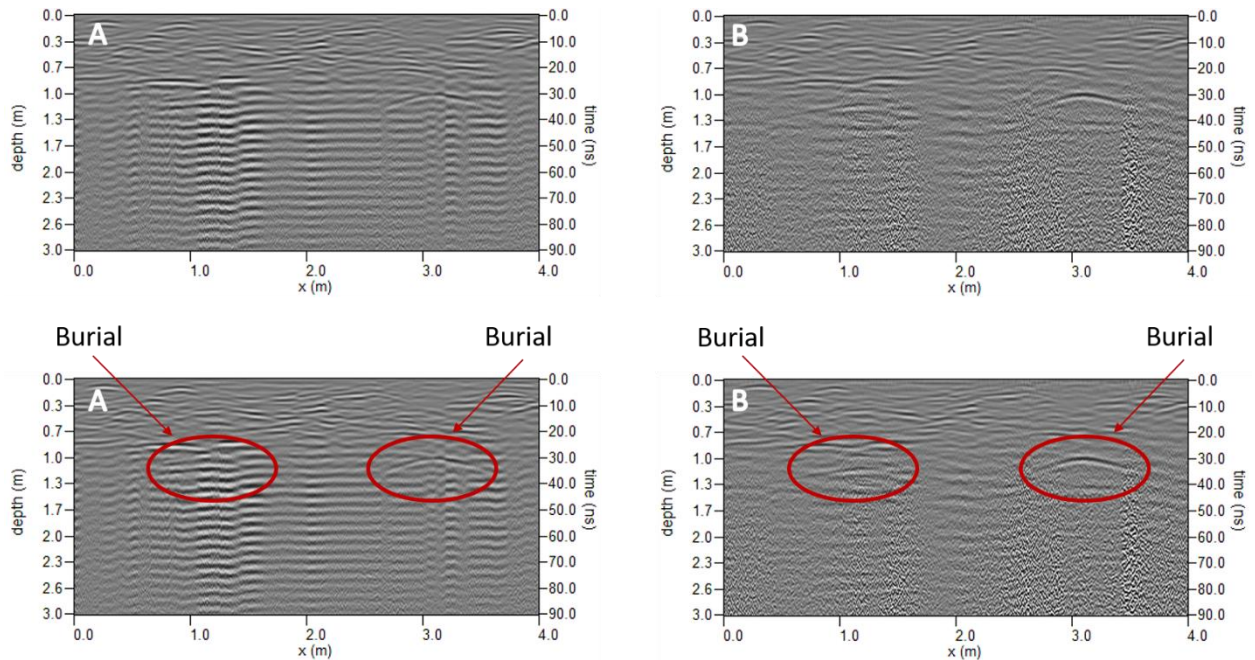


Figure 3.9. Radargrams line 006 marked burials at Taylor Cemetery (A) 350 MHz HS antenna (B) 400 MHz antenna

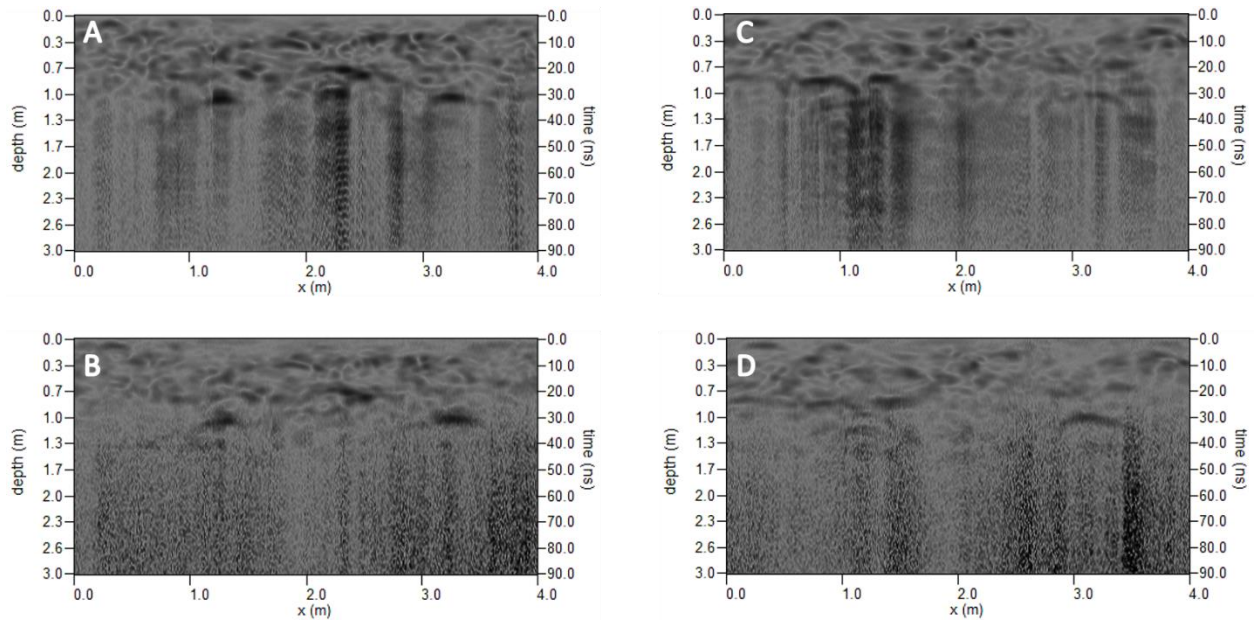


Figure 3.10. Hilbert transform radargrams of marked burials at Taylor Cemetery (A) 350 MHz HS antenna line 003 (B) 400 MHz antenna line 003 (C) 350 MHz HS antenna line 006 (D) 400 MHz antenna line 006

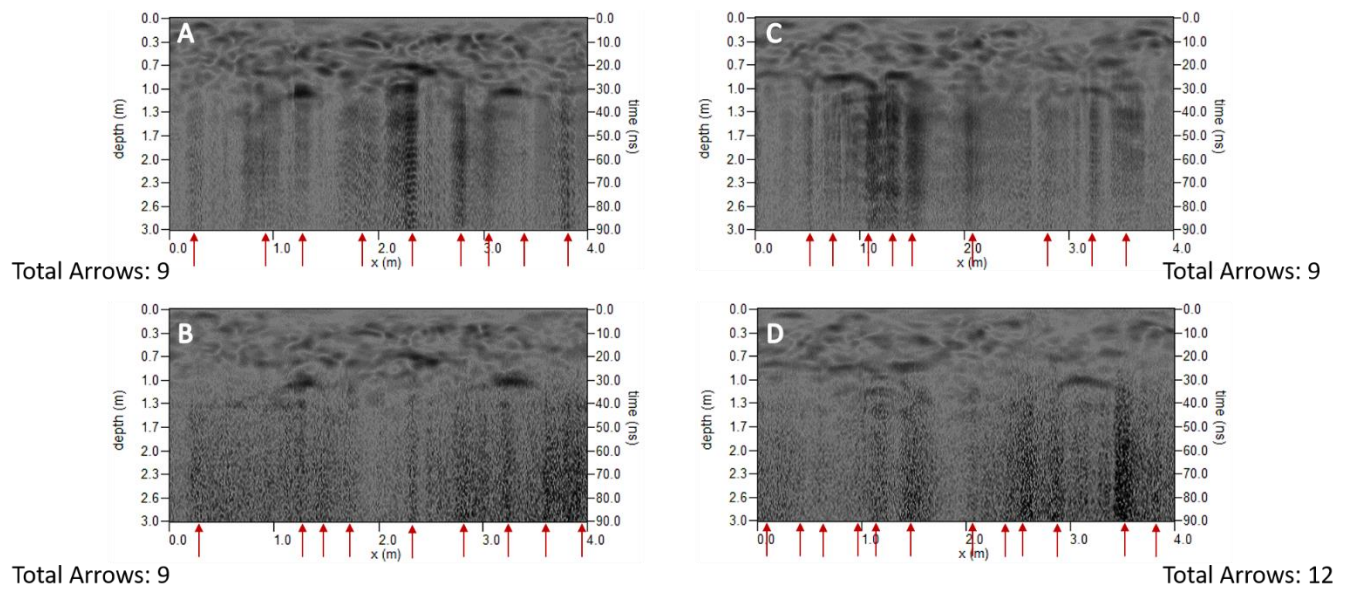


Figure 3.11. Hilbert transform radargrams of marked burials at Taylor Cemetery (A) 350 MHz HS antenna line 003 (B) 400 MHz antenna line 003 (C) 350 MHz HS antenna line 006 (D) 400 MHz antenna line 006. Red arrows indicate areas of noise.

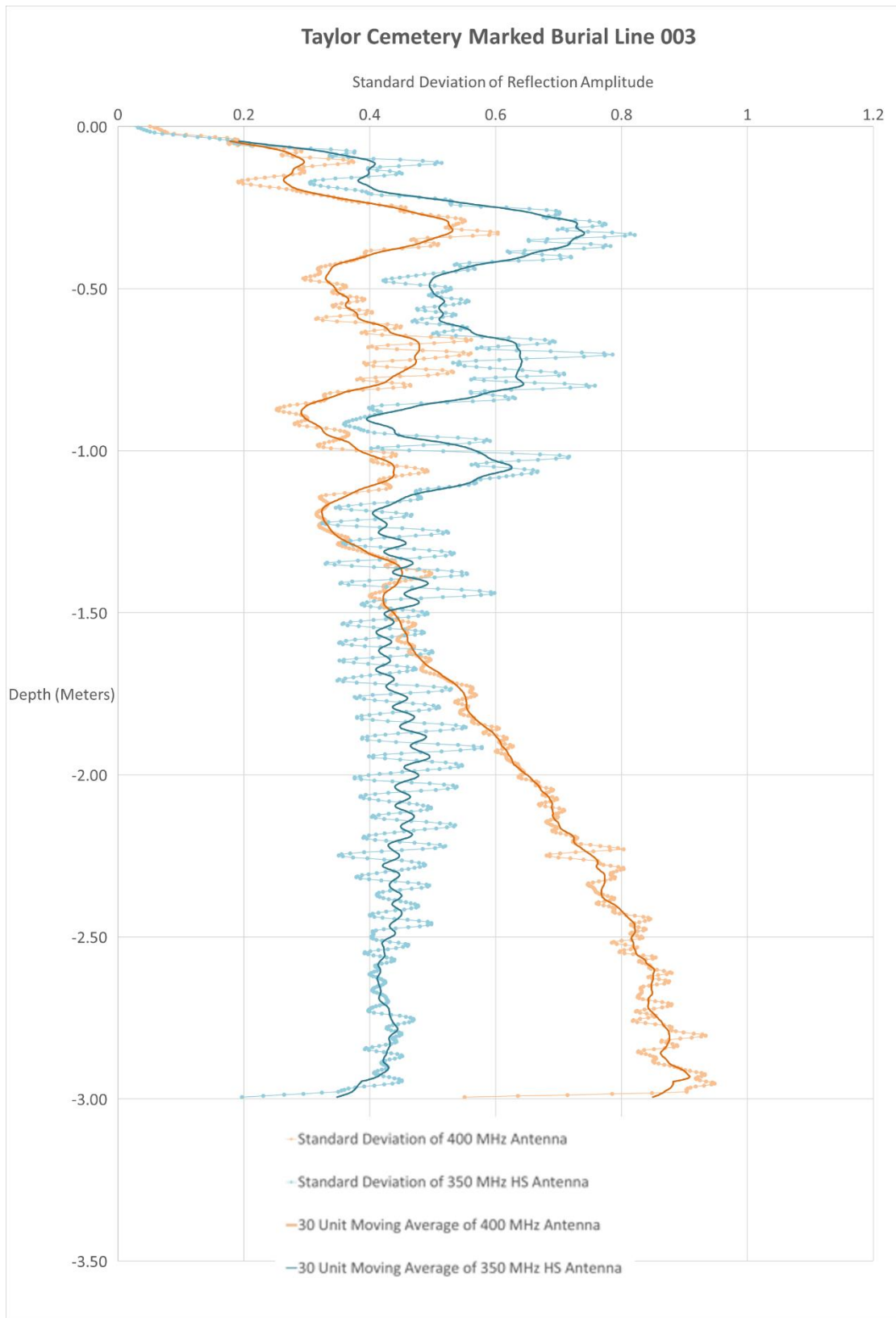


Figure 3.12. Graph of standard deviation with depth for Line 003 over a marked burial

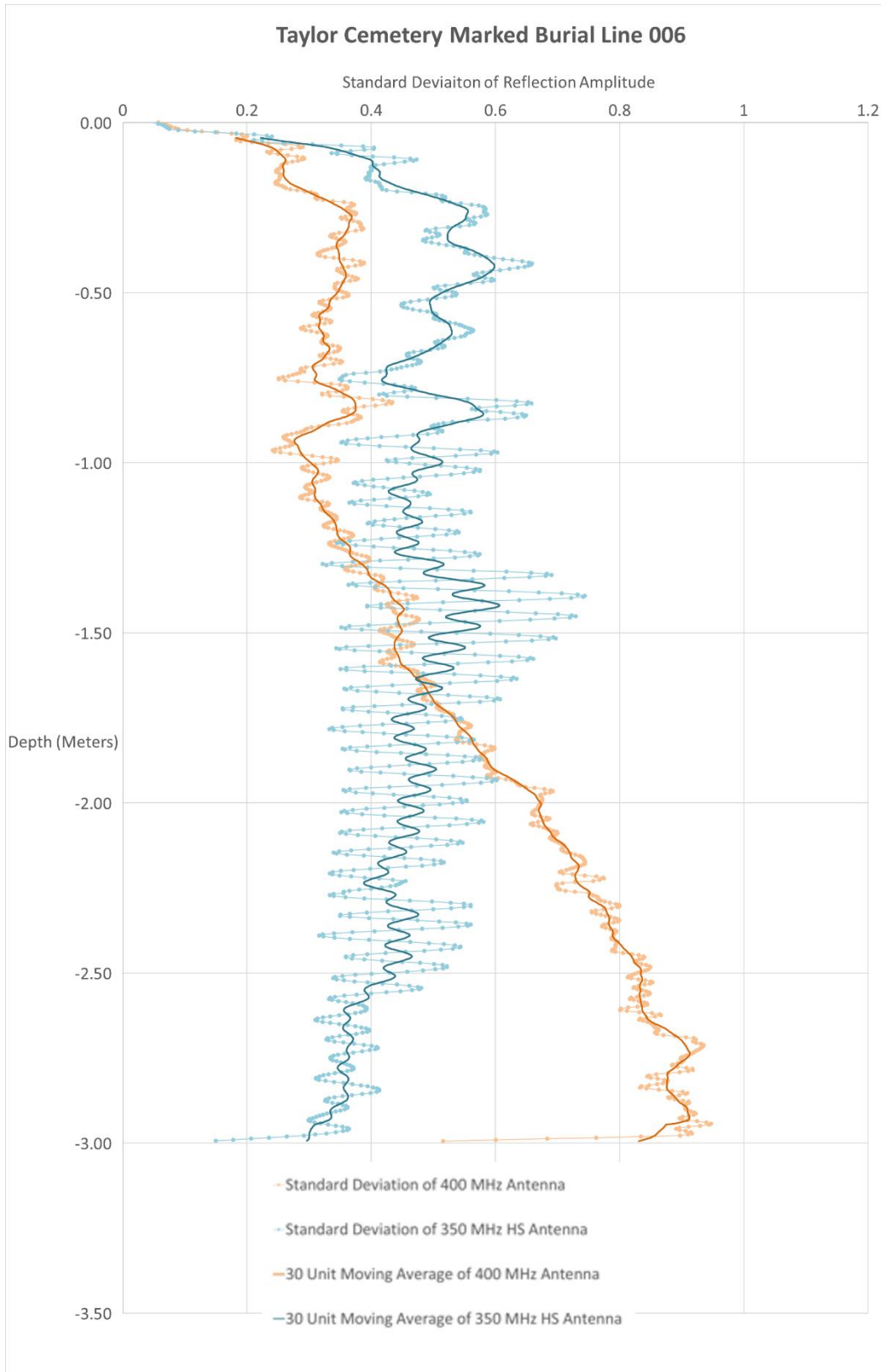


Figure 3.13. Graph of standard deviation with depth for Line 006 over a marked burial

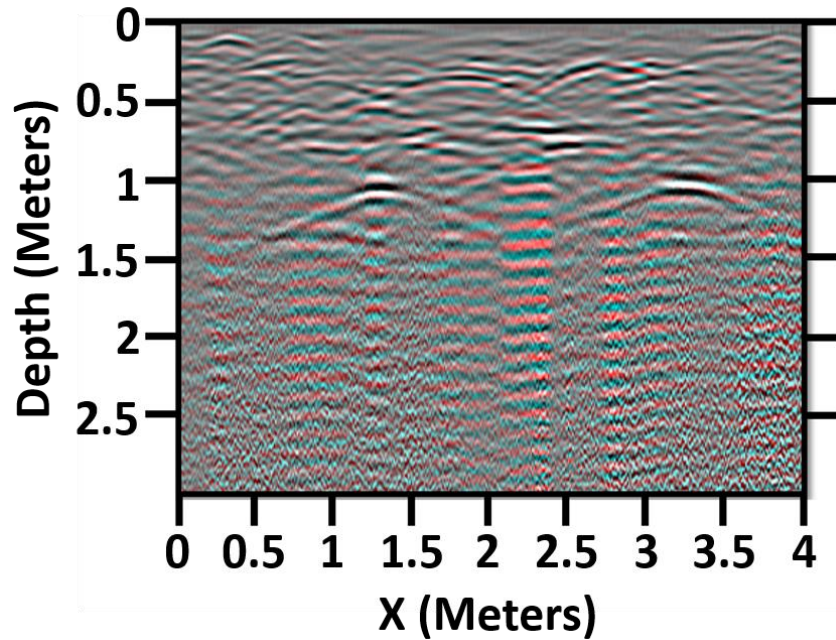


Figure 3.14. Color composite marked burials line 003, 400 MHz antenna is the blue and green band and 350 MHz HS antenna is the red band. Shades of gray indicate agreement between antennas.

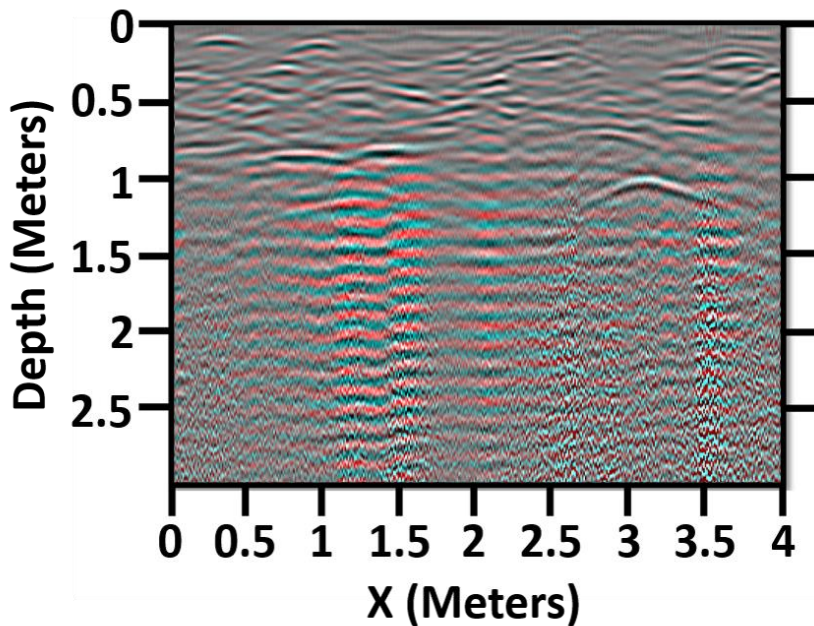


Figure 3.15. Color composite marked burials line 006, 400 MHz antenna is the blue and green band and 350 MHz HS antenna is the red band. Shades of gray indicate agreement between antennas.

Unmarked Burials. Estimated radar velocity was 0.066 meters per nanosecond and RDP was 20.66 for Taylor Cemetery. Two sample lines were collected over two depressions assumed to be potential unmarked burials. A single hyperbolic reflection was observed at a depth of approximately 1 meter (Figure 3.16), which was the expected response for a burial. The hyperbolic reflection was observed on a second radargram (Figure 3.17) at an approximate depth of 0.7 meters. However, this reflection response appeared weaker. In both radargrams the noise floor was interpreted at a depth of approximately 1.3 meters, due to the increase in random reflections (Figures 3.16 and 3.17). In both radargrams there was continuous horizontal banding observed in the radargrams for the 350 MHz HS antenna (Figures 3.16 and 3.17). The Hilbert transform radargrams of the unmarked burials showed linear spikes of noise (Figures 3.18 and 3.19). Generally, it appeared that there was more linear spiking noise with the 400 MHz than the 350 MHz HS antenna (Figure 3.19).

The graph of standard deviation of recorded radar reflection amplitude showed an increase in standard deviation at approximately 1 meter with the 350 MHz HS antenna but not the 400 MHz antenna (Figures 3.20 and 3.21). Visually, the graph showed that there is a transitional zone from approximately 1 to 1.5 meters in depth where there was an increase in noise. The point of intersection occurs at approximately 1.5 to 2 meters and delineates the point of complete signal loss, indicating that only noise, and no meaningful reflections were being recorded. The standard deviation curve agrees with the radargram data. Following the point of intersection, the lines separate where remaining noise in the 400 MHz antenna data was amplified in comparison to the 350 MHz HS antenna data. Agreement between the 400 MHz and 350 MHz HS antennas, at the location of the burials, was indicated by the shades of gray in the color composite (Figures 3.22 and 3.23). Generally, it appeared that the 400 MHz antenna

contributed more noise to the data, as indicated by the appearance of cyan, as random reflectors in the lower half of the radargrams. Noise shown in red, appeared only in the 350 MHz HS antenna data, such as the horizontal striping to the right of the burial at approximately 2.5 meters in horizontal distance (Figure 3.22).

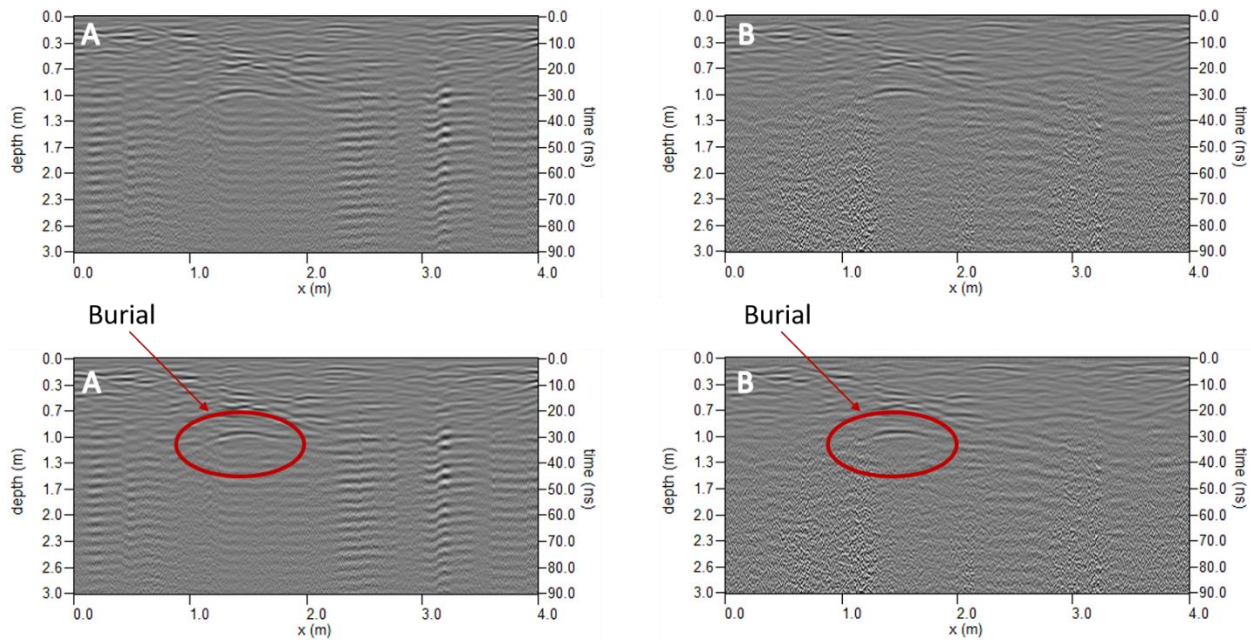


Figure 3.16. Radargrams line 003 possible unmarked burials at Taylor Cemetery (A) 350 MHz HS antenna (B) 400 MHz antenna

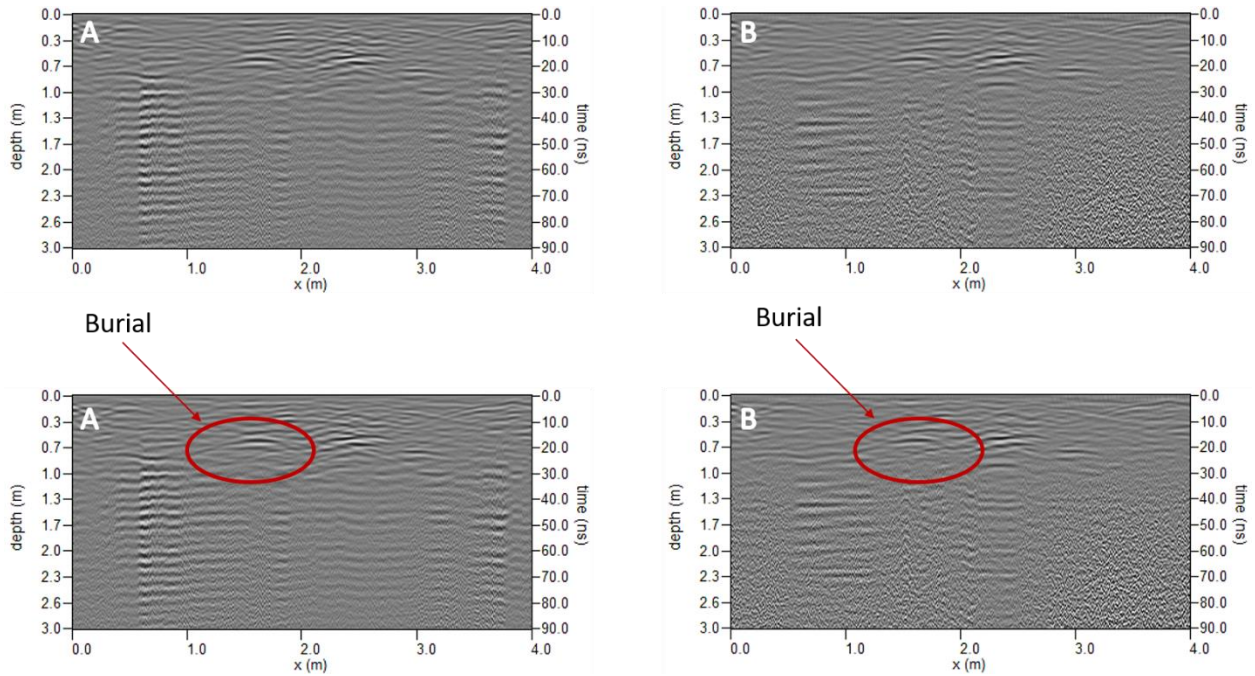


Figure 3.17. Radargrams line 004 possible unmarked burials at Taylor Cemetery (A) 350 MHz HS antenna (B) 400 MHz antenna

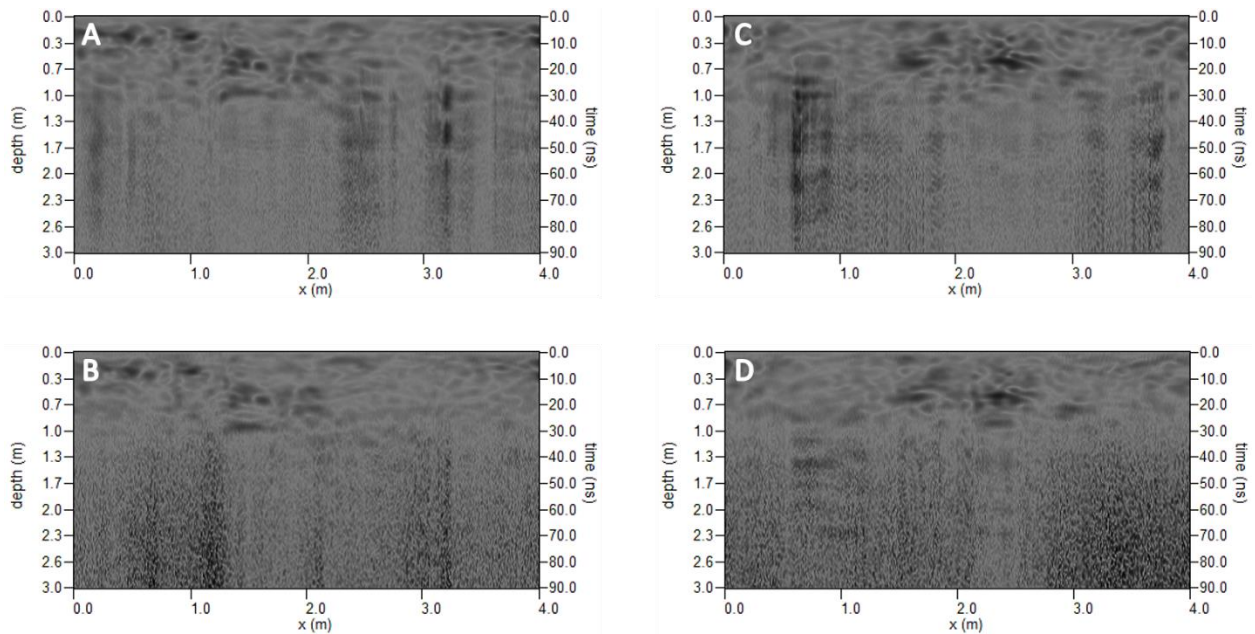


Figure 3.18. Hilbert transform radargrams of unmarked burials at Taylor Cemetery (A) 350 MHz HS antenna line 003 (B) 400 MHz antenna line 003 (C) 350 MHz HS antenna line 004 (D) 400 MHz antenna line 004

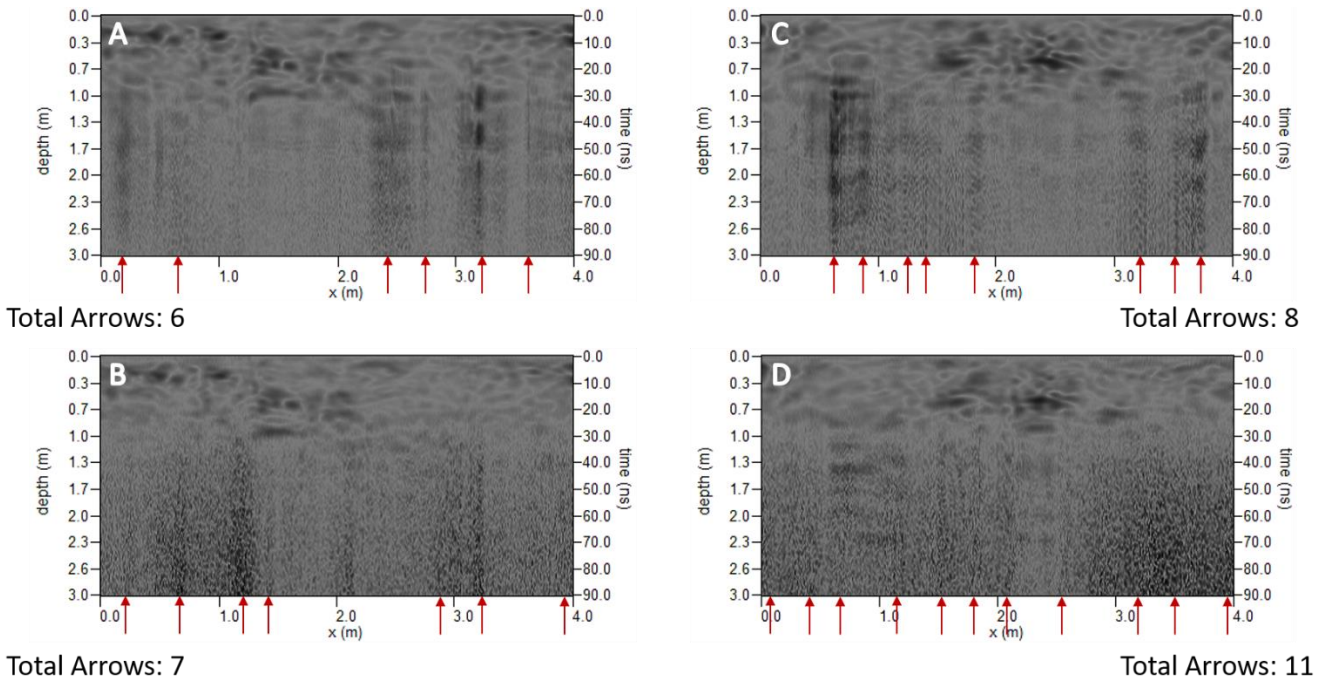


Figure 3.19. Hilbert transform radargrams of unmarked burials at Taylor Cemetery (A) 350 MHz HS antenna line 003 (B) 400 MHz antenna line 003 (C) 350 MHz HS antenna line 004 (D) 400 MHz line antenna 004. Red arrows indicate areas of noise.

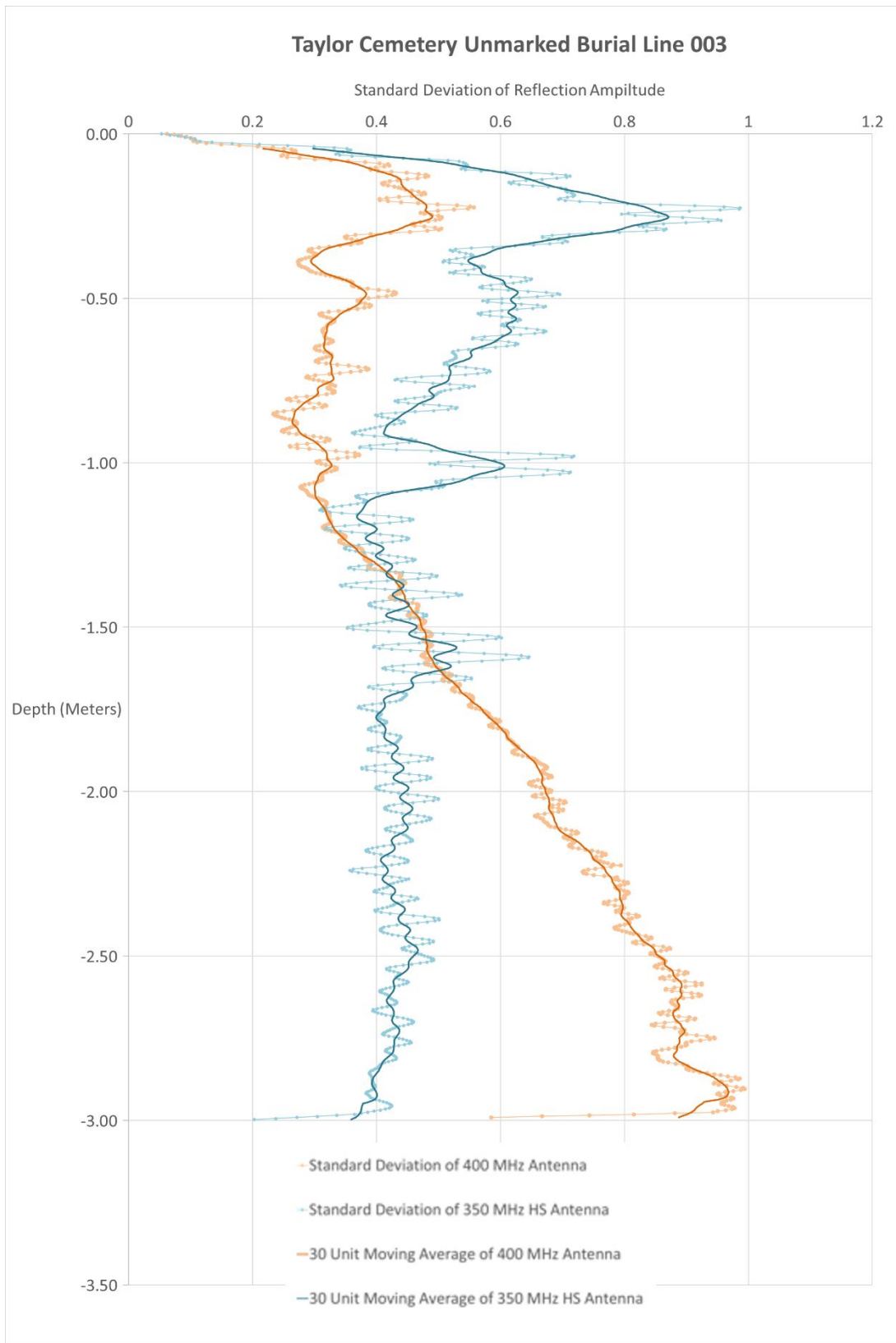


Figure 3.20. Graph of standard deviation with depth for line 003 over an unmarked burial

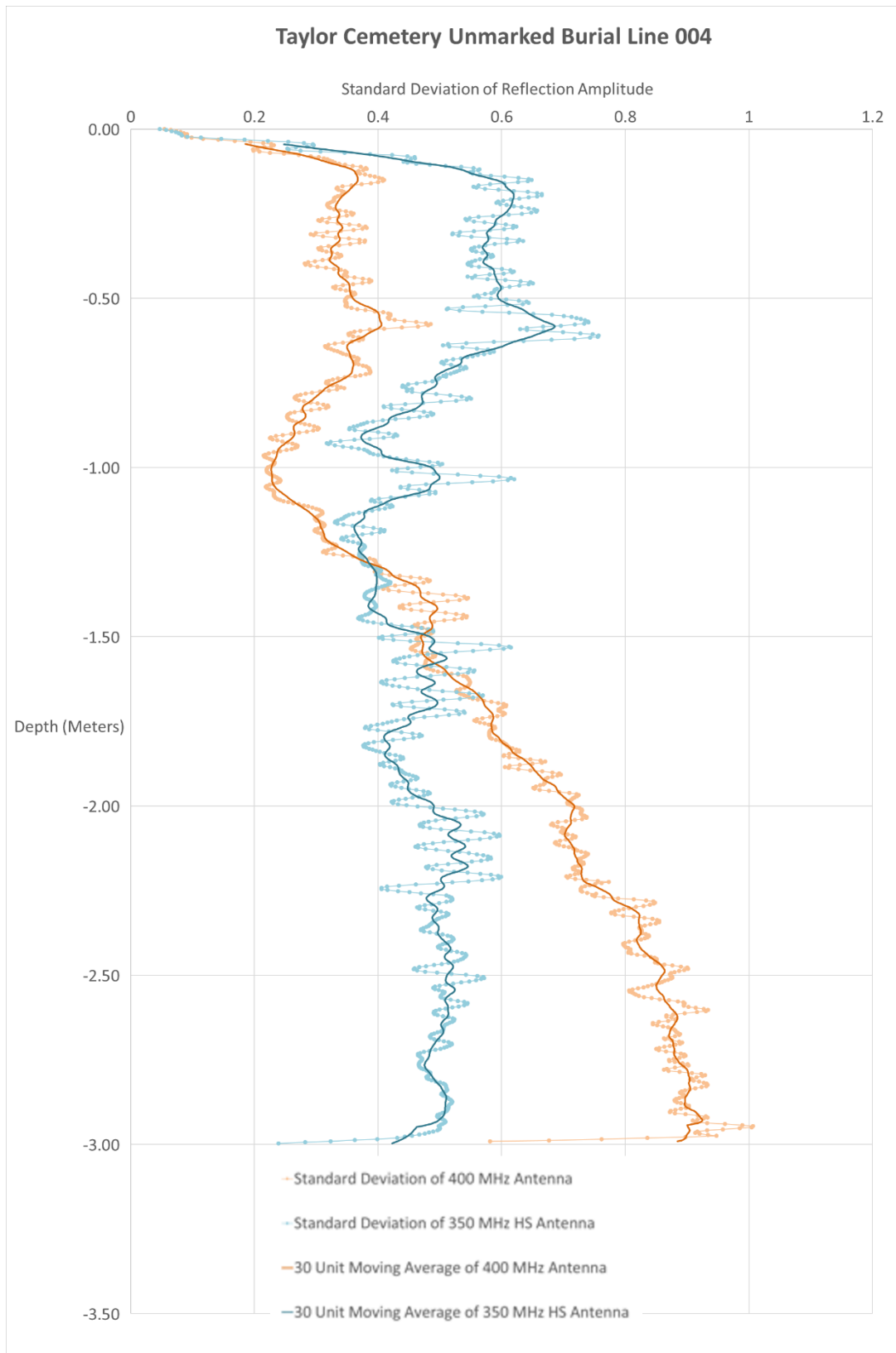


Figure 3.21. Graph of standard deviation with depth for line 004 over an unmarked burial

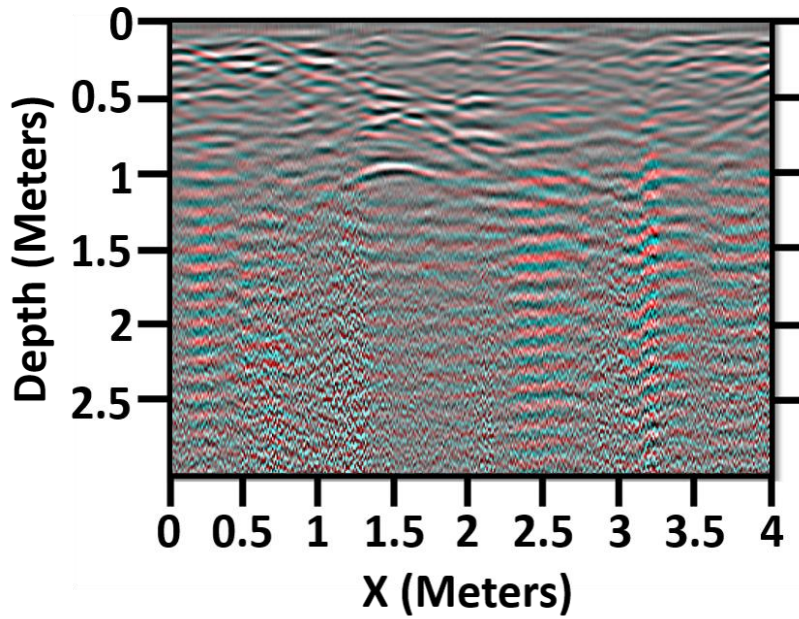


Figure 3.22. Color composite of unmarked burials line 003, 400 MHz antenna is the blue and green band and 350 MHz HS antenna is the red band. Shades of gray indicate agreement between antennas.

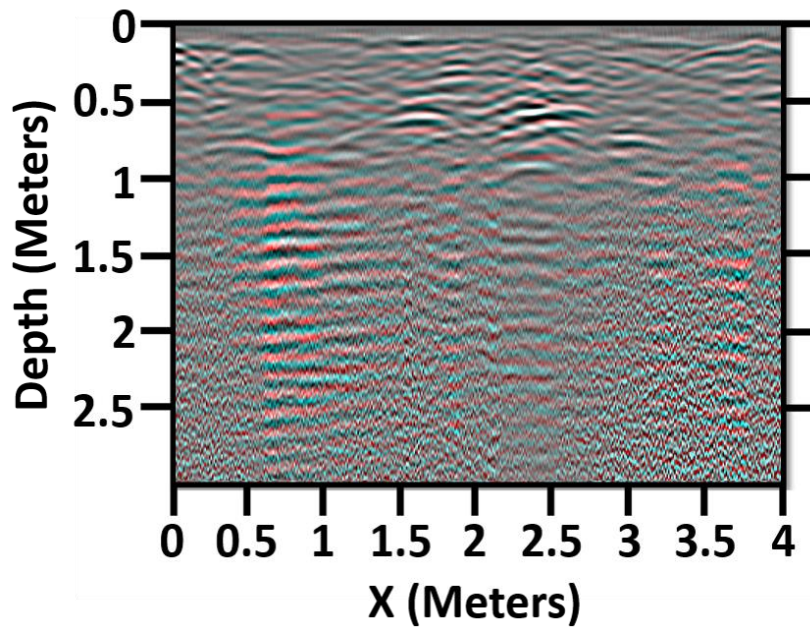


Figure 3.23. Color composite of unmarked burials line 004, 400 MHz antenna is the blue and green band and 350 MHz HS antenna is the red band. Shades of gray indicate agreement between antennas.

Quantitative Analysis

Marked Burials. There were statistically significant differences occurring at depth between the 400 MHz and 350 MHz HS antennas for both the sample transects. Statistical results for Taylor Cemetery line 003 indicated that there was a significant difference ($p = 0.000$) in the standard deviations of reflection amplitude between the 400 MHz and 350 MHz HS antennas from a depth of 0.0 to 1.4 meters (Table 3.3). There was an insignificant difference in the standard deviations for line 003 between the 400 MHz and 350 MHz HS antennas at a depth of 1.4 to 1.6 meters. There was a statistically significant difference ($p = 0.000$) in standard deviations between the 400 MHz and 350 MHz HS antennas from a depth of 1.6 to 3.0 meters. Statistical results for Taylor Cemetery line 006 indicate that there was a significant difference in the standard deviations of reflection amplitude between the 400 MHz and 350 MHz HS antennas at all depths of the profile (0.0 to 3.0 meters) (Table 3.4).

Table 3.3. P-values from the Mann-Whitney U Test at depth interval of 0.2 meters indicating significant differences between the two antenna frequencies

Taylor Cemetery Marked Burial Line 003	
Mann-Whitney U Test Results	
Depth (Meters)	P-Value
0.0 to 0.2	0.000
0.2 to 0.4	0.000
0.4 to 0.6	0.000
0.6 to 0.8	0.000
0.8 to 1.0	0.000
1.0 to 1.2	0.000
1.2 to 1.4	0.000
1.4 to 1.6	-
1.6 to 1.8	0.000
1.8 to 2.0	0.000
2.0 to 2.2	0.000
2.2 to 2.4	0.000
2.4 to 2.6	0.000
2.6 to 2.8	0.000
2.8 to 3.0	0.000
<i>Significant at 0.05 Confidence Level</i>	

Table 3.4. P-values from the Mann-Whitney U Test at depth interval of 0.2 meters indicating significant differences between the two antenna frequencies

Taylor Cemetery Marked Burial Line 006	
Mann-Whitney U Test Results	
Depth (Meters)	P-Value
0.0 to 0.2	0.000
0.2 to 0.4	0.000
0.4 to 0.6	0.000
0.6 to 0.8	0.000
0.8 to 1.0	0.000
1.0 to 1.2	0.000
1.2 to 1.4	0.000
1.4 to 1.6	0.000
1.6 to 1.8	0.008
1.8 to 2.0	0.000
2.0 to 2.2	0.000
2.2 to 2.4	0.000
2.4 to 2.6	0.000
2.6 to 2.8	0.000
2.8 to 3.0	0.000
<i>Significant at 0.05 Confidence Level</i>	

Unmarked Burials. There were statistically significant differences occurring at depth between the 400 MHz and 350 MHz HS antennas for both the sample transects. Statistical results for Taylor Cemetery line 003 indicated that there was a significant difference in the standard deviations of reflection amplitude between the 400 MHz and 350 MHz HS antennas from a depth of 0.0 to 1.4 meters and 1.6 to 3.0 meters (Table 3.5). Statistical results for Taylor Cemetery line 004 indicated that there was a significant difference in the standard deviations of reflection amplitude between the 400 MHz and 350 MHz HS antennas at all depths of the profile (0.0 to 3.0 meters) (Table 3.6). There is a less significant difference ($p = 0.025$) at a depth of 1.2 to 1.4 meters between both the 400 MHz and 350 MHz HS antennas.

Table 3.5. P-values from the Mann-Whitney U Test at depth interval of 0.2 meters indicating significant differences between the two antenna frequencies

Taylor Cemetery Unmarked Burial Line 003	
Mann-Whitney U Test Results	
Depth (Meters)	P-Value
0.0 to 0.2	0.000
0.2 to 0.4	0.000
0.4 to 0.6	0.000
0.6 to 0.8	0.000
0.8 to 1.0	0.000
1.0 to 1.2	0.000
1.2 to 1.4	0.010
1.4 to 1.6	-
1.6 to 1.8	0.000
1.8 to 2.0	0.000
2.0 to 2.2	0.000
2.2 to 2.4	0.000
2.4 to 2.6	0.000
2.6 to 2.8	0.000
2.8 to 3.0	0.000
<i>Significant at 0.05 Confidence Level</i>	

Table 3.6. P-values from the Mann-Whitney U Test at depth interval of 0.2 meters indicating significant differences between the two antenna frequencies

Taylor Cemetery Unmarked Burial Line 004	
Mann-Whitney U Test Results	
Depth (Meters)	P-Value
0.0 to 0.2	0.000
0.2 to 0.4	0.000
0.4 to 0.6	0.000
0.6 to 0.8	0.000
0.8 to 1.0	0.000
1.0 to 1.2	0.000
1.2 to 1.4	0.025
1.4 to 1.6	0.006
1.6 to 1.8	0.000
1.8 to 2.0	0.000
2.0 to 2.2	0.000
2.2 to 2.4	0.000
2.4 to 2.6	0.000
2.6 to 2.8	0.000
2.8 to 3.0	0.000
<i>Significant at 0.05 Confidence Level</i>	

Carter Mansion

Qualitative Analysis

Estimated radar velocity was 0.09 meters per nanosecond and RDP was 11.05 for Carter Mansion. There was a strong hyperbolic reflection occurring at an approximate depth of 1.4 meters between 2 to 4 meters along the radargrams for the Carter Mansion line 015 (Figure 3.24). Above the hyperbolic reflection there was a strong horizontal reflection at an approximate depth of 0.9 meters. Depth of penetration appeared to increase marginally at approximately 0.1 meters along the radargram with the 350 MHz HS antenna as compared to the 400 MHz antenna, which was indicated by reflections seen at an approximate depth of 2.7 meters (Figure 3.25). The Hilbert transform radargrams confirm the hyperbolic reflection between 2 to 4 meters along the radargrams (Figure 3.26). More linear noise spiking occurred within the 400 MHz antenna data, beginning at an approximate depth of 2.7 meters (Figures 3.26 and 3.27). Generally, the noise reduction of the 350 MHz HS antenna was confirmed by the Hilbert transform radargrams (Figures 3.26 and 3.27).

Multiple strong hyperbolic reflections occurred at a depth between approximately 0.9 to 1.4 meters and 10 to 14 meters along the radargrams for Carter Mansion line 024 (Figure 3.28). There was a relatively continuous strong horizontal reflection at an approximate depth of 1.4 meters from 14 to 20 meters along the radargrams. There was a marginal increase of approximately 0.1 meters in depth of penetration and noise reduction with the 350 MHz HS antenna as compared to the 400 MHz antenna, which was indicated by the reflections seen at an approximate depth of 2.7 meters (Figure 3.29). The Hilbert transform radargrams confirm the hyperbolic reflections occurring between 14 to 20 meters along the radargrams (Figure 3.30). More linear noise spikes occurred with the 400 MHz antenna data, beginning at an approximate

depth of 2.7 meters (Figures 3.30 and 3.31). Generally, the noise reduction of the 350 MHz HS antenna was confirmed by the Hilbert transform radargrams (Figures 3.30 and 3.31).

The interpreted noise floor for both transects occurred at a depth of approximately 2.7 meters (Figures 3.24, 3.26, 3.28, and 3.30). Generally, the noise reduction of the 350 MHz HS antenna was confirmed by the Hilbert transform radargrams (Figures 3.26, 3.27, 3.30, and 3.31). The graphs of standard deviation of reflection amplitude showed higher values of standard deviation in the near-surface with the 350 MHz HS antenna as compared to the 400 MHz antenna (Figures 3.32 and 3.33). There was a transitional zone of reduced signal strength indicated by the decreasing values of standard deviations between 2 to 2.5 meters depth. The intersection of the lines was interpreted to be the depth of complete signal loss. There was a strong increase in standard deviation with the 400 MHz antenna data at approximately 2.5 to 4.1 meters, which indicated amplified noise. The color composite showed strong agreement of location of the interpreted features as indicated by the white (Figures 3.34 and 3.35). Other areas of agreement in the color composites are shown by the shades of gray. Importantly, there was more cyan occurring in the lower half of the radargrams, which indicated that the 400 MHz antenna amplified more noise beneath the noise floor.

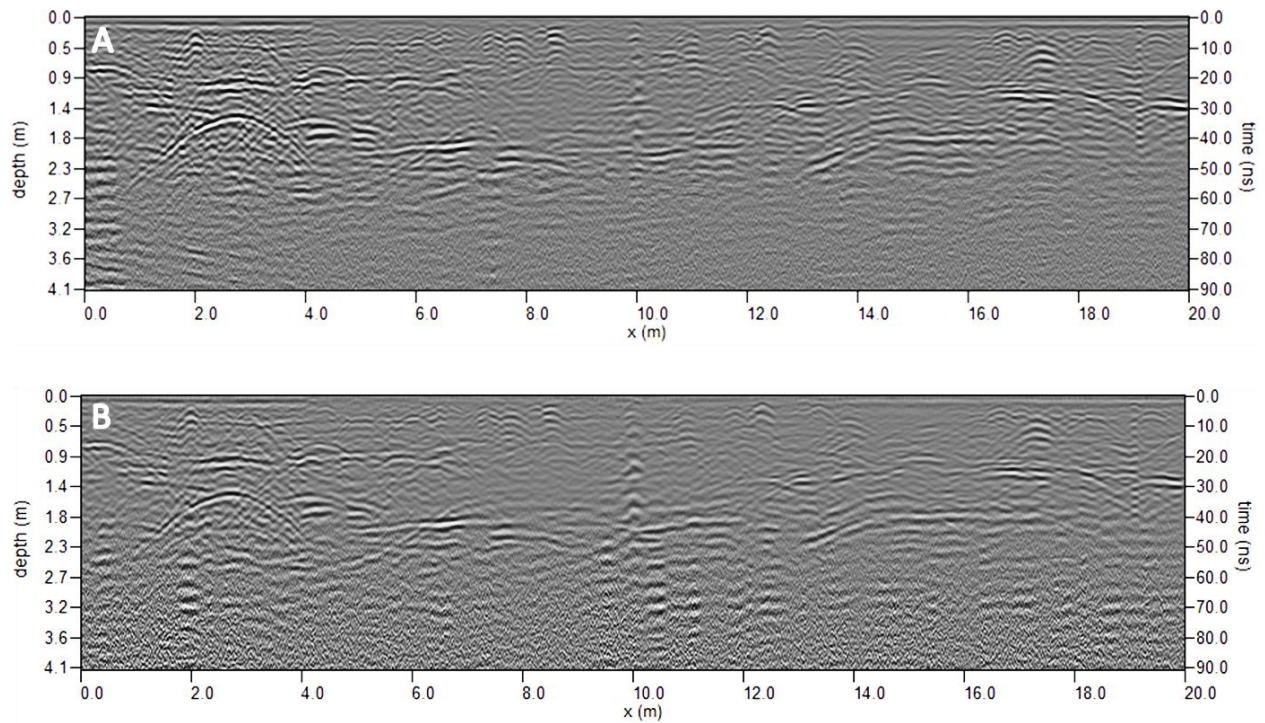


Figure 3.24. Radargrams for Carter Mansion line 015 (A) 350 MHz HS antenna (B) 400 MHz antenna

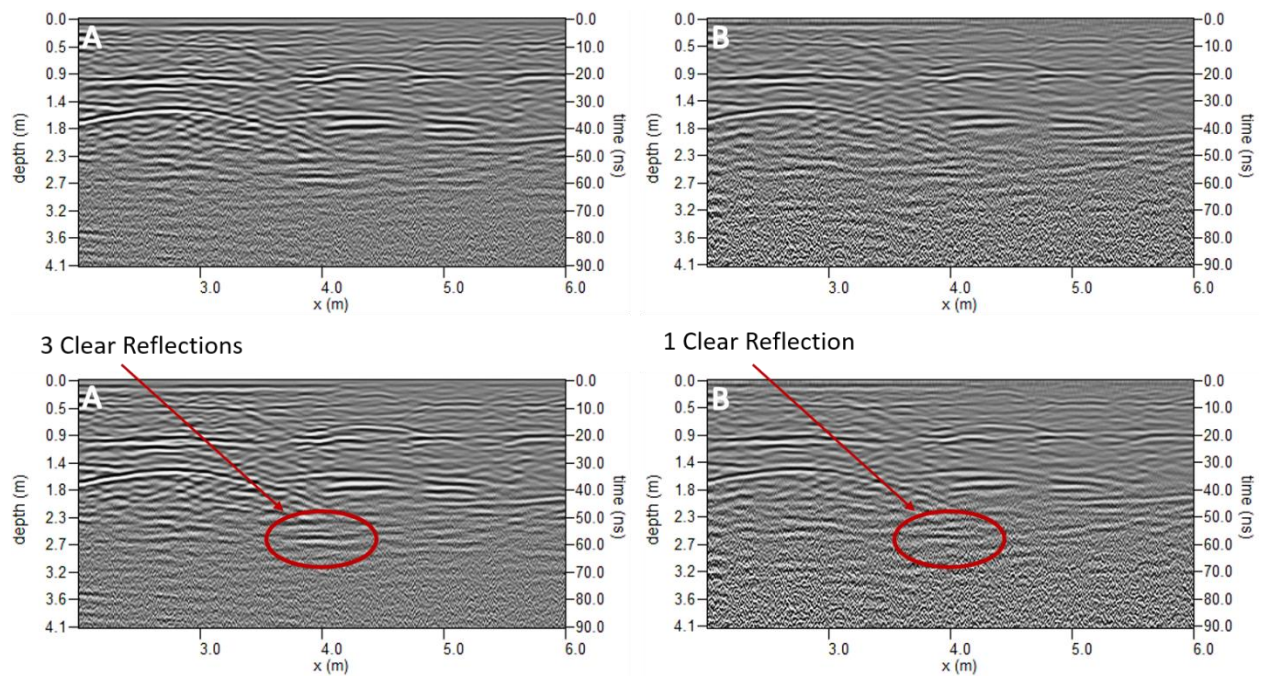


Figure 3.25. Zoomed in view of radargrams for Carter Mansion line 015 (A) 350 MHz HS antenna (B) 400 MHz antenna, showing the marginal increase in depth of penetration

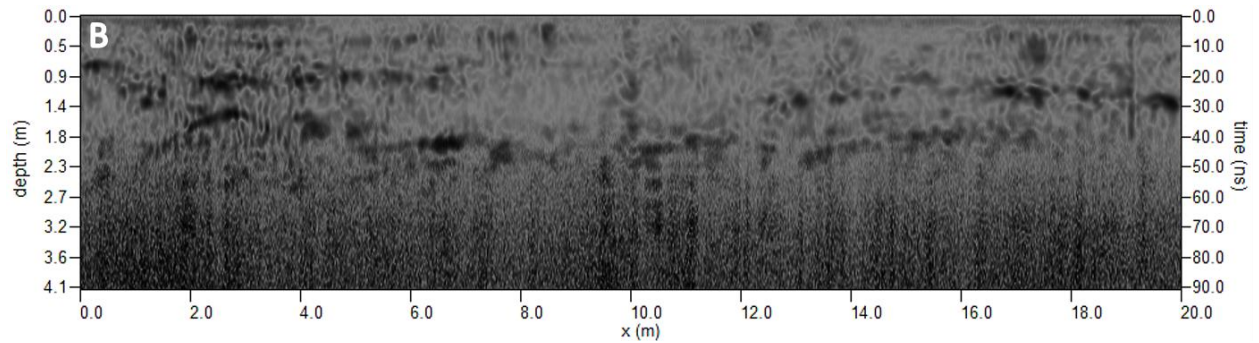
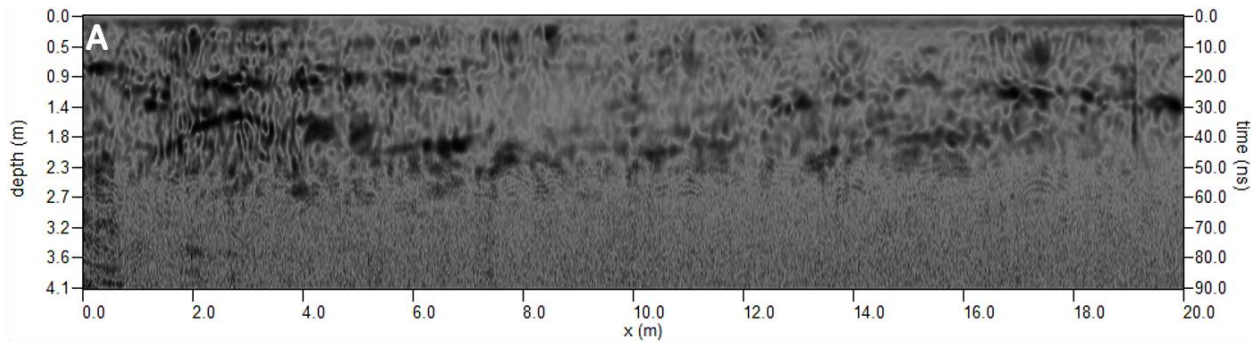
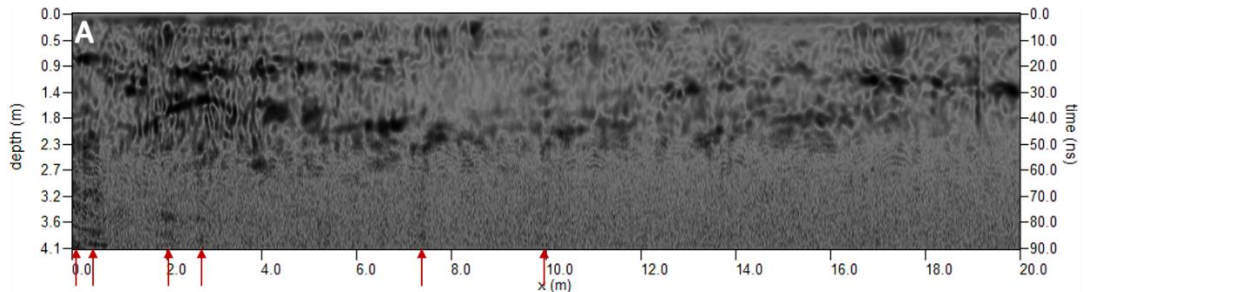
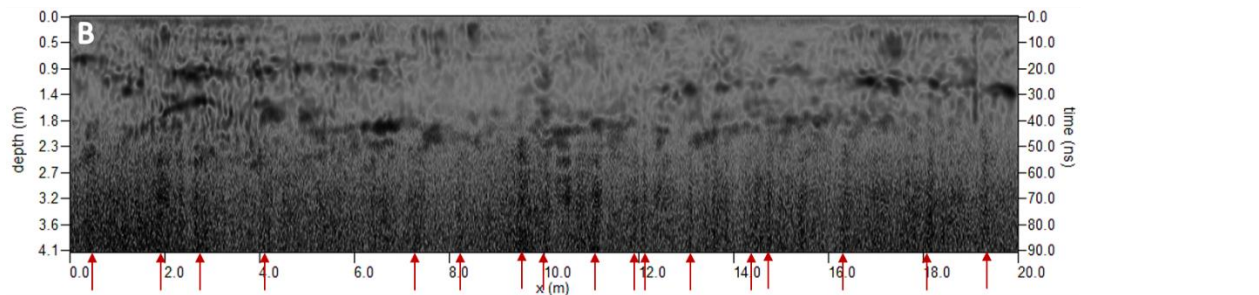


Figure 3.26. Hilbert transform radargrams for Carter Mansion line 015 (A) 350 MHz HS antenna (B) 400 MHz antenna, showing the hyperstacking noise



Total Arrows: 6



Total Arrows: 17

Figure 3.27. Hilbert transform radargrams for Carter Mansion line 015 (A) 350 MHz HS antenna (B) 400 MHz antenna showing the hyperstacking noise reduction. Red arrows indicate areas of noise.

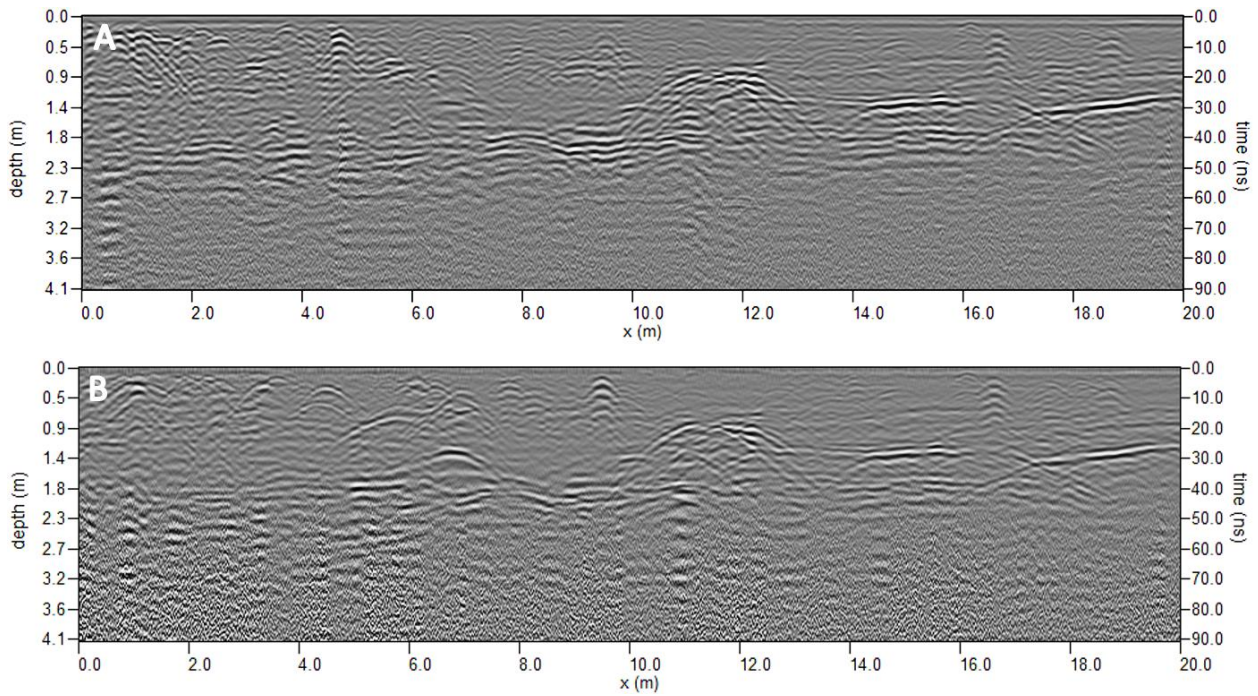


Figure 3.28. Radargrams for Carter Mansion line 024 (A) 350 MHz HS antenna (B) 400 MHz antenna

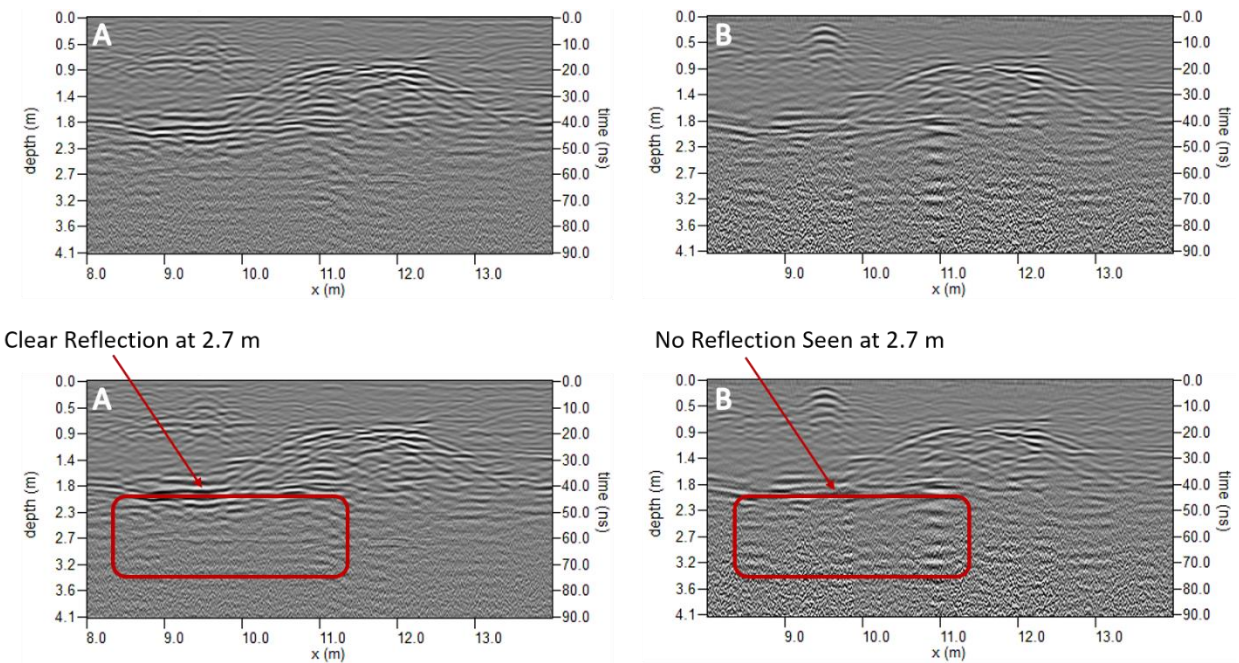


Figure 3.29. Zoomed in view of radargrams for Carter Mansion line 024 (A) 350 MHz HS antenna (B) 400 MHz antenna, showing the marginal increase in depth of penetration

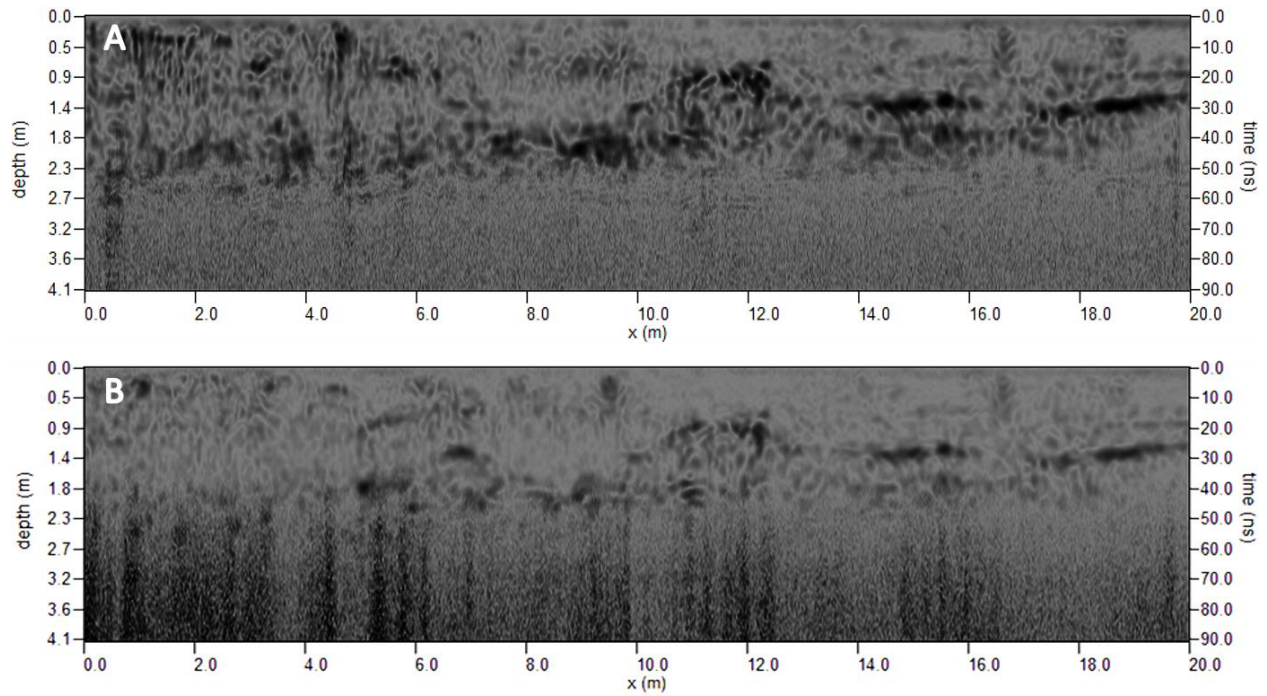


Figure 3.30. Hilbert transform radargrams for Carter Mansion line 024 (A) 350 MHz HS antenna (B) 400 MHz antenna showing the hyperstacking noise reduction

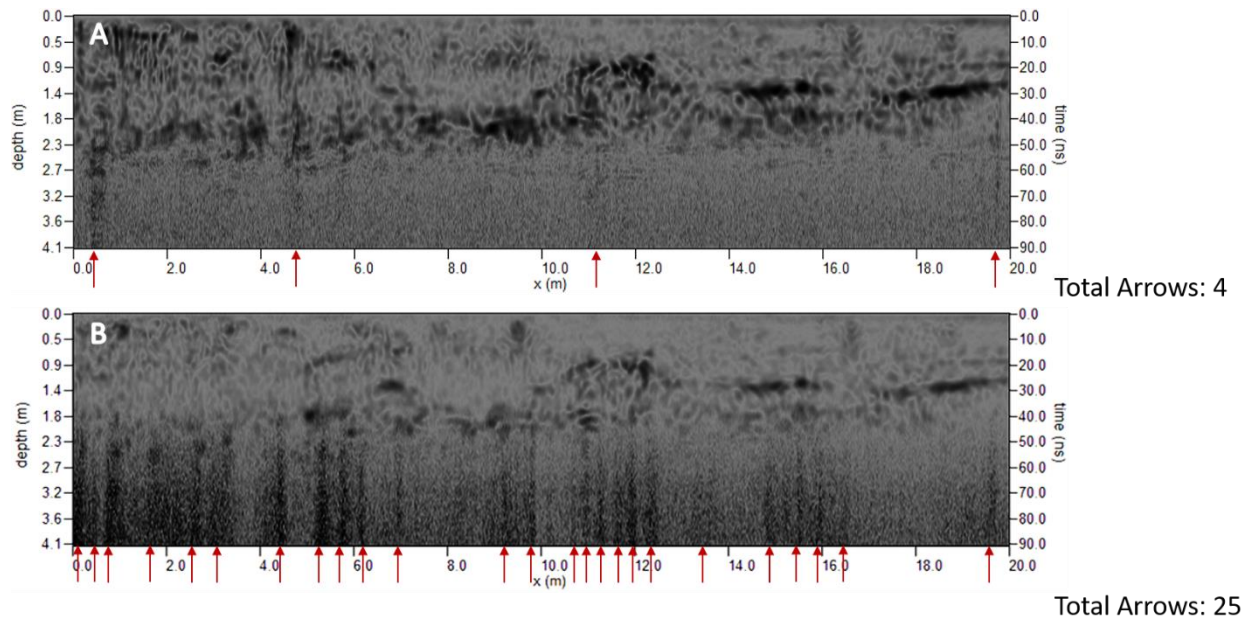


Figure 3.31. Hilbert transform radargrams for Carter Mansion line 024 (A) 350 MHz HS antenna (B) 400 MHz antenna showing the hyperstacking noise reduction. Red arrows indicate areas of noise.

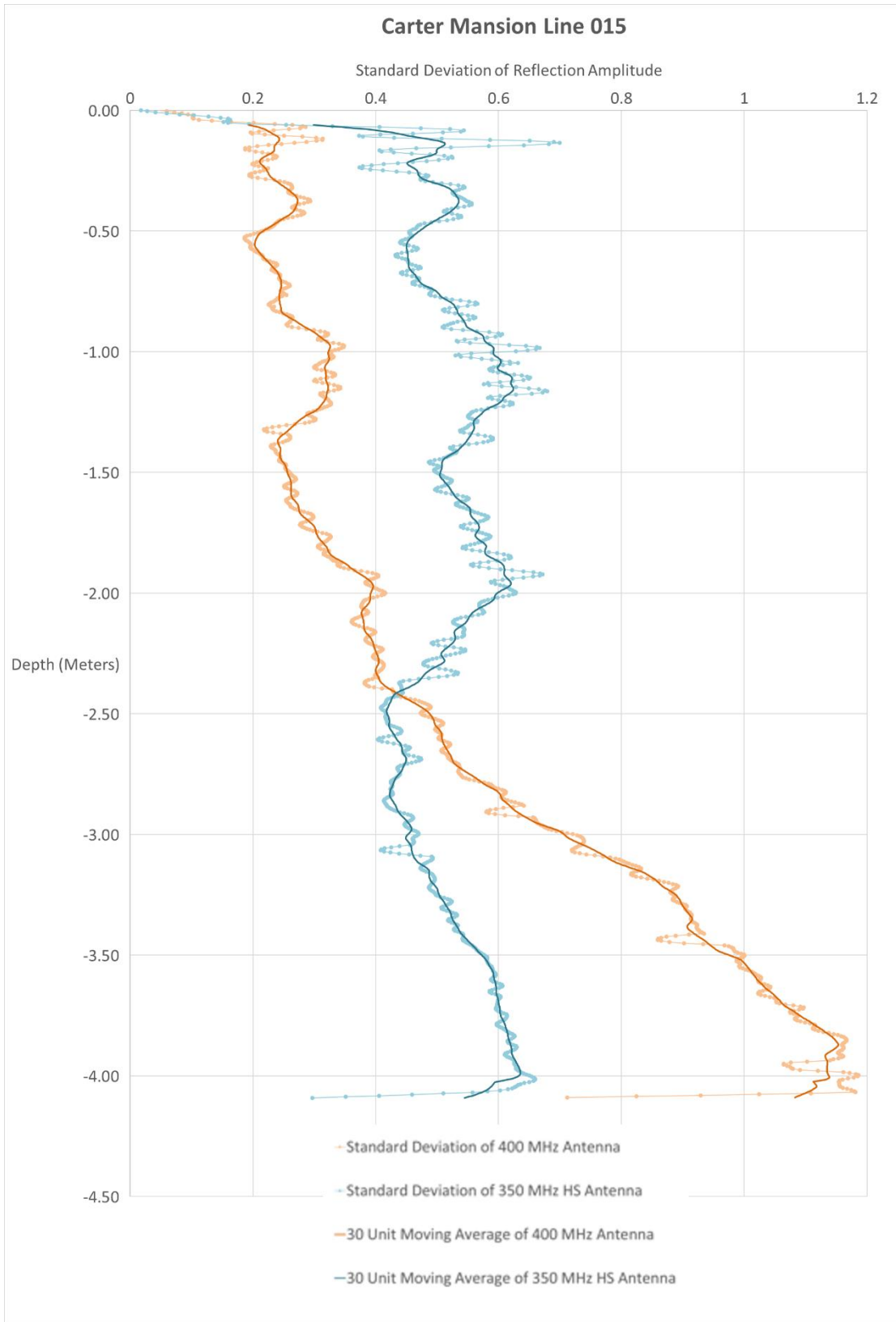


Figure 3.32. Graph of standard deviation with depth for Carter Mansion Line 015

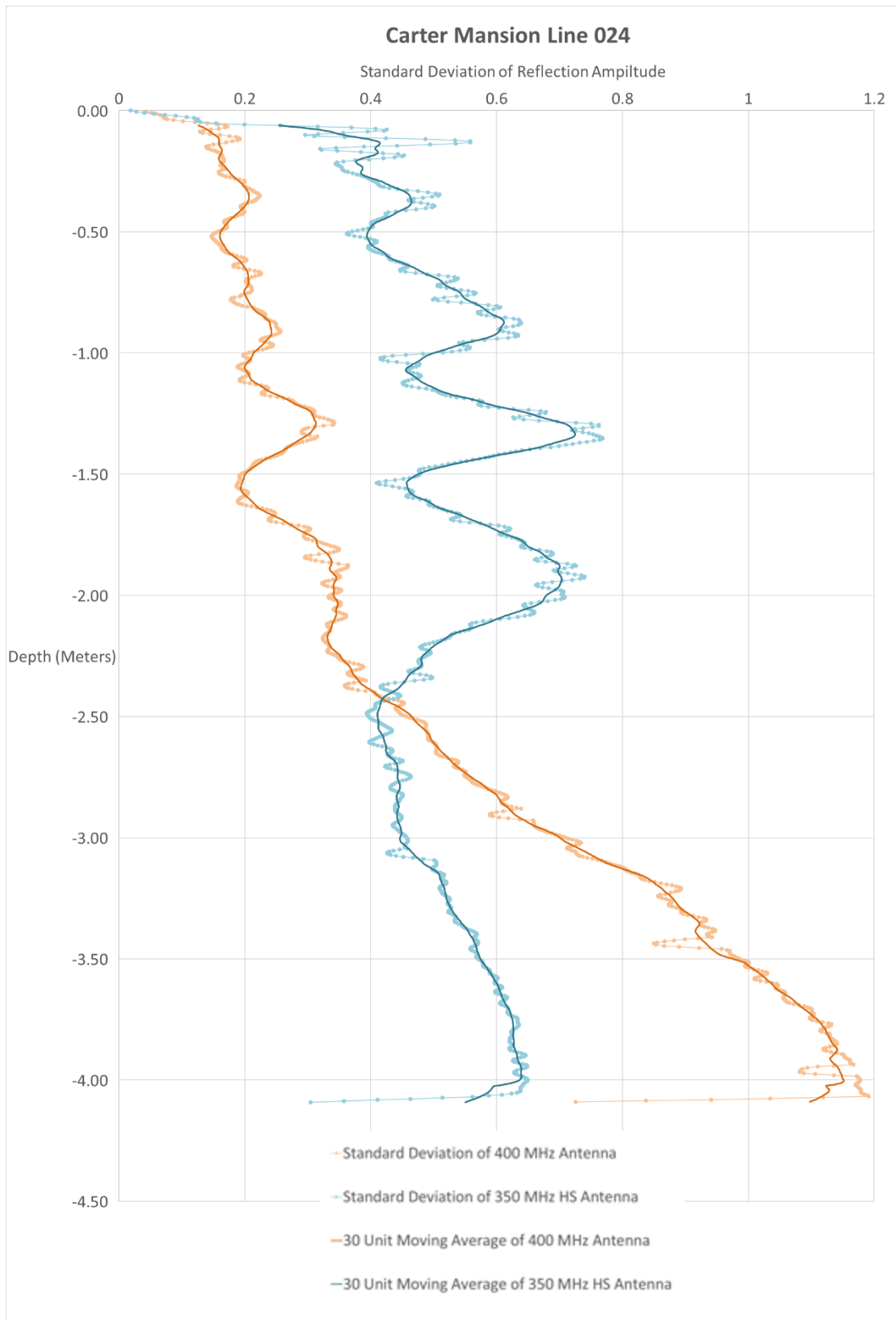


Figure 3.33. Graph of standard deviation with depth for Carter Mansion Line 024

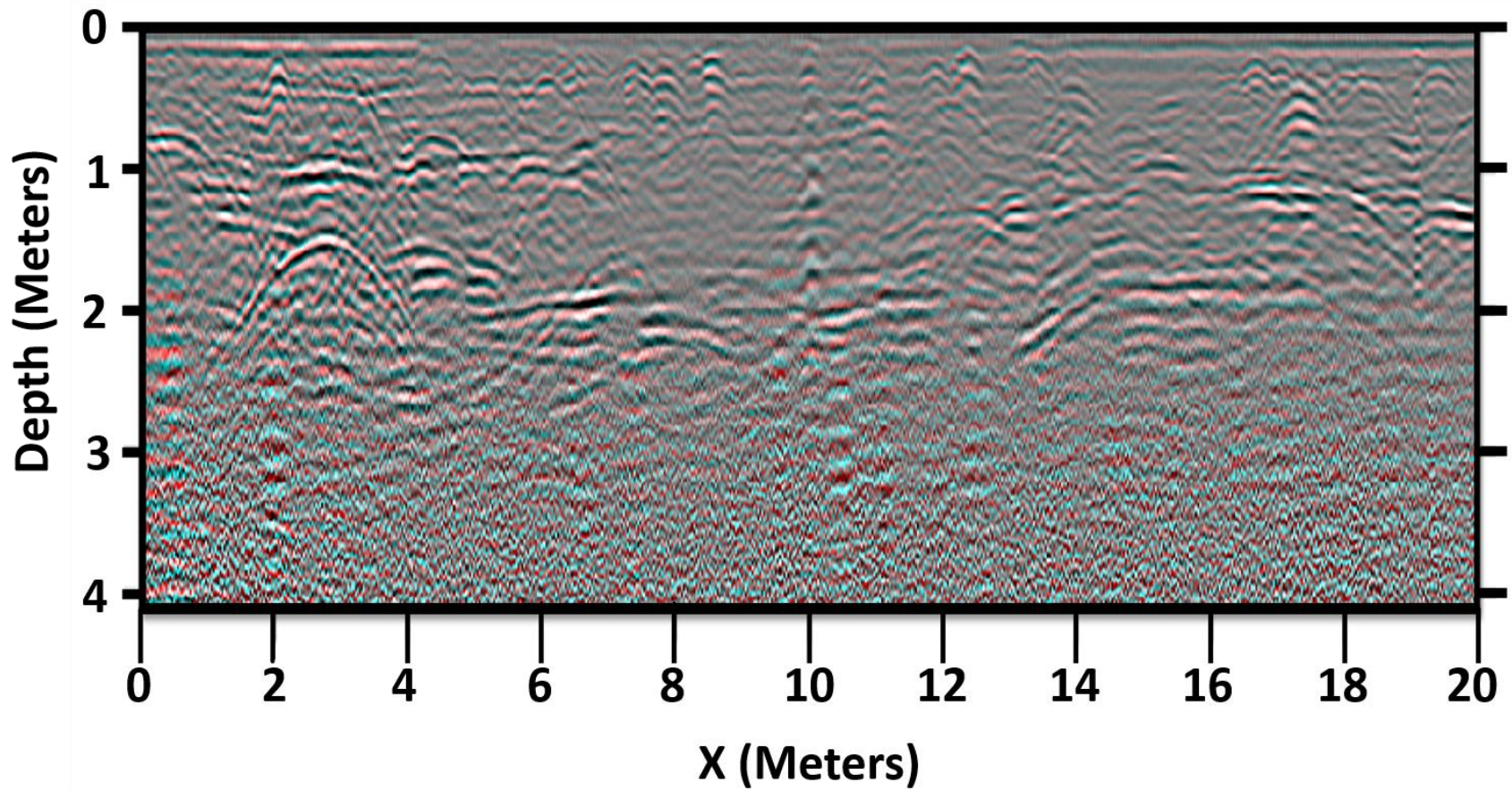


Figure 3.34. Color composite of Carter Mansion line 015, 400 MHz antenna is the blue and green band and 350 MHz HS antenna is the red band. Shades of gray indicate agreement between the 400 MHz and the 350 MHz HS antennas.

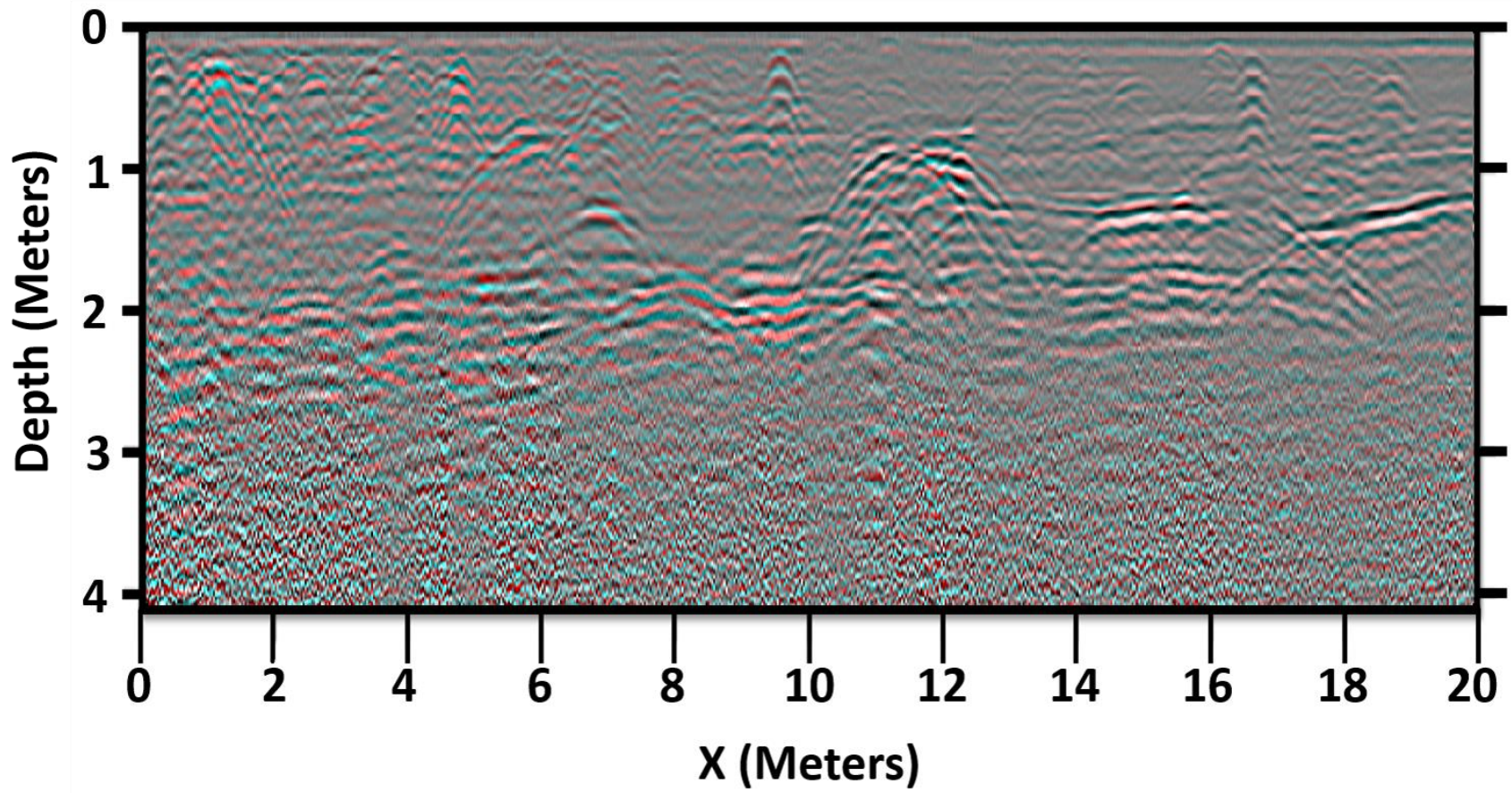


Figure 3.35. Color composite of Carter Mansion line 024, 400 MHz antenna is the blue and green band and 350 MHz HS antenna is the red band. Shades of gray indicate agreement between the 400 MHz and the 350 MHz HS antennas.

Quantitative Analysis

There were statistically significant differences occurring at depth between the 400 MHz and 350 MHz HS antennas for both the sample transects. Results for Carter Mansion line 015 indicate that there was a significant difference ($p = 0.000$) in the standard deviations of reflection amplitude between both the 400 MHz and 350 MHz HS antennas at all depths from 0.0 to 4.0 meters (Table 3.7). Results for Carter Mansion line 024 indicate that there was a significant difference ($p = 0.000$) in the standard deviations of reflection amplitude between both the 400 MHz and 350 MHz HS antennas at all depths from 0.0 to 4.0 meters (Table 3.8).

Table 3.7. P-values from the Mann-Whitney U Test at depth interval of 0.2 meters indicating significant differences between the two antenna frequencies at all depths

Carter Mansion Line 015	
Mann-Whitney U Test Results	
Depth (Meters)	P-Value
0.0 to 0.2	0.000
0.2 to 0.4	0.000
0.4 to 0.6	0.000
0.6 to 0.8	0.000
0.8 to 1.0	0.000
1.0 to 1.2	0.000
1.2 to 1.4	0.000
1.4 to 1.6	0.000
1.6 to 1.8	0.000
1.8 to 2.0	0.000
2.0 to 2.2	0.000
2.2 to 2.4	0.000
2.4 to 2.6	0.000
2.6 to 2.8	0.000
2.8 to 3.0	0.000
3.0 to 3.2	0.000
3.2 to 3.4	0.000
3.4 to 3.6	0.000
3.6 to 3.8	0.000
3.8 to 4.0	0.000
<i>Significant at 0.05 Confidence Level</i>	

Table 3.8. P-values from the Mann-Whitney U Test at depth interval of 0.2 meters indicating significant differences between the two antenna frequencies at all depths

Carter Mansion Line 024	
Mann-Whitney U Test Results	
Depth (Meters)	P-Value
0.0 to 0.2	0.000
0.2 to 0.4	0.000
0.4 to 0.6	0.000
0.6 to 0.8	0.000
0.8 to 1.0	0.000
1.0 to 1.2	0.000
1.2 to 1.4	0.000
1.4 to 1.6	0.000
1.6 to 1.8	0.000
1.8 to 2.0	0.000
2.0 to 2.2	0.000
2.2 to 2.4	0.000
2.4 to 2.6	0.000
2.6 to 2.8	0.000
2.8 to 3.0	0.000
3.0 to 3.2	0.000
3.2 to 3.4	0.000
3.4 to 3.6	0.000
3.6 to 3.8	0.000
3.8 to 4.0	0.000
<i>Significant at 0.05 Confidence Level</i>	

Runion

Qualitative Analysis

Estimated radar velocity was 0.103 meters per nanosecond and RDP was 8.48 for Runion. There was a relatively continuous strong horizontal reflection at approximately 1.5 meters depth on Runion line 002 (Figure 3.36). There was a strong horizontal reflection from 4 to 16 meters at an approximate depth of 3.1 meters. Both relatively horizontal reflections are observed in the Hilbert transform radargram (Figure 3.37). There was a reduction in linear noise spiking with the 350 MHz HS antenna compared to the 400 MHz antenna, as indicated by the red arrows (Figure 3.38). Comparison between the radargrams and the Hilbert transform radargrams indicate the presence of four recognizable layers based on recognition of four distinct, relatively horizontal, reflections (Figures 3.36, 3.37, and 3.38). The layers appear as black areas on the Hilbert transform radargram (Figure 3.37).

In Runion line 014 there was a relatively continuous strong horizontal reflection present at an approximate depth of 1.5 meters (Figure 3.39). A strong dipping reflector occurs from 0 to 12 meters along the radargram, starting at an approximate depth of 4.1 meters and ending at a depth of 2.1 meters. The strong reflections also occurred on the Hilbert transform radargrams (Figure 3.40). There was a dramatic reduction in linear noise spiking with the 350 MHz HS antenna when compared to the 400 MHz antenna, as indicated by the red arrows (Figure 3.41). Comparison of the radargrams and the Hilbert transform radargrams indicates the presence of three distinct and relatively horizontal reflections which indicates three layers (Figures 3.39, 3.40, and 3.41).

A relatively continuous strong horizontal reflection was present at an approximate depth of 1.5 meters on Runion line 018 (Figure 3.42). There was a strong dipping reflector occurring

from 24 to 30 meters along the radargram, starting at an approximate depth of 2.1 meters and ending at a depth of 1.1 meters. There was a strong reflection beginning at 0 to 22 meters along the radargram. The reflection begins at a lateral distance of 0 to 12 meters on the radargram at an approximate depth of 3.1 meters which trends up to a depth of 2.1 meters. The observed reflection dips from 2.1 meters depth down to a depth of 3.1 meters from 12 to 22 meters along the x-axis of the radargram, where the reflection is lost. The strong reflections also occurred on the Hilbert transform radargrams (Figure 3.43). There was a reduction in linear noise spiking with the 350 MHz HS antenna when compared to the 400 MHz antenna, as indicated by the red arrows (Figure 3.44). When comparing the radargrams to the Hilbert transform radargrams there appeared to be three layers occurring based on three distinct relatively horizontal reflections (Figures 3.42, 3.43, and 3.44).

Overall, there was a marginal increase of 0.15 meters depth of penetration with the 350 MHz HS antenna when compared to the 400 MHz antenna (Figures 3.36, 3.39, and 3.42). The Hilbert transform radargrams showed the previously mentioned strong reflections as indicated in black (Figures 3.39, 3.41, 3.43). The Hilbert transform radargrams also showed a reduction in recorded noise between the 400 MHz and 350 MHz HS antennas, with linear noise spikes indicated by red arrows (Figures 3.38, 3.41, and 3.44). The graphs of standard deviation of reflection amplitude showed slightly higher values of standard deviation in the near-surface with the 350 MHz HS antenna when compared to the 400 MHz antenna (Figures 3.45, 3.46 and 3.47). There was a transitional zone of reduced signal strength as indicated by the decreasing values of standard deviations between 3 to 4 meters depth. The intersection of the lines at 4 meters depth was interpreted to be the depth of complete signal loss (noise floor). There was a slight increase in standard deviation with the 400 MHz antenna at approximately 4 meters to approximately 5.6

meters, indicating amplified noise. The color composite showed agreement on the location of strong relatively horizontal reflections as indicated by the white (Figures 3.48, 3.49 and 3.50). Other areas of agreement between the antennas are indicated by the shades of gray. There was more cyan occurring in the lower half of the radargrams, which indicated that the 400 MHz antenna is contributing more of the different signal (noise).

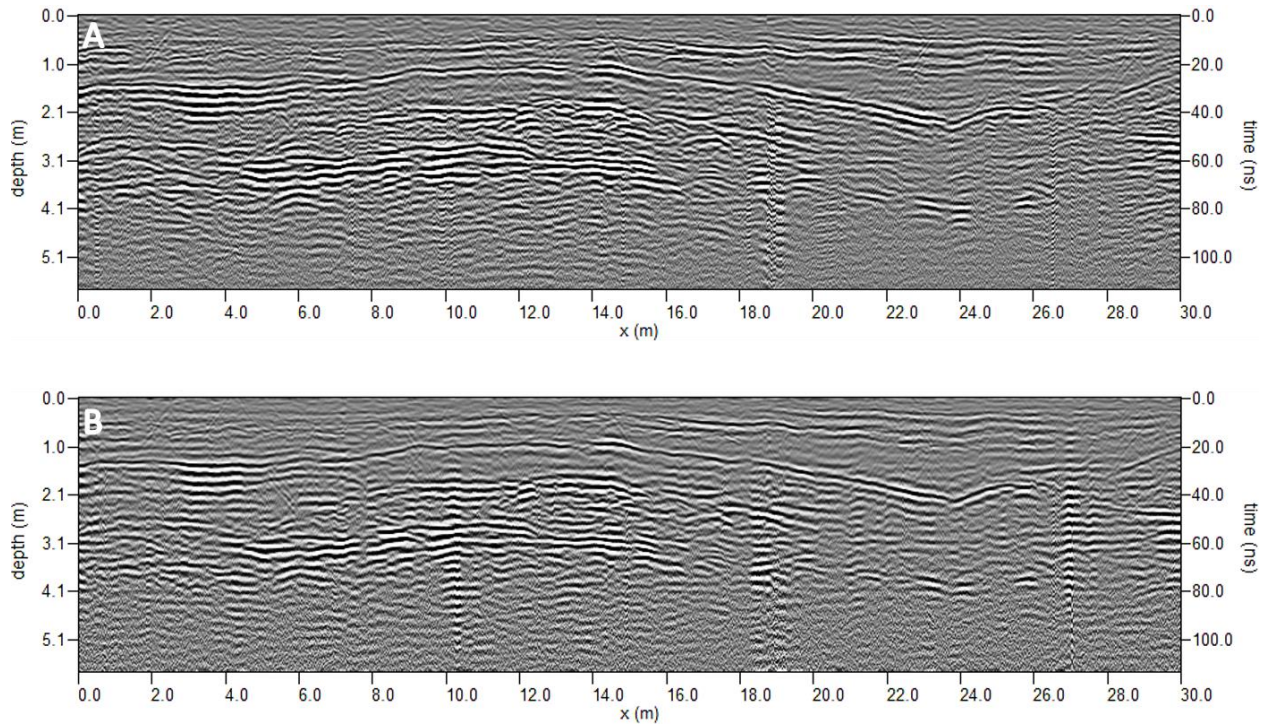


Figure 3.36. Radargram of linear feature on Runion line 002 (A) 350 MHz HS antenna (B) 400 MHz antenna

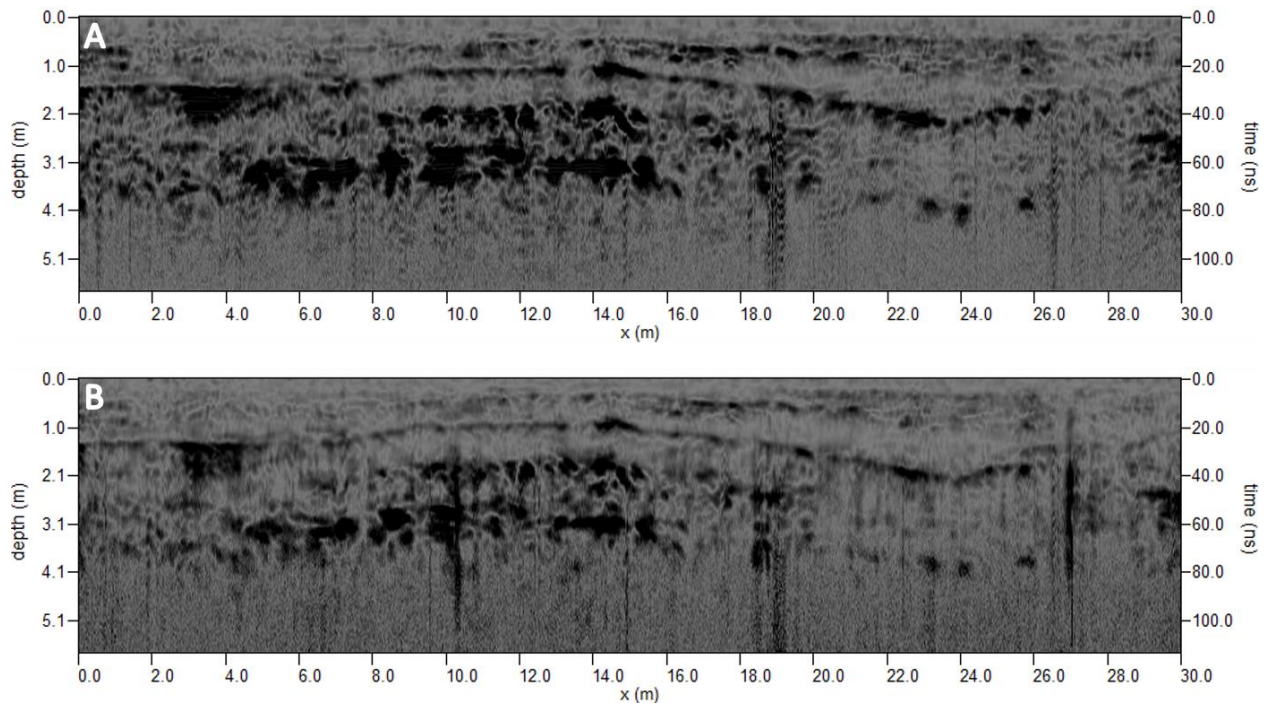


Figure 3.37. Hilbert transform radargram of linear feature on Runion line 002 (A) 350 MHz HS antenna (B) 400 MHz antenna

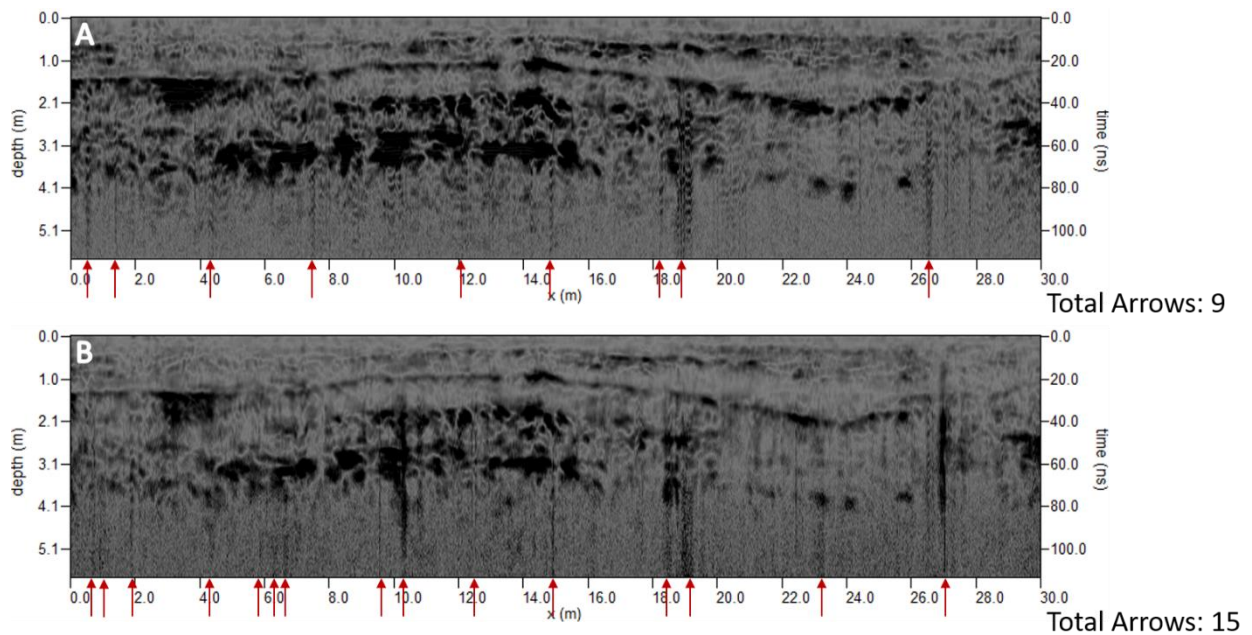


Figure 3.38. Hilbert transform radargram of linear feature on Runion line 002 (A) 350 MHz HS antenna (B) 400 MHz antenna. Red arrows indicate areas of noise.

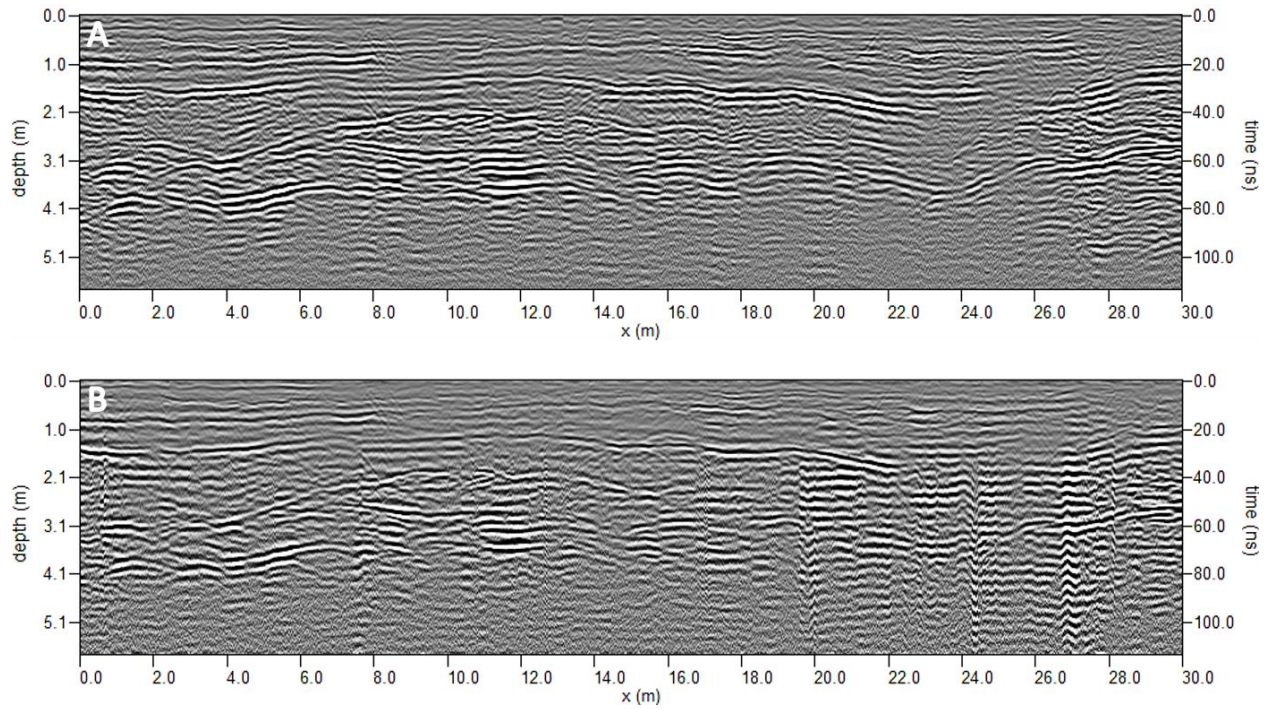


Figure 3.39. Radargram of linear feature on Runion line 014 (A) 350 MHz HS antenna (B) 400 MHz antenna

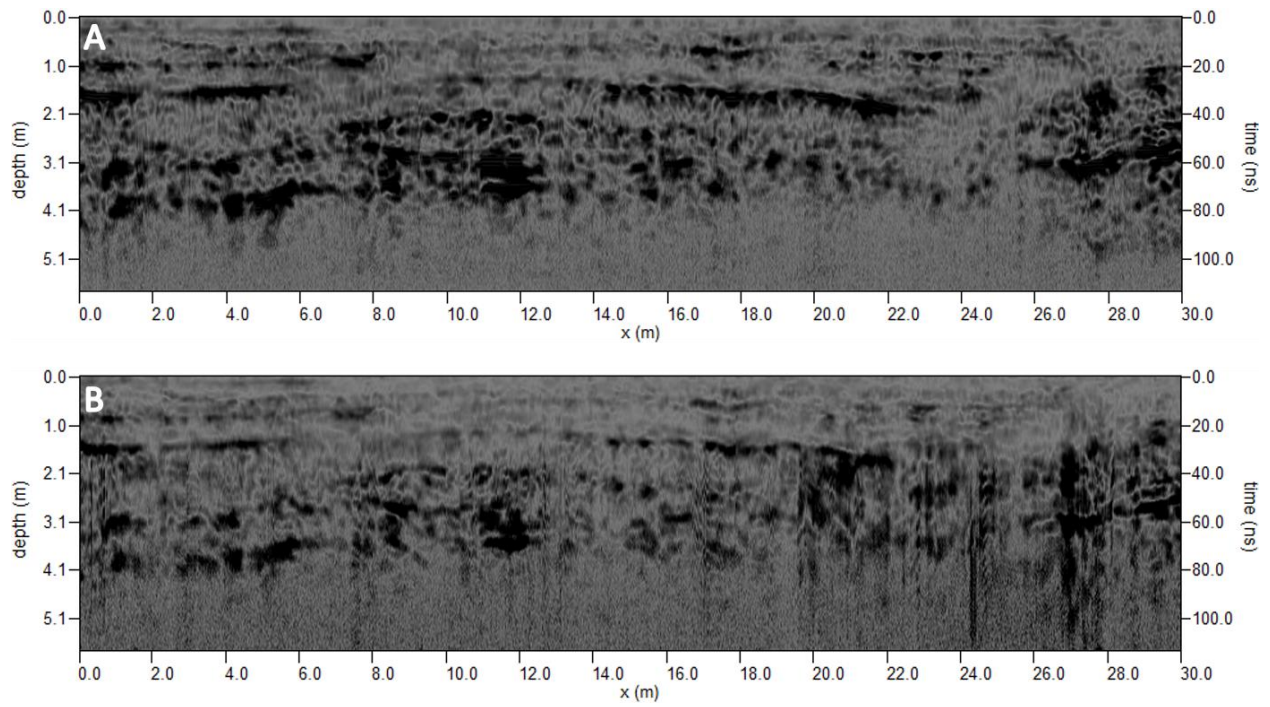


Figure 3.40. Hilbert transform radargram of linear feature on Runion line 014 (A) 350 MHz HS antenna (B) 400 MHz antenna

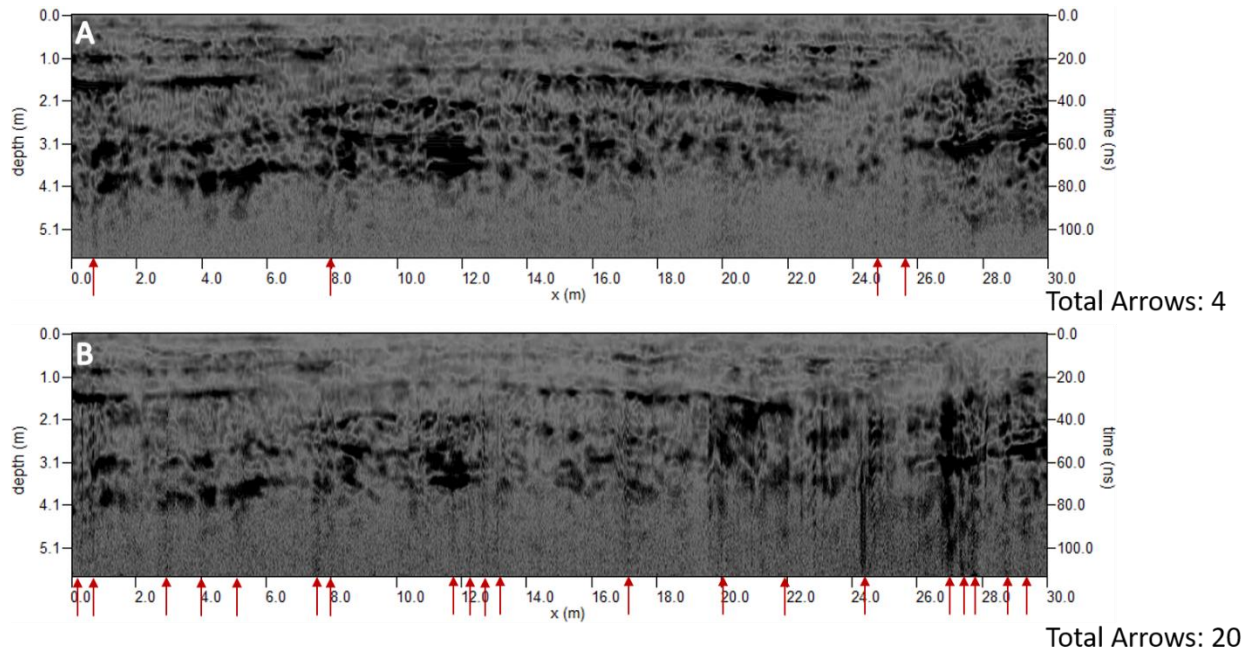


Figure 3.41. Hilbert transform radargram of linear feature on Runion line 014 (A) 350 MHz HS antenna (B) 400 MHz antenna. Red arrows indicate areas of noise.

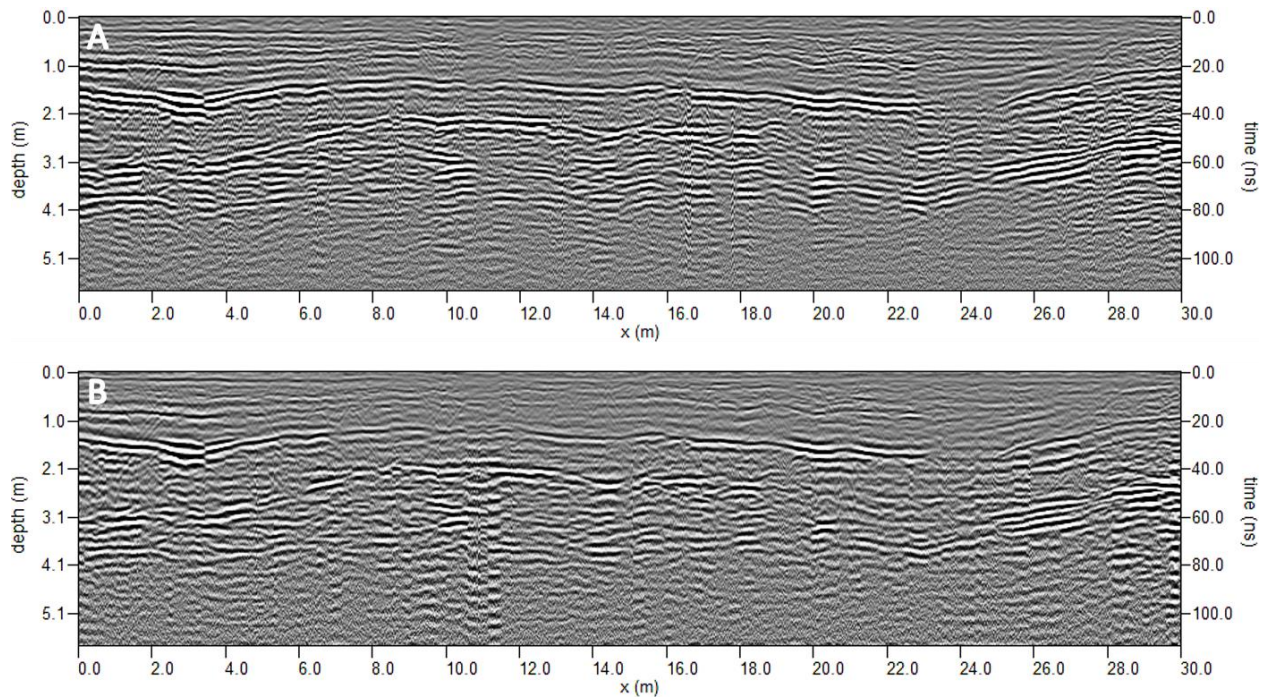


Figure 3.42. Radargram of linear feature on Runion line 018 (A) 350 MHz HS antenna (B) 400 MHz antenna

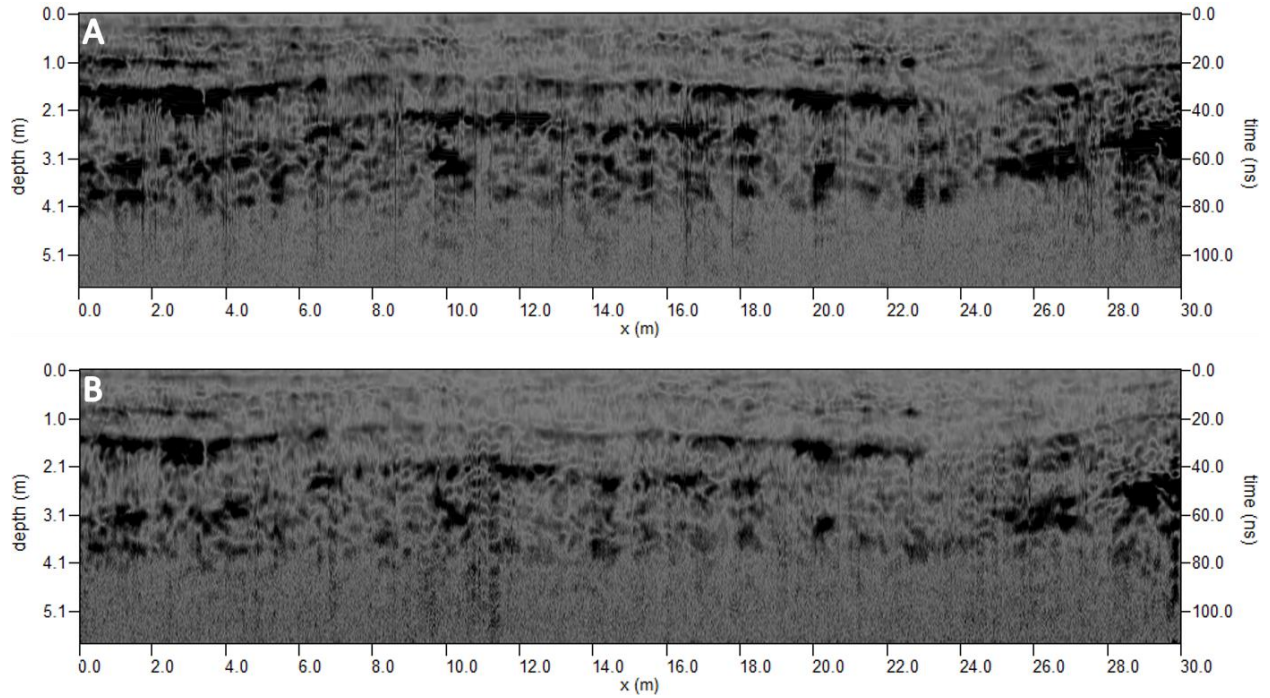


Figure 3.43. Hilbert transform radargram of linear feature on Runion line 018 (A) 350 MHz HS antenna (B) 400 MHz antenna

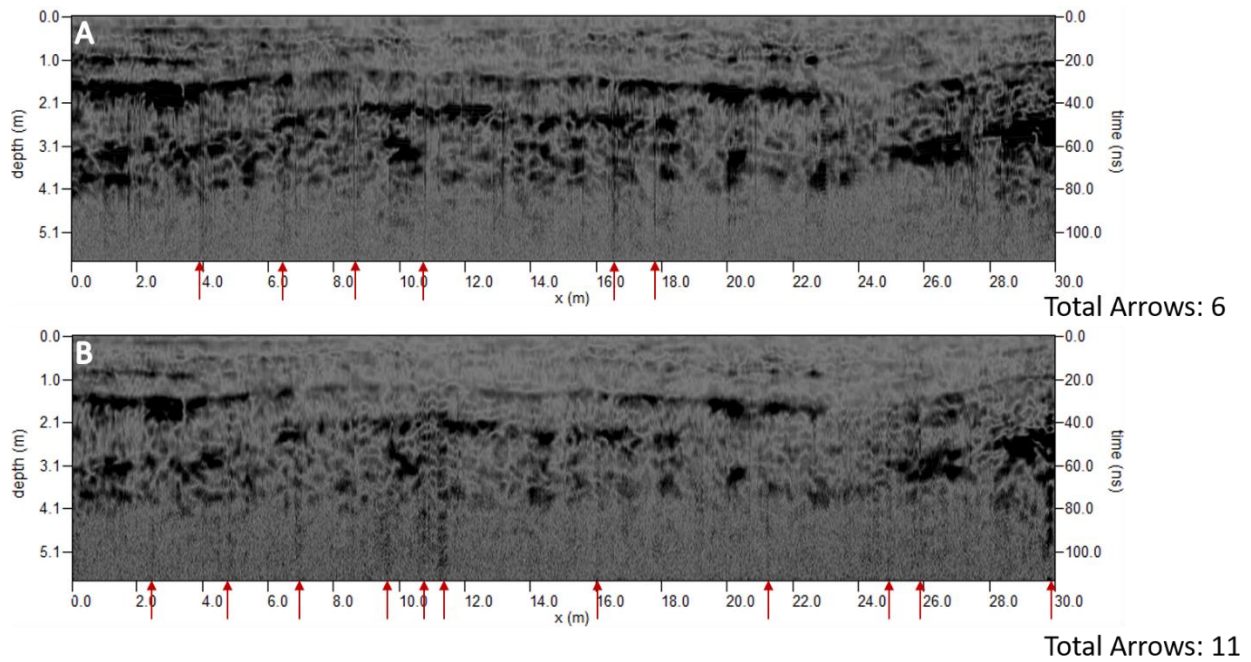


Figure 3.44. Hilbert transform radargram of linear feature on Runion line 018 (A) 350 MHz HS antenna (B) 400 MHz antenna. Red arrows indicate areas of noise.

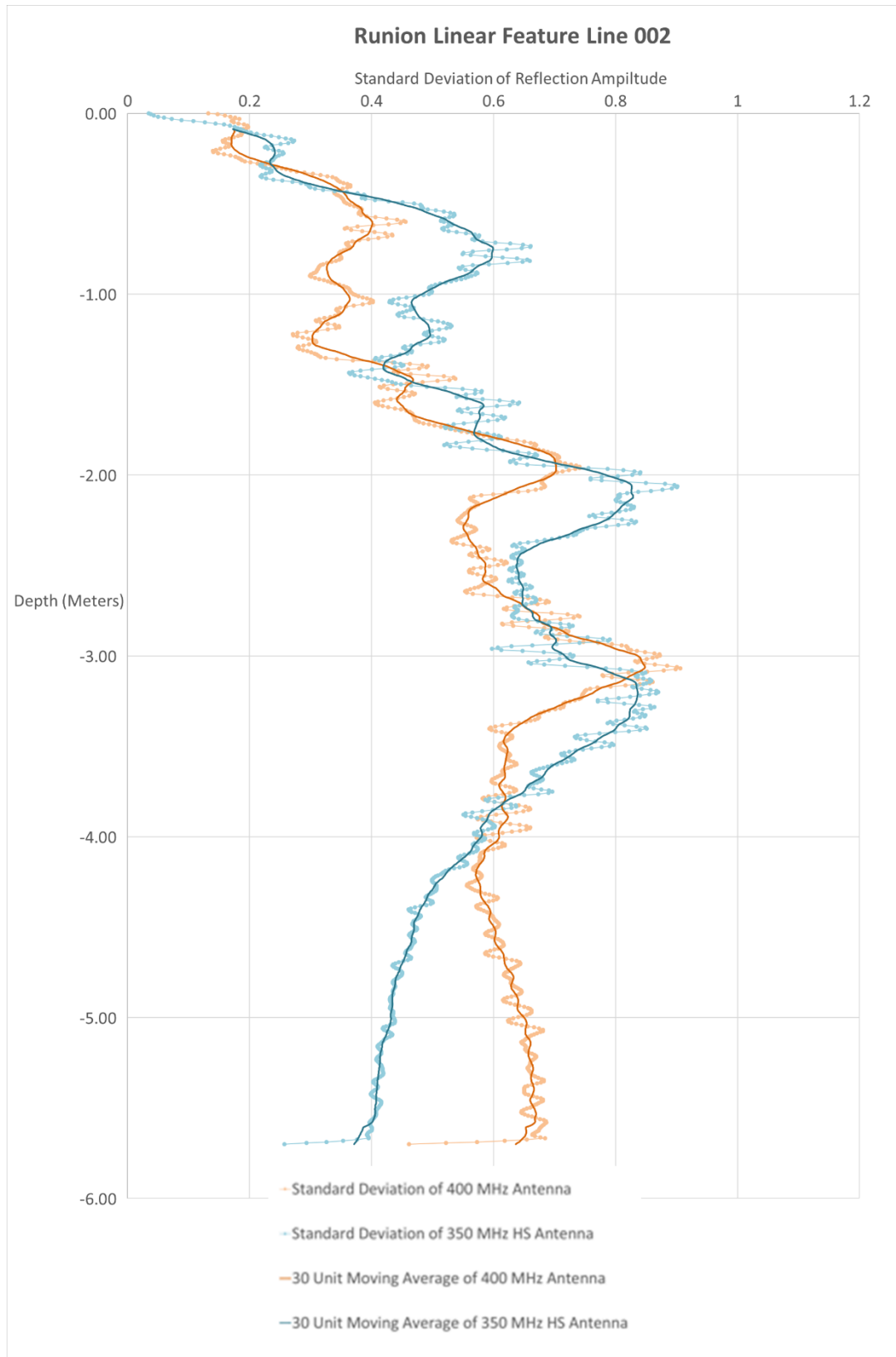


Figure 3.45. Graph of standard deviation with depth for Runion Line 002

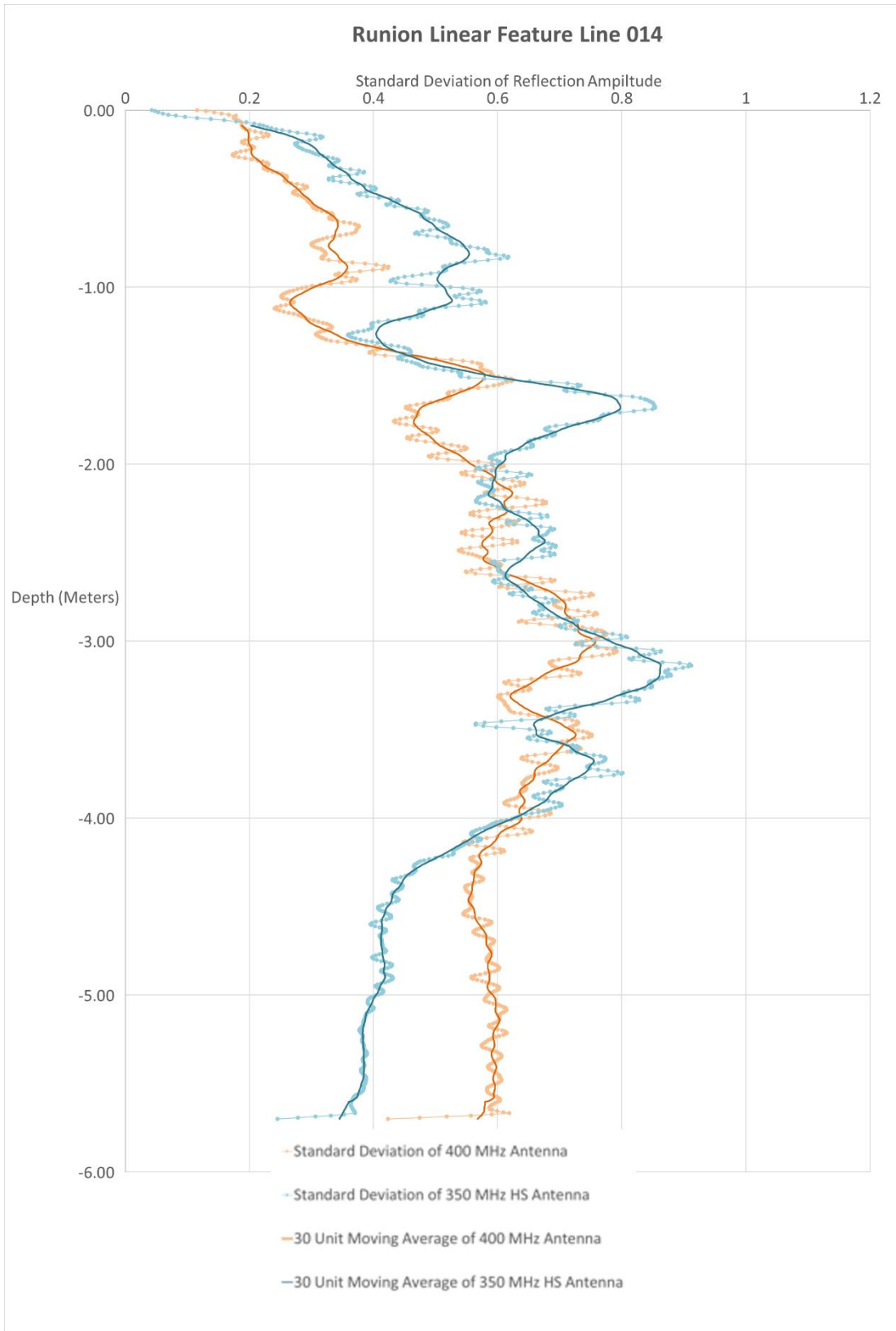


Figure 3.46. Graph of standard deviation with depth for Runion Line 014

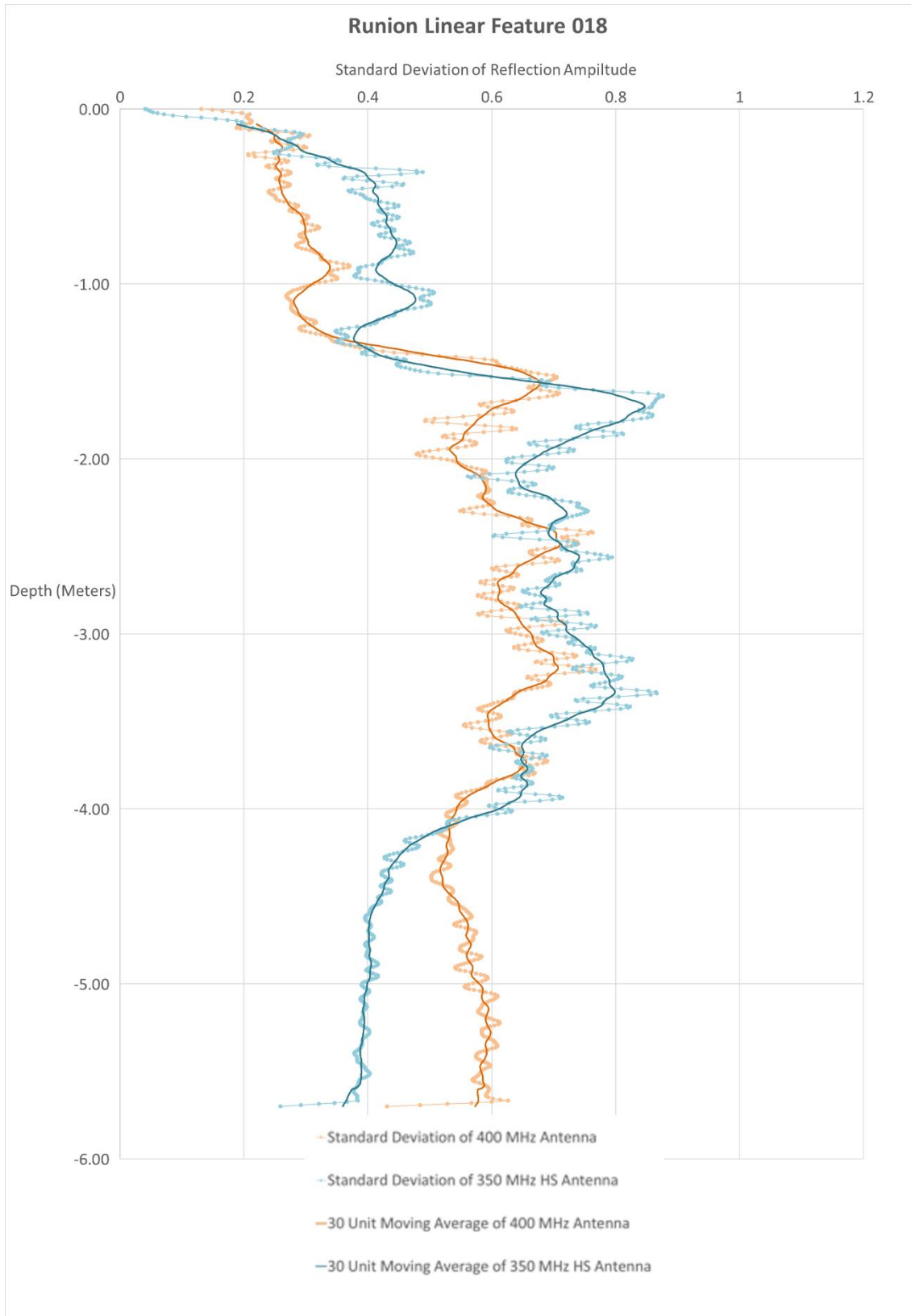


Figure 3.47. Graph of standard deviation with depth for Runion Line 018

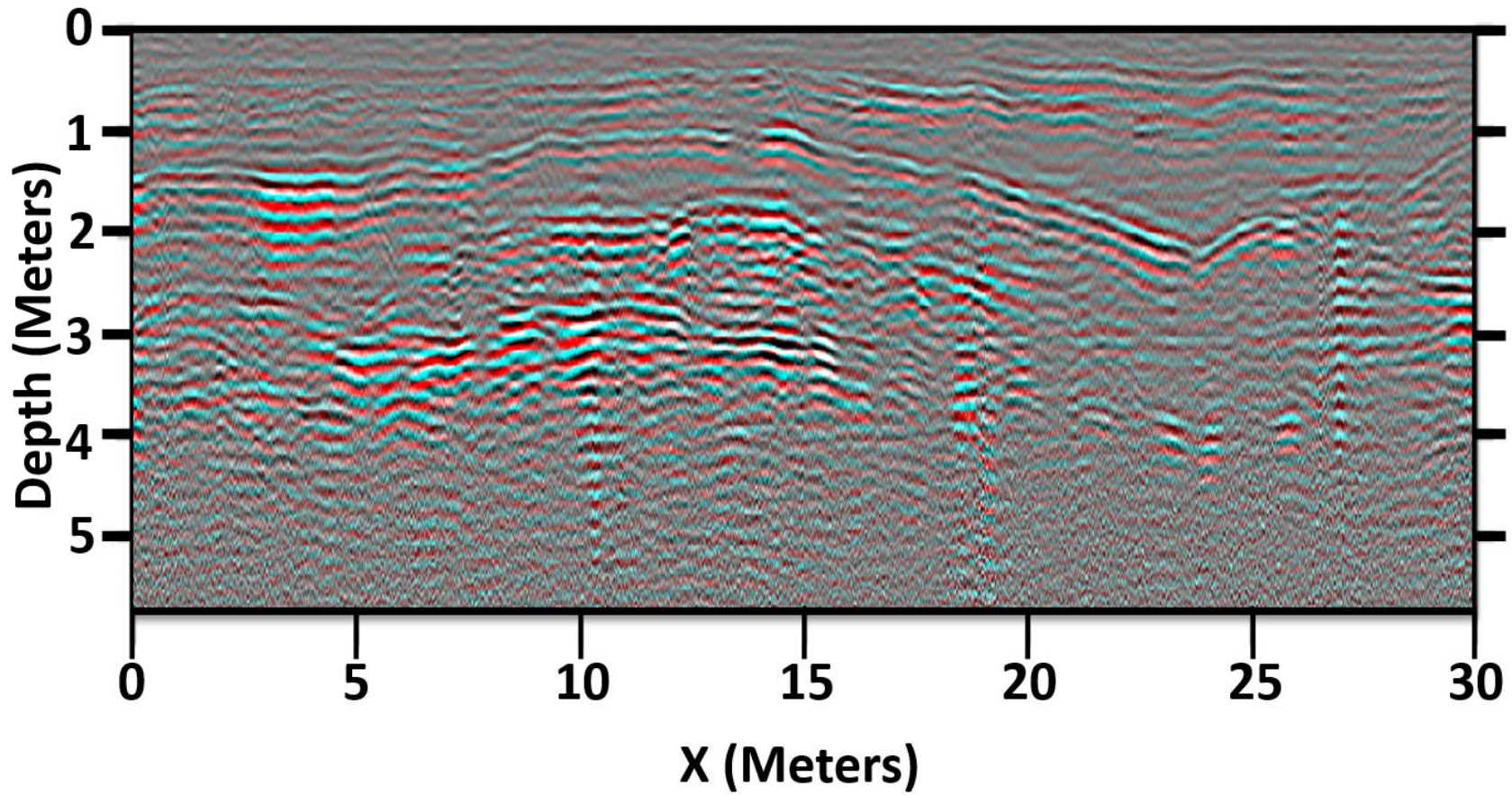


Figure 3.48. Color composite of Runion line 002, 400 MHz antenna is the blue and green band and 350 MHz HS antenna is the red band. Shades of gray indicate agreement between the 400 MHz and the 350 MHz HS antennas.

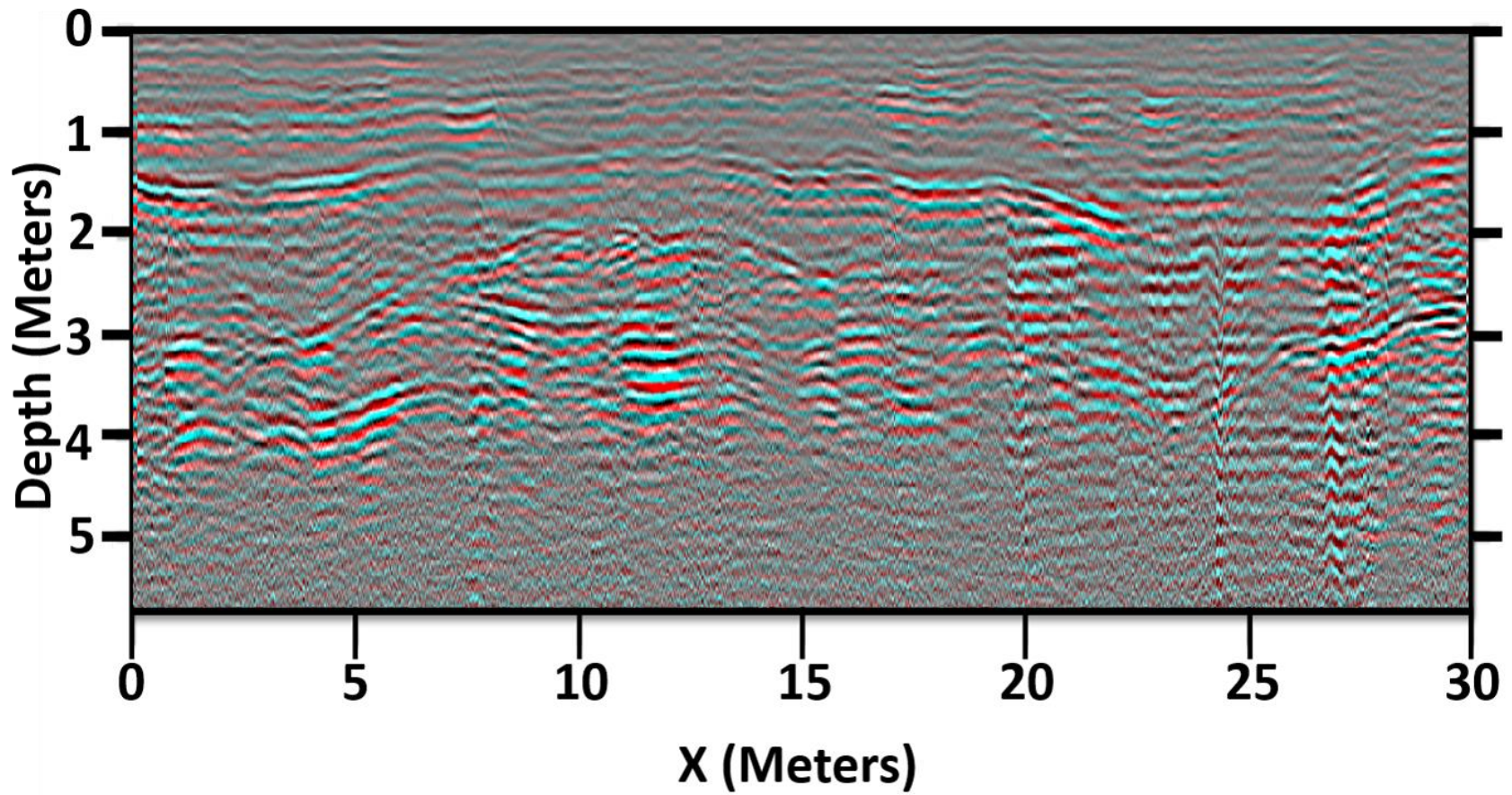


Figure 3.49. Color composite of Runion line 002, 400 MHz antenna is the blue and green band and 350 MHz HS antenna is the red band. Shades of gray indicate agreement between the 400 MHz and the 350 MHz HS antennas.

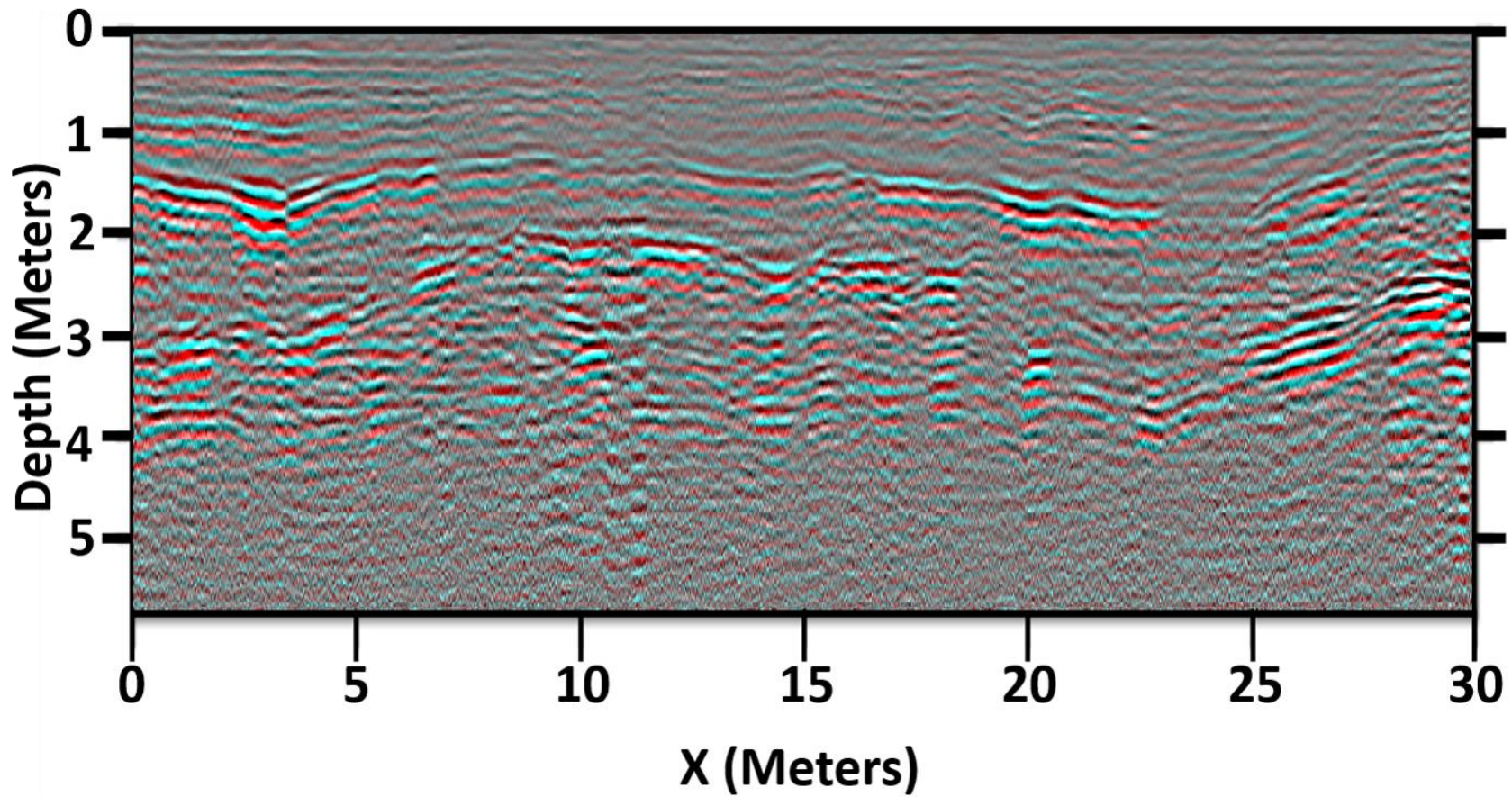


Figure 3.50. Color composite of Runion line 018, 400 MHz antenna is the blue and green band and 350 MHz HS antenna is the red band. Shades of gray indicate agreement between the 400 MHz and the 350 MHz HS antennas.

Quantitative Analysis

There were statistically significant differences occurring at different depths between the 400 MHz and 350 MHz HS antennas for all three transects. Results for Runion line 002 indicated that there were insignificant differences in the standard deviation of reflection amplitude between both the 400 MHz and 350 MHz HS antennas from 0.0 to 0.4 meters, 1.4 to 1.6 meters, and 2.6 to 3.2 meters depth (Table 3.9). There were significant differences in the standard deviations of reflection amplitude between the 400 MHz and 350 MHz HS antennas from 0.4 to 1.4 meters, 1.6 to 2.6 meters, and 3.2 to 5.6 meters depth. Statistical results for Runion line 014 indicated that there were significant differences in the standard deviation of reflection amplitude between the 400 MHz and 350 MHz HS antennas from 0.0 to 1.4 meters, 1.6 to 2.0 meters, 2.2 to 2.8 meters, and 3.0 to 5.6 meters depth. (Table 3.10). There were insignificant differences in standard deviation of reflection amplitude between the 400 MHz and 350 MHz HS antennas from a depth of 1.4 to 1.6 meters, 2.0 to 2.2 meters, and 2.8 to 3.0 meters depth. Results for Runion line 018 indicated that there were insignificant differences in the standard deviation of reflection amplitude between the 400 MHz and 350 MHz HS antennas from 0.0 to 0.2 meters, 2.4 to 2.6 meters, 3.6 to 3.8 meters, and 4.0 to 4.2 meters depth (Table 3.11). There were significant differences in the standard deviation of reflection amplitudes between the 400 MHz and 350 MHz HS antennas for depths of 0.2 to 2.4 meters, 2.6 to 3.6 meters, 3.8 to 4.0 meters, and 4.2 to 5.6 meters.

Table 3.9. P-values from the Mann-Whitney U Test at depth interval of 0.2 meters indicating significant differences between the two antenna frequencies

Runion Line 002	
Mann-Whitney U Test Results	
Depth (Meters)	P-Value
0.0 to 0.2	-
0.2 to 0.4	-
0.4 to 0.6	0.000
0.6 to 0.8	0.000
0.8 to 1.0	0.000
1.0 to 1.2	0.000
1.2 to 1.4	0.000
1.4 to 1.6	-
1.6 to 1.8	0.000
1.8 to 2.0	0.010
2.0 to 2.2	0.000
2.2 to 2.4	0.000
2.4 to 2.6	0.000
2.6 to 2.8	-
2.8 to 3.0	-
3.0 to 3.2	-
3.2 to 3.4	0.000
3.4 to 3.6	0.000
3.6 to 3.8	0.000
3.8 to 4.0	0.000
4.0 to 4.2	0.000
4.2 to 4.4	0.000
4.4 to 4.6	0.000
4.6 to 4.8	0.000
4.8 to 5.0	0.000
5.0 to 5.2	0.000
5.2 to 5.4	0.000
5.4 to 5.6	0.000
<i>Significant at 0.05 Confidence Level</i>	

Table 3.10. P-values from the Mann-Whitney U Test at depth interval of 0.2 meters indicating significant differences between the two antenna frequencies

Runion Line 014	
Mann-Whitney U Test Results	
Depth (Meters)	P-Value
0.0 to 0.2	0.031
0.2 to 0.4	0.000
0.4 to 0.6	0.000
0.6 to 0.8	0.000
0.8 to 1.0	0.000
1.0 to 1.2	0.000
1.2 to 1.4	0.000
1.4 to 1.6	-
1.6 to 1.8	0.000
1.8 to 2.0	0.000
2.0 to 2.2	-
2.2 to 2.4	0.001
2.4 to 2.6	0.000
2.6 to 2.8	0.005
2.8 to 3.0	-
3.0 to 3.2	0.000
3.2 to 3.4	0.000
3.4 to 3.6	0.000
3.6 to 3.8	0.000
3.8 to 4.0	0.000
4.0 to 4.2	0.000
4.2 to 4.4	0.000
4.4 to 4.6	0.000
4.6 to 4.8	0.000
4.8 to 5.0	0.000
5.0 to 5.2	0.000
5.2 to 5.4	0.000
5.4 to 5.6	0.000
<i>Significant at 0.05 Confidence Level</i>	

Table 3.11. P-values from the Mann-Whitney U Test at depth interval of 0.2 meters indicating significant differences between the two antenna frequencies

Runion Line 018	
Mann-Whitney U Test Results	
Depth (Meters)	P-Value
0.0 to 0.2	-
0.2 to 0.4	0.000
0.4 to 0.6	0.000
0.6 to 0.8	0.000
0.8 to 1.0	0.000
1.0 to 1.2	0.000
1.2 to 1.4	0.000
1.4 to 1.6	0.002
1.6 to 1.8	0.000
1.8 to 2.0	0.000
2.0 to 2.2	0.000
2.2 to 2.4	0.000
2.4 to 2.6	-
2.6 to 2.8	0.000
2.8 to 3.0	0.000
3.0 to 3.2	0.000
3.2 to 3.4	0.000
3.4 to 3.6	0.000
3.6 to 3.8	-
3.8 to 4.0	0.000
4.0 to 4.2	-
4.2 to 4.4	0.000
4.4 to 4.6	0.000
4.6 to 4.8	0.000
4.8 to 5.0	0.000
5.0 to 5.2	0.000
5.2 to 5.4	0.000
5.4 to 5.6	0.000
<i>Significant at 0.05 Confidence Level</i>	

CHAPTER 4. DISCUSSION

At all four test sites, both in high-loss and low-loss soils, the 350 MHz HS antenna data had a reduction in noise when compared to the 400 MHz antenna data. This is clearly the result of the high-rate stacking technology, because stacking averages multiple scans together to reduce any random signals. In low-loss soil conditions, at Carter Mansion and Runion, there is a dramatic reduction in linear noise spikes (Figures 3.27, 3.31, 3.38, 3.41, and 3.44) as indicated by the red arrows. Although noise remains present in the 350 MHz HS antenna data in high-loss conditions, there is a noticeable reduction in noise and linear noise spikes (Figures 3.5, 3.11, and 3.19).

In low-loss conditions there is a marginal increase in depth of penetration ranging from approximately 0.1 to 0.15 meters, based on the presence of reflections imaged at depth with the 350 MHz HS antenna in relation to the 400 MHz antenna. Specifically, at Carter Mansion, reflections occurring at 2.7 meters depth in the 350 MHz HS antenna data, are not seen in the 400 MHz antenna data (Figures 3.25 and 3.29). At Runion reflections appearing at approximately 4.5 meters in the 350 MHz HS antenna data are not seen in the 400 MHz antenna data. This is likely due to more noise being recorded with the 400 MHz antenna than the 350 MHz HS antenna. These results indicate that, even with “hyperstacking” technology, GPR is limited by the electrical properties of soils, such as RPD, which GPR is dependent on (Leucci 2008). High-loss soils, such as clays, tend to be electrically conductive and attenuate radar energy (Leucci 2008), which reduces the depth of penetration possible with GPR. Low-loss soils such as sands or loams tend to be electrically resistive, which allows radar reflections to be detected at greater depths (Leucci 2008).

The results of noise reduction seen in this study agree with the findings presented by Feigin and Cist (2016). However, Feigin and Cist (2016) claim an approximate 6.5 feet (2.0 meter) increase in depth of penetration with the 350 MHz HS antenna when compared to the 400 MHz antenna in low-loss soil conditions. Results from the Carter Mansion and Runion studies (low-loss conditions) indicate an approximate 0.1 to 0.15 meters increase in depth of penetration with the 350 MHz HS antenna when compared to the 400 MHz antenna. Feigin and Cist (2016) do not show a visible increase in depth of penetration in high-loss conditions, a result supported by the Taylor Cemetery and Paleochannel studies. In low-loss conditions Feigin and Cist (2016) show an increase in reflection strength at depth with the 350 MHz HS antenna. The increase in signal strength could be the result of stacking, averaging together signals that are the same to provide the appearance of increased signal strength.

The Paleochannel site, with high-loss soils, reveals significant differences in standard deviation between the 400 MHz, 350 MHz HS, and 270 MHz antennas with the Kruskal-Wallis test (Table 3.1). The pairwise comparison of the antennas indicated that the 400 MHz and 270 MHz antennas had insignificant differences in standard deviation (Table 3.2). The insignificant difference is confirmed by the overlap in standard deviations between the 400 MHz and 270 MHz antennas (Figure 4.1). This is further supported by similarities between the 400 MHz and 270 MHz antenna signal standard deviations with depth (Figure 3.6). Both the 400 MHz and 270 MHz antenna data are statistically and visually different when data curves are compared from the 350 MHz HS antenna (Table 3.2, Figures 3.6 and 4.1). At the depth where all three standard deviation lines intersect for the Paleochannel data (Figure 3.6) the 400 MHz and 270 MHz antenna data are significantly different from the 350 MHz antenna data. This is possibly due to the intersection of standard deviation lines occurring at a point within a 0.2 meter depth

increment, and before and after the intersection the lines of standard deviation were more separated (higher differences in standard deviation). These statistics support the visual differences that are seen in the radargram data at the Paleochannel site.

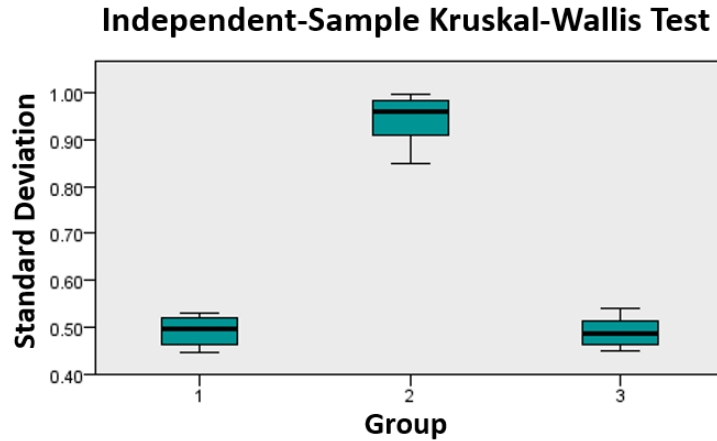


Figure 4.1. Independent-sample Kruskal-Wallis test of the Paleochannel site standard deviations between antenna groups. Group 1 is the 400 MHz antenna, group 2 is the 350 MHz HS antenna, and group 3 is the 270 MHz antenna.

Quantitative analysis of Taylor Cemetery data, a site with high-loss soils, show that there are statistically significant differences in standard deviations between the 400 MHz and 350 MHz HS antenna data with the Mann-Whitney U test (Tables 3.3, 3.4, 3.5, and 3.6). Taylor Cemetery unmarked burial line 003 has a statistically significant standard deviation difference occurring from a depth of 0.0 to 1.4 meters (Table 3.5), which is represented by the separation of the standard deviation lines (Figure 3.20). On the graph, at approximately 1.4 to 1.6 meters, the lines overlap and there is a statistically insignificant difference between the 400 MHz and 350 MHz antennas. Then the standard deviation lines begin to separate again, at an approximate depth of 1.6 meters, indicating that the differences between the 400 MHz and 350 MHz HS antennas are statistically significant. The Taylor Cemetery unmarked burial line 004 has

statistically significant standard deviation differences from a depth of 0.0 to 3.0 meters (Table 3.6), which is represented by the lack of overlap of lines on the standard deviation graph (Figure 3.21) within the 0.2 meter depth increment. Taylor Cemetery marked burial line 003 has a statistically significant standard deviation difference occurring at a depth of 0.0 to 1.4 meters (Table 3.3), which is represented by the separation of the lines on the standard deviation graph (Figure 3.12). At approximately 1.4 to 1.6 meters there was less separation between the lines and a statistically insignificant difference between the 400 MHz and 350 MHz antennas. Then the lines begin to separate again at an approximate depth of 1.6 meters indicating that the differences between the 400 MHz and 350 MHz HS are statistically significant. Taylor Cemetery marked burial line 006 has statistically significant standard deviation differences from a depth of 0.0 to 3.0 meters (Table 3.4), which is represented by the lack of overlap of lines on the standard deviation graph (Figure 3.13) within 0.2 meter depth increments. The statistical results support the visual differences observed in radargram data collected at Taylor Cemetery.

Quantitative analysis of Carter Mansion, a site with low-loss soils, show that there are statistically significant differences in standard deviations between the 400 MHz and 350 MHz HS antennas with the Mann-Whitney U test (Tables 3.7 and 3.8). Carter Mansion line 015 has a statistically significant difference between the 400 MHz and 350 MHz HS antennas at all depths from 0.0 to 4.0 meters (Table 3.7), which is represented visually, by the lack of overlap of the lines occurring on the standard deviation graph (Figure 3.32). Moreover, Carter Mansion line 024 has a statistically significant difference between the 400 MHz and 350 MHz HS antennas at all depths from 0.0 to 4.0 meters (Table 3.8), which is represented visually, by the lack of overlap of the standard deviation lines (Figure 3.33). These findings may be attributed to the low-loss soil conditions or potentially not surveying over the exact same point due to human

error. However, these statistics support the visual differences observed in radargram data at Carter Mansion.

Quantitative analysis of Runion, a site with low-loss soils, shows that there are statistically significant differences in standard deviation between the 400 MHz and 350 MHz HS antennas with the Mann-Whitney U test (Tables 3.9, 3.10 and 3.11). Runion line 002 has statistically insignificant differences in standard deviation between the 400 MHz and 350 MHz HS antennas from a depth of 0.0 to 0.4 meters (Table 3.9), which is represented visually, by the overlap of standard deviation lines (Figure 3.45). There is a statistically significant difference in standard deviation between the 400 MHz and 350 MHz HS antenna data from a depth of 0.4 to 1.4 meters visually, represented by the lack of overlap of standard deviation lines plotted on the graph. There is an insignificant difference in the standard deviation line data for the 400 MHz and 350 MHz HS antennas from a depth of 1.4 to 1.6 meters represented visually, by the overlap of lines on the graph. There is a statistically significant difference in standard deviation between the 400 MHz and 350 MHz HS antenna data from a depth of 1.6 to 2.6 meters as visually, represented by the lack of overlap of line occurring on the graph. There is an insignificant difference in standard deviation between the 400 MHz and 350 MHz HS antenna data from a depth of 2.6 to 3.2 meters represented, by the overlap of lines on the graph. There is a statistically significant difference in standard deviation between the 400 MHz and 350 MHz HS antenna data from a depth of 3.2 to 5.6 meters visually, represented by the lack of overlap of standard deviation lines occurring on the graph. These trends are seen in both the statistics and graphs of Runion lines 014 and 018 (Tables 3.10, 3.11, Figures 3.46, and 3.47). All these statistics support the visual differences observed on radargram data at Runion.

In general, the quantitative analysis at all four sites confirms conclusions drawn from the visual analysis of the graphs. In the near-surface (upper 1 to 2 meters) the statistics prove that there are significant differences between the 400 MHz and 350 MHz HS antennas. This difference is likely related to antenna power. The 350 MHz HS (digital) antenna has a higher power relative to the 400 MHz (analog) antenna based on the higher standard deviations which occur in the near-surface on the graph. There was a transitional zone approximately 0.5 meters above and below the interpreted noise floor, which corresponds to the area on the graph where the antenna standard deviation lines cross. Below the transitional zone, the noise floor, the standard deviation lines separate and the noise in the 400 MHz antenna is amplified compared to the 350 MHz HS antenna. This is represented by the higher standard deviation values.

Feigin and Cist (2016) compare radargrams from high-loss and low-loss conditions, although, they do not actually define high-loss and low-loss. Most GPR specialists consider clay-rich soils to be high-loss conditions and low-loss soils are typically sandy or loamy soils (Jol, 1995; Smith and Jol, 1995; Jol, 2009; Everett 2013; Goodman and Piro 2013; Reynolds 2013). It appears that even in prime GPR soil conditions, such as those at Carter Mansion and Runion, there is only a marginal increase in depth of penetration with the 350 MHz HS antenna. At all four study sites the antennas were nearly tested to the maximum depth of penetration (noise floor was imaged). Specifically, at Runion and Carter Mansion the GPR imaged features to approximately 4 meters below surface with the 400 MHz antenna, which is the stated depth limit by GSSI (Table 1.1). This proves that the low-loss sites are in fact very low loss. In fact, the noise floor for the 400 MHz in low loss soils is identical to the one presented by Feigin and Cist (2016) (10 feet). Without a clear definition of Feigin and Cist's (2016) "low-loss conditions" it is possible that the results they provided had different gains applied. Preliminary results, during

data processing, indicate differences in gain between the 350 MHz HS and 400 MHz antennas even when the same gain curve is applied (Figure 2.4), presumably due to antenna power differences. Theoretically it may be possible to increase the scans per meter and reduce the scans per second, while walking extremely slowly with the 400 MHz antenna in order to attempt to replicate the stacking results of the 350 MHz HS. However, this would greatly increase the time required for data collection.

This study utilized different analysis techniques such as a statistical Mann-Whitney U test and raster image composite analysis to compare and analyze radargrams. These analyses provide context for innovative ways to analyze and interpret geophysical radar data. Analyzing radargrams with different techniques may provide insights about the data that were not observable with simple visual analysis. The potential of “hyperstacking” technology to reduce noise without post-acquisition processing is confirmed (Figure 2.5) and shows that there is room for continued improvement in radar technology to reduce the amount of post-acquisition processing required to be able to interpret radar data.

Continued improvements in digital technology will enhance radar data acquisition and data quality. In theory, digital technology will permit increased depth penetration and reduction of SNR. Introducing the geophysical community to quantitative ways of visualizing radar data, such as graphing standard deviation of reflection amplitude or analyzing results from a Mann-Whitney U test, have proven useful in evaluating antenna performance.

This study examined four sites, two high-loss conditions and two low-loss conditions, and therefore cannot be considered to be exhaustive. More sites, with even lower-loss conditions, such as a freshwater sand beach or a glacier would need to be examined to continue to compare the antennas. Those sites are known to have electrical properties which allow for increased depth

of penetration (Everett 2013; Goodman and Piro 2013; Reynolds 2013). Examining sites with known features at greater depth would be of use to determine if those features would be detectable with the 350 MHz HS antenna but not the 400 MHz antenna.

CHAPTER 5. CONCLUSION

GPR performs differently depending on soil conditions and antenna frequency. The objective of this thesis was to compare depth of penetration and noise reduction of the 350 MHz HS and 400 MHz GPR antennas. Two study sites, the Paleochannel and Taylor Cemetery, are characterized by high-loss soils, based on the limited depth of penetration before reaching the noise floor. Two study sites, Carter Mansion and Runion, are characterized by low-loss soils, based on a depth of penetration between 2 to 3 meters before reaching the noise floor. Statistical results indicate that there are significant differences in standard deviation of radar reflection amplitude occurring at depth, over 0.2 meter increments, between the 400 MHz and 350 MHz HS antennas. Results are in agreement with Feigin and Cist (2016), that in both high-loss and low-loss soil conditions, the 350 MHz HS antenna reduces random noise. There is a marginal increase of 0.1 to 0.15 meters in depth of penetration with the 350 MHz HS antenna in low-loss soil conditions. However, there is no increase in depth of penetration in high-loss soils when the 350 MHz HS antenna is compared to the 400 MHz antenna. The results of this study do not support Feigin and Cist (2016) on their claim of significant increased depth of penetration in low-loss conditions. Analysis of more data from more sites may provide additional insights.

REFERENCES

- Agisoft. 2006. Tutorial (Beginner Level): Orthomosaic and DEM Generation with Agisoft PhotoScan Pro 1.3 (without Ground Control Points). St. Petersburg: Agisoft LLC. [accessed 2020 Jan 25]. <https://www.agisoft.com/support/tutorials/beginner-level/>
- Alsharahi G, Driouach A, Faize A. 2015. Performance of GPR Influenced by Electrical Conductivity and Dielectric Constant. In: 9th International Conference Interdisciplinary in Engineering. Trigu-Mures: Procedia Technology. p. 570-575. [accessed 2020 Jan 26]
- Andersen T, Poulsen S, Thomsen P, Havas K. 2018. Geological characterization in urban areas based on geophysical mapping: A case study from Horsens, Denmark. *Journal of Applied Geophysics* 150:338-349. [accessed 2020 Jan 17]. <https://doi.org/10.1016/j.jappgeo.2017.08.009>
- Bigman D. 2013. Mapping social relationships: geophysical survey of a nineteenth-century American slave cemetery. *Archaeological and Anthropological Sciences* 6:17-30. [accessed 2020 Jan 17]. <https://doi.org/10.1007/s12520-013-0119-6>
- Bigman DP, King A, Walker CP. 2011. Recent Geophysical Investigations and New Interpretations of Etowah's Palisade. *Southeastern Archaeology* 30(1):38-50.
- Clark Labs. Released 2017. TerrSet for Windows, Version 18.31. Worcester, MA: Clark Labs.
- Cobb C, King A. 2005. Re-Inventing Mississippian Tradition at Etowah, Georgia. *Journal of Archaeological Method and Theory* 12:167-193.
- Davis H. 1994. Soil Survey of Sullivan County, Tennessee. Washington D.C.: United States Department of Agriculture. [accessed 2020 Jan 29].

https://www.nrcs.usda.gov/Internet/FSE_MANUSCRIPTS/tennessee/TN163/0/sullivan.pdf

Davis J, Annan A. 1989. Ground-Penetrating Radar for High Resolution Mapping of Soil and Rock Stratigraphy. *Geophysical Prospecting* 37:531-551.

Diamanti N, Annan A. 2019. Understanding the use of ground-penetrating radar for assessing clandestine tunnel detection. *The Leading Edge* 38:453-459. [accessed 2020 Jan 17].
<https://doi.org/10.1190/tle38060453.1>

Doolittle J, Bellantoni N. 2010. The search for graves with ground-penetrating radar in Connecticut. *Journal of Archaeological Science* 37:941-949. [accessed 2020 Jan 31].

Doolittle J, Jenkinson B, Hopkins D, Ulmer M, Tuttle W. 2006. Hydropedological investigations with ground-penetrating radar (GPR): Estimating water-table depths and local groundwater flow pattern in areas of coarse-textured soils. *Geoderma* 131:317-329. [accessed 2020 Jan 17]. <https://doi.org/10.1016/j.geoderma.2005.03.027>

EEGS. 2019. What is Geophysics?. [Eegs.org](https://www.eegs.org/what-is-geophysics-). <https://www.eegs.org/what-is-geophysics->

Elder J. 1958. Soil Survey Washington County, Tennessee. Washington D.C.: United States Department of Agriculture. [accessed 2020 Jan 29].
https://www.nrcs.usda.gov/Internet/FSE_MANUSCRIPTS/tennessee/washingtonTN1958/Washington.pdf

Ernenwein E, Franklin J. 2017. Archaeological Geophysics at Runion, a Protohistoric Site on the Middle Nolichucky River. Tennessee Council for Professional Archaeology. [accessed 2020 Jan 31].

<https://tennesseearchaeologycouncil.wordpress.com/2017/09/12/archaeological-geophysics-at-runion-a-protohistoric-site-on-the-middle-nolichucky-river/>

Ernenwein, E.G, Cannon C.M. 2017. Geophysical Survey and Excavations at Carter Mansion (40CR5). Final Report submitted to Tennessee Historical Commission, Nashville. 21 pp.

ESRI. Released 2019. ArcGIS Pro for Windows, Version 2.4.0. Redlands, CA: ESRI.

Everett M. 2013. Near-surface applied geophysics. 1st ed. Cambridge: Cambridge University Press.

Feigin J, Cist D. 2016. Evaluating the Effectiveness of Hyperstacking for GPR Surveys. In: SAGEEP 2016 - 29th Annual Symposium on the Application of Geophysics to Engineering and Environmental Problems. Environmental and Engineering Geophysical Society. [accessed 2020 Jan 31]

Feigin J. 2017. HyperStacking GPR. xyHt. [accessed 2020 Feb 16].

<https://www.xyht.com/energyutilities/hyperstacking-gpr/>

Geophysical Survey Systems Inc. 2014. <https://patents.google.com/patent/EP2698647A1/en>. [accessed 2020 Feb 14]

Golden Software. Released 2015. Surfer for Windows, Version 13.0. Golden, CO: Golden Software LLC.

Goodman D, Piro S. 2013. GPR Remote Sensing in Archaeology. Berlin: Springer Berlin.

Goodman D. Released 2019. GPR-Slice for Windows, Version 7.0. Woodland Hills, CA: GPR-Slice © Ground Penetrating Radar Imaging Software.

- Hansen J, Pringle J, Goodwin J. 2014. GPR and Bulk Ground Resistivity Surveys in Graveyards: Locating Unmarked Burials in Contrasting Soil types. *Forensic Science International* 237:e14-e29.
- Hartgrove N. 2000. Soil Survey of Carter County, Tennessee. Washington D.C.: United States Department of Agriculture. [accessed 2020 Jan 29].
https://www.nrcs.usda.gov/Internet/FSE_MANUSCRIPTS/tennessee/TN019/0/tn_carter.pdf
- Hausmann J, Steinel H, Kreck M, Werban U, Vienken T, Dietrich P. 2013. Two-dimensional geomorphological characterization of a filled abandoned meander using geophysical methods and soil sampling. *Geomorphology* 201:335-343. [accessed 2020 Jan 17].
<https://doi.org/10.1016/j.geomorph.2013.07.009>
- IBM Corp. Released 2017. IBM SPSS Statistics for Windows, Version 25.0. Armonk, NY: IBM Corp.
- Jol H. 1995. Ground penetrating radar antennae frequencies and transmitter powers compared for penetration depth, resolution and reflection continuity1. *Geophysical Prospecting* 43:693-709.
- Jol H. 2009. *Ground Penetrating Radar Theory and Applications*. 1st ed. Oxford: Elsevier Science.
- Kim J, Cho S, Yi M. 2007. Removal of ringing noise in GPR data by signal processing. *Geosciences Journal* 11:75-81. [accessed 2020 Feb 27]

- Klotzsche A, Jonard F, Looms M, van der Kruk J, Huisman J. 2018. Measuring Soil Water Content with Ground Penetrating Radar: A Decade of Progress. *Vadose Zone Journal* 17:1-9. [accessed 2020 Jan 17]. <https://doi.org/10.2136/vzj2018.03.0052>
- Leucci G. 2008. Ground Penetrating Radar: The Electromagnetic Signal Attenuation and Maximum Penetration Depth. *Scholarly Research Exchange* 2008:1-7. [accessed 2020 Feb 28]
- Mostapha A, Faize A, Alsharahi G, Louzazni M, Driouach A. 2019. Effect of External Noise on Ground Penetrating Radar Ability to Detect Objects. *International Journal of Microwave and Optical Technology*, 14:124-131. [accessed 2020 Feb 27]
- Nimnate P, Thitimakorn T, Choowong M, Hisada K. 2017. Imaging and locating paleo-channels using geophysical data from meandering system of the Mun River, Khorat Plateau, Northeastern Thailand. *Open Geosciences* 9.
- Oskooi B, Parnow S, Smirnov M, Varfinezhad R, Yari M. 2018. Attenuation of random noise in GPR data by image processing. *Arabian Journal of Geosciences* 11. [accessed 2020 Feb 27]
- Reynolds J. 2013. *An introduction to applied and environmental geophysics*. 2nd ed. Hoboken, N.J.: Wiley
- Roth K, Schulm R, Flühler H, Attinger W. 1992. Calibration of Time Domain Reflectometry for Water Content Measurement Using a Composite Dielectric Approach. *Water Resources Research* 26:2267-2273.

- Salinas Naval V, Santos-Assunção S, Pérez-Gracia V. 2018. GPR Clutter Amplitude Processing to Detect Shallow Geological Targets. *Remote Sensing* 10:1-16. [accessed 2020 Jan 17]. <https://doi.org/10.3390/rs10010088>
- Schultz J, Collins M, Falsetti A. 2006. Sequential Monitoring of Burials Containing Large Pig Cadavers Using Ground-Penetrating Radar. *Journal of Forensic Sciences* 51:607-616. [accessed 2020 Jan 31]. <https://onlinelibrary.wiley.com/doi/epdf/10.1111/j.1556-4029.2006.00129.x>
- Słowik M. 2011. Reconstructing migration phases of meandering channels by means of ground-penetrating radar (GPR): the case of the Odra River, Poland. *Journal of Soils and Sediments* 11:1262-1278. [accessed 2020 Jan 17]. <https://doi.org/10.1007/s11368-011-0420-x>
- Smith D, Jol H. 1995. Ground Penetrating Radar: Antenna Frequencies and Maximum Probable Depths of Penetration in Quaternary Sediments. *Journal of Applied Geophysics* 33:93-100.
- Spathis A. 1983. Design Data for Digital Butterworth Filters in Geophysical Data Processing. *Exploration Geophysics* 14:63-71. [accessed 2020 Jan 14]. <https://doi.org/10.1071/EG983063>
- Stec B, Susek W. 2018. Theory and Measurement of Signal-to-Noise Ratio in Continuous-Wave Noise Radar. *Sensors* 18:1-11.
- Tennessee Valley Authority. 1949. *Geology and foundation treatment*. Knoxville, Tenn.: Tennessee Valley Authority.

- van Dam R. 2001. Causes of Ground-Penetrating Radar Reflections in Sediments [Ph.D]. Vrije Universiteit Amsterdam.
- Verdonck L, Taelman D, Vermeulen F, Docter R. 2015. The Impact of Spatial Sampling and Migration on the Interpretation of Complex Archaeological Ground-penetrating Radar Data. *Archaeological Prospection* 22:91-103. [accessed 2020 Jan 17].
<https://doi.org/10.1002/arp.1501>
- Wang W, Hao L, Li X, Sun J. 2017. Signal Processing Technology and its Application Research of Ground Penetrating Radar (GPR). *IOP Conference Series: Earth and Environmental Science* 69:012077. [accessed 2020 Feb 16].
<https://iopscience.iop.org/article/10.1088/1755-1315/69/1/012077/pdf>
- Weaver W. 2006. Ground-penetrating radar mapping in clay: success from South Carolina, USA. *Archaeological Prospection* 13:147-150. [accessed 2020 Jan 31]
- Welc F, Mieszkowski R, Trzciński J, Kowalczyk S. 2015. Western Section of the ‘Dry Moat’ Channel Surrounding Step Pyramid Complex in Saqqara in the Light of Ground-penetrating Radar Prospection. *Archaeological Prospection* 22:293-305. [accessed 2020 Jan 17]. <https://doi.org/10.1002/arp.1514>
- Westoby M, Brasington J, Glasser N, Hambrey M, Reynolds J. 2012. ‘Structure-from-Motion’ Photogrammetry: A low-cost, Effective Tool for Geoscience Applications. *Geomorphology* 179:300-314.
- Wyatt D, Temples T. 1996. Ground-Penetrating Radar Detection of Small-Scale Channels, Joints and Faults in the Unconsolidated Sediments of the Atlantic Coastal Plain. *Environmental Geology* 27:219-225. [accessed 2020 Jan 31]. <https://doi.org/10.1007/BF00770435>

APPENDIX: Coordinates of Site Locations

Location Name	Longitude	Latitude
Paleochannel	-82.551651	36.539888
Carter Mansion	-82.204647	36.354056
Taylor Cemetery	-82.273505	36.316881
Runion	-82.608429	36.18938

VITA

MONTANA L. KRUSKE

- Education: M.S. Geosciences, East Tennessee State University, Johnson City,
Tennessee, 2020
B.S. Geology, Lake Superior State University, Sault Ste. Marie,
Michigan, 2018
A.S. Science, Delta College, University Center,
Michigan, 2015
- Professional Experience: Graduate Assistant, East Tennessee State University, Department
of Geosciences, College of Arts and Sciences, 2018-2020
- Publications: C.R. Mattheus, T.P. Diggins, C. Boyce, J. Cockrell, **M. Kruske**,
and M. VanWinkle (2018). "Geomorphology of a Harbor-
Breakwater Beach along a High Sand Supply, Wave
Dominated Great Lakes Littoral Cell."
Journal of Coastal Research: Volume 35, Issue 1:
pp. 41 – 55.
- Honors and Awards: East Tennessee State University Graduate Research Grant
Research Grant (\$800), East Tennessee State University,
Spring 2019